EXHUMATION OF THE CASCADE RANGE, OREGON: INVESTIGATING CLIMATE PATTERN COINCIDENCE WITH EXHUMATION TIMING DURING OROGEN EVOLUTION

A Thesis

by

MARIA ELIZABETH PESEK

Submitted to the Office of Graduate and Professional Studies of
Texas A&M University
in partial fulfillment of the requirements for the degree of

MASTER OF SCIENCE

Chair of Committee,	Nicholas D. Perez
Committee Members,	Michael P. Bishop
	Brent V. Miller
Head of Department,	Michael C. Pope

May 2019

Major Subject: Geology

ABSTRACT

Resolving the linkages among climate, erosion, and tectonics has implications for understanding geologic problems in deep time and in the future, yet studies yield conflicting results as to how surface and lithospheric processes drive mountain range development. The Cascade Range, NW USA is an ideal setting to assess how these drivers may guide rock uplift patterns, as structural and modern precipitation patterns have a unique along-strike spatial distribution. Orographic precipitation uniformly incises the western flank, broadly N-S compression in northern Oregon transitions to generally E-W extension in the south, and magmatism is segmented along the arc.

New single-sample multi-proxy geo- and thermochronologic methods were applied at six sample locations along the Western Cascades range. At each location, a unique geologic relationship between incised Cenozoic plutons capped by basalts provides the opportunity to reconstruct the pluton exhumation pathway from crystallization to near-surface exposure and constrain the amount of rock uplift in this region. New and existing U-Pb geochronologic data reveal pluton crystallization ages between ~10–24 Ma. Apatite (U-Th)/He ages reveal anomalously young cooling ages (~2–4 Ma) near Mount Hood, which may reflect resetting by younger volcanic flows. Some apatite and zircon (U-Th)/He ages from southern Oregon are older than the corresponding zircon U-Pb crystallization age, which may be attributed to inclusions, zoning, or ^{4}He implantation. Remaining apatite and zircon (U-Th)/He ages range from ~8–22 Ma and suggest a generally southward increase in cooling ages. ^{40}Ar/^{39}Ar geochronologic results define the eruption age of basalts that unconformably overlie the plutons, which range from ~5–8 Ma.

Existing low-temperature apatite (U-Th)/He thermochronologic results from the Washington Cascades document uniform ~6–12 Ma exhumation ages that were initially attributed to focused orographic precipitation and erosion. The diversity of ages in Oregon suggest the timing of exhumation occurred from ~7–22 Ma, which differs from the results in Washington, and generally increases from north to south. These results are more consistent with processes that demonstrate along-strike variability, such as tectonics or magmatic processes, and support the interactions of

climate, erosion, and tectonics in guiding orogen evolution.

DEDICATION

To my parents, Larry and Charlene, whose sacrifices have allowed me to pursue higher education and whose unconditional love provided the support to succeed.

ACKNOWLEDGMENTS

This journey has been by far the most challenging endeavor I have pursued, but also the most enriching and rewarding. I could not have accomplished this master's thesis without the help and support of many people along the way. First, I would like to thank my committee chair, Dr. Nicholas Perez, for his guidance on this project. I am a better geologist for having had the opportunity to learn from him both in the classroom and in the field. I would also like to thank my committee members, Dr. Michael Bishop and Dr. Brent Miller, for their guidance and support during the course of this research.

I could not have completed this thesis without the help and support of Dr. Perez's research team, including Colton Barr, Charlie Bruce, Daniela Chiriboga, Clyde Findlay, Daniel Hou, Vicky Gao, Sarah Giles, Seth Hardin, Keller Herrin, Kristina Levine, Telemachos Manos, Liam Norris, Bailey Ohlson, and Clay Rowden. In particular I would like to thank Sarah Giles for her assistance during field work, in the mineral separation process, and in HeFTy modeling. Thank you to Clay Rowden for his tremendous contribution to the mineral separation process and HeFTy modeling as well.

I would also like to thank our collaborators at Oregon State University. Thank you to Dr. Andrew Meigs for his guidance and support on this project, including assistance during field work. Thank you to Danielle Woodring for assistance during field work and for being a gracious host during my visits to Corvallis. Thank you also to Wolfgang Lopez for his guidance on the basalt sample preparation. Thank you to Elinor Utevsky and Dr. John Dilles at Oregon State University for access to their work and extra mineral separates.

I am incredibly grateful and appreciative for the help and guidance of the lab managers and coordinators that worked with us to obtain these data. Thank you in particular to Dr. Kip Hodges, Dr. Matthijs van Soest, and Michelle Aigner at the Arizona State University Group 18 Laboratory and to Dr. Dan Miggins at the Oregon State University Argon Geochronology Laboratory. Thank you also to Dr. Brent Miller at the Texas A&M Radiogenic Isotope Geosciences Facility. Thank you to Dr. Daniel Stockli and Dr. Rudra Chatterjee at the University of Texas UTChron Laboratory for their work on the preliminary data for this study.

This thesis would not have been possible without the generous funding support from the following sources: the Bush Foundation Graduate Student Travel Grant, the GSA Graduate Student Research Grant, and the GSA On To the Future travel award. The National Petrographic Service provided thin sections of the samples collected during this study.

Lastly, thank you to my parents for their unconditional love and for many early-morning trips to the airport heading to field work, lab work, and conferences. I would not be where I am today without their support. Thank you also to my brothers, sister, sisters-in-law, and brother-in-law for their support over these past few years and for listening to me talk about rocks. Thank you to my best friend and the love of my life, Ivan Vazquez, who has been with me during every step of this journey and inspires me to achieve my dreams.

CONTRIBUTORS AND FUNDING SOURCES

Contributors

Committee members that provided supervision on this thesis include Dr. Nicholas Perez and Dr. Brent Miller of the Department of Geology & Geophysics and Dr. Michael Bishop of the Department of Geography.

Some of the data discussed in Section 4 were provided by work previously completed by Dr. Nicholas Perez of Texas A&M and Dr. Andrew Meigs of Oregon State University in 2017. Mineral separates for these samples were provided by Elinor Utevsky and Dr. John Dilles of Oregon State University. Apatite and zircon (U-Th)/He analyses were conducted at the University of Texas UTChron Lab with the assistance of Dr. Daniel Stockli and Dr. Rudra Chatterjee.

Apatite and zircon (U-Th)/He and zircon U-Pb analyses for this study were conducted at the Arizona State University Group 18 Laboratory with the assistance of Dr. Kip Hodges, Dr. Matthijs van Soest, and Michelle Aigner. Basalt groundmass $^{40}Ar/^{39}Ar$ analyses were conducted at the Oregon State University Argon Geochronology Laboratory with the assistance of Dr. Dan Miggins. Additional zircon U-Pb and apatite U-Pb analyses were conducted at the Texas A&M University Radiogenic Isotope Geosciences Facility with the assistance of Dr. Brent Miller.

Sarah Giles assisted with sample collection during field work, the mineral separation process, and HeFTy modeling. Clayton Rowden assisted with the mineral separation process and HeFTy modeling. Charles Bruce, Daniel Hou, Kristina Levine, and Liam Norris also assisted with the mineral separation process. Clyde Findlay and Telemachos Manos provided training on the mineral separation machines and techniques. Wolfgang Lopez provided guidance on the basalt sample preparation. Danielle Woodring and Dr. Andrew Meigs provided additional assistance with sample collection during field work.

All other work contributing to this thesis was conducted by the student independently.

Funding Sources

Graduate study was supported by the Marathon Scholarship and the M.T. Halbouty '30/AAPG Foundation Endowed Fellowship granted through the Texas A&M University Department of Geology & Geophysics.

This work was also made possible through funding from the Bush Foundation Graduate Student Travel Grant, the GSA Graduate Student Research Grant, and the GSA On To the Future travel award. Additional funding support was provided by Dr. Nicholas Perez.

TABLE OF CONTENTS

LIST OF FIGURES

LIST OF TABLES

1. INTRODUCTION

A fundamental problem in Earth science is understanding the interactions between surface and tectonic processes, and the relative contribution of each factor to the development of topography. Resolving how climate, erosion, and tectonics interact has potential implications for understanding how natural hazards, including landslides, develop and how sediment is eroded and transported into drainage networks. The NSF Tectonics community recently highlighted this problem as a major grand challenge for future research (Huntington et al., 2017). Some studies have framed this debate in the context of either climate or tectonic processes drive rock uplift (Burbank et al., 2003; Forte et al., 2016), but other efforts emphasize the interactions among these processes (Hodges et al., 2004; Willett, 1999).

The feedback relationships among climate, erosion, and tectonics remain debated. For example, the Southern Alps of New Zealand and the Olympic Mountains in Washington have similar subduction orientations and precipitation patterns, but numerical models predict different topographic and exhumation profiles between the two regions (Willett, 1999). These different profiles highlight the role of primary wind direction and focused precipitation as key controls on prowedge-focused erosion (in the case of the Olympic Mountains) or retrowedge-focused erosion (in the case of the Southern Alps), suggesting surface processes compete with subduction processes as dominant controls on orogen evolution.

Field studies yield more varied results with regard to the contribution of subduction polarity, deformation, and surface processes to rock uplift. Both climate and structural drivers have been interpreted as the dominant controls on rock uplift to explain exhumation records from the Marsyandi River catchment in Nepal. The correlation of Quaternary deformation patterns with precipitation patterns supports a component of climate-driven exhumation (Hodges et al., 2004), yet erosion and upward movement are spatially consistent, which supports structural drivers (Burbank et al., 2003). In the Caucasus mountain range, erosion rates constrained from topographic metrics and low-temperature bedrock thermochronologic results suggest that large-scale changes in the climate gradient do not control the topography in Western Asia (Forte et al., 2016). This implies that in the Caucasus, on the time scale of millions of years, tectonic processes are the main drivers of rock uplift (Forte et al., 2016). The diversity of conclusions found in these studies emphasize that the nature and presence of interactions between surface and lithospheric processes remain uncertain. This is potentially due to some regions, such as the Himalayas and the Southern Alps, having deformation and precipitation patterns that covary spatially, which makes disentangling the relative contributions from each factor difficult.

Integrated geochronology and thermochronology analyses combined with geodynamic models are needed to produce detailed exhumation histories in order to address the debate regarding the driving forces of mountain range development (Huntington et al., 2017). This study reconstructs the cooling history of the Cascade Range in Oregon and southern Washington by integrating thermochronologic and geochronologic data from bedrock samples of plutons and basalts. The Cascade Range provides an excellent setting to independently assess contributions from climate and tectonic processes on orogen evolution, as the unique structural and precipitation trends along this portion of the range have not covaried over the past 15–30 million years. This study focuses on six sites along the Cascade Range that are situated across multiple structural and volcanic domains yet remain within the same modern and ancient orographic precipitation zone along the western Cascade flank. These distinct along-strike trends allow the investigation of whether spatial patterns of exhumation are aligned with deformation or climate processes because they do not co-vary spatially compared to regions in other studies.

Low-temperature bedrock thermochronological data from the Washington Cascades have been used to argue for climate-modulated rock uplift. Apatite fission track and (U-Th)/He thermochronologic results from plutonic rocks in Washington suggest initially slow cooling throughout the Oligocene followed by a pulse of rapid exhumational cooling during the middle Miocene on the western flank of the Cascades, where cooling ages range from ~6–12 Ma (Reiners et al., 2002). The timing of increased rock uplift rate is similar to the Coast Mountains in Alaska, where accelerated exhumation began at ~10 Ma (Hickes et al., 2000; Hickes, 2001). Farther north in the

St. Elias Mountains of Alaska, convergence in the Yakutat Terrane has been constant since ~6 Ma (Gulick et al., 2013, 2015; Pavlis et al., 2012; Worthington et al., 2012), which is consistent with these studies (Hickes et al., 2000; Hickes, 2001; Reiners et al., 2002). Reiners et al. (2002, 2003) reasoned that although Washington and Alaska exhibit different tectonic and deformation patterns, both are affected by similar orographic precipitation patterns. They interpreted synchronous timing of accelerated uplift in the Alaska Coast Mountains and the Washington Cascades, coupled with the spatial correlation between increased rock uplift rates and regions of increased precipitation and erosion rates in the Washington Cascades, as evidence that regional climate guided exhumation patterns (Reiners et al., 2002, 2003). In contrast, thermochronologic data from the eastern flank of the Washington Cascades suggests Miocene exhumation was driven by crustal shortening and that precipitation and erosion rates alone were not sufficient to erode volumes required to expose basement bedrock (Enkelmann et al., 2015). Additionally, eroded volume studies in the Santiam drainage of the Oregon Cascades show that fluvial incision and erosion alone were insufficient to account for the total rock uplift in this area (Lopez and Meigs, 2016). The eroded volume since 6.3 Ma was calculated using the relationship between paleo-valley markers and the present-day valley bottoms, and the resulting amount of rock uplift was determined assuming a perfectly isostatic model, a continuous plate flexural model, and a broken plate flexural model (Lopez and Meigs, 2016). The broken plate flexural model, which most accurately represents the setting of the Oregon Cascades, results in an average of 262.5 ± 87.5 m of rock uplift in the core of the range using an estimated value of 10 km for the elastic thickness (Lopez and Meigs, 2016). Simple isostasy can account for ~55% of the present-day elevation difference between the paleo-valley markers and the valley bottom, while the plate flexure models suggest only ~36% of rock uplift can be attributed to erosion (Lopez and Meigs, 2016). The study presented here tests the existing hypotheses that exhumation is guided by regional precipitation and climate patterns (Reiners et al., 2003) by extending the thermochronology dataset to include the segment of the Cascades in southern Washington and Oregon and comparing the along-strike timing of exhumation.

The value of using multiple geo- and thermochronometers on the same sample is also explored as a means of distinguishing between magmatic cooling processes and the true exhumation signal. Low-temperature thermochronometers often yield a wide range of cooling ages, which can be difficult to interpret (Fitzgerald et al., 2006). This study additionally explores how to model a dataset with dispersion of apatite and zircon (U-Th)/He ages and which models may be most representative of the true cooling history.

Here we present results from integrated geochronology and multiple low-temperature thermochronometers to investigate 1) the timing of exhumation in the Oregon Cascades, 2) whether the timing of exhumation in the Oregon Cascades is consistent with existing results from Washington, and 3) how the spatial pattern of exhumation compares with spatial trends in deformation and precipitation.

2. GEOLOGIC BACKGROUND

2.1 Geologic Setting

The Cascade Range is the volcanic arc associated with subduction of the Juan de Fuca plate underneath North America and spans British Columbia to northern California (Figure 2.1) (Wells and McCaffrey, 2013). Arc volcanism in Oregon and Washington began ~40–45 Ma, approximately 10 Ma after the accretion of the Siletzia microplate associated with the final phases of the Laramide orogeny (Schmandt and Humphreys, 2011). Cenozoic volcanic rocks of the Cascade Range are composed of two provinces: the High Cascades and the Western Cascades (du Bray and John, 2011). The High Cascades province represents the modern active volcanic arc that erupted since ~4 Ma. Underlying and to the west of the High Cascades are the Western Cascades, which represent magmatism associated with the ancestral arc from ~4–45 Ma (du Bray and John, 2011). The northern segment of the ancestral arc is not well-defined, but is believed to terminate north of Mount Rainier in central Washington (Christiansen and Yeats, 1992; Duncan and Kulm, 1989; Vance et al., 1987). The southern segment of the ancestral arc spans from Mount Rainier to Mount Shasta in northern California, west of the modern High Cascade range (du Bray and John, 2011). This segment of the ancestral arc was formed as the subduction angle steepened after the Eocene (du Bray and John, 2011).

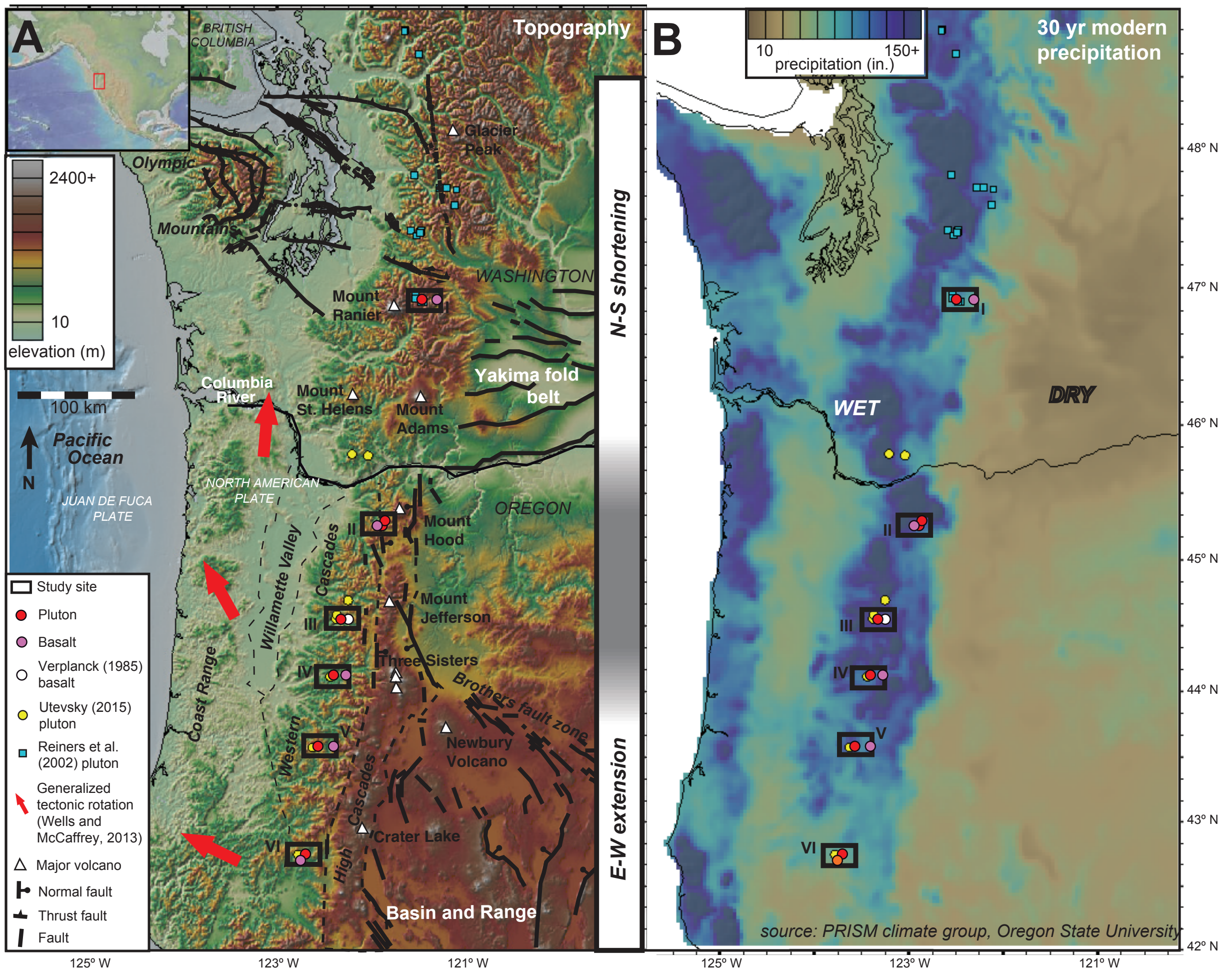

Figure 2.1: Field study area showing sample locations, structural and tectonic features of interest (A), and modern precipitation gradient (B). Note existing sample locations.

2.2 Magmatic Trend

The timing and distribution of arc magmatism has varied (Figure 2.2). From 36 Ma to before 40 Ma, the arc was active in southern Washington and produced basalt, andesite, and basaltic andesite magmatic compositions (du Bray and John, 2011). From 18 to 35 Ma, the arc was active in both Washington and Oregon, and magmatic compositions also included rhyolite and dacite (du Bray and John, 2011; Priest, 1990). From 8 to 17 Ma, magmatism was focused along the northern two-thirds of Oregon and returned to more mafic compositions (du Bray and John, 2011; Priest, 1990). Magmatic compositions were primarily basalt and basaltic andesite from 4 to 8 Ma, and magmatic activity remained focused in Oregon and northern California (du Bray and John, 2011; Priest, 1990). High Cascades volcanism began at ~4 Ma and included magmatic compositions of basalt, basaltic andesite, and silicic ash flows. (du Bray and John, 2011; Priest, 1990).

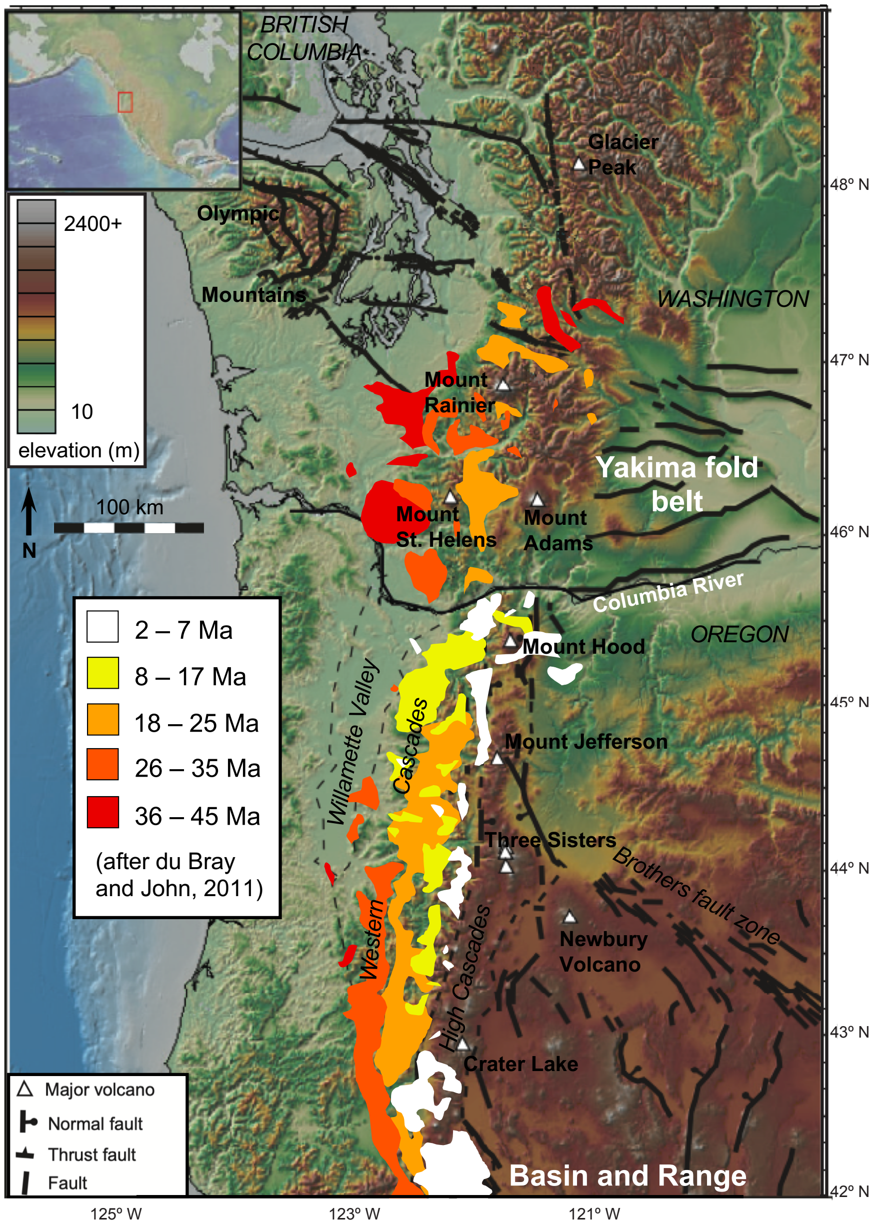

Figure 2.2: Location of magmatic arc in Oregon and Washington from 2–45 Ma, modified from du Bray and John (2011).

2.3 Deformation Trend

The deformation style varies along the Cascade Range (Reiners et al., 2002). Combined clockwise vertical axis rotation and northward motion of western Oregon result in north-south shortening in the Yakima Fold Belt of southern Washington, which was established at least by the mid-Miocene (Swanson and Wright, 1976; Wells and McCaffrey, 2013). Evidence for Miocene and Pliocene deformation associated with the Yakima Fold Belt is recorded in the Columbia River Basalt Group (6–17.5 Ma) (Blakely et al., 2011). South of the Yakima Fold Belt, deformation decreases, and northern Oregon exhibits a neutral setting. In southern Oregon, northwest-southeast extension is associated with the northernmost Basin and Range province (Figure 2.1) (Wells and McCaffrey, 2013). Normal faulting associated with Basin and Range extension began at ~12 Ma in southern Oregon (Dilles and Gans, 1995; Colgan et al., 2004; Surpless et al., 2002; Trench et al., 2012).

Paleomagnetic data support that western Oregon has rotated about a vertical axis at 1.19 ± 0.1 °/m.y. throughout most of the Cenozoic (Wells and McCaffrey, 2013). GPS observations from the past 15 years reveal vertical axis rotation rates that are consistent with those determined from paleomagnetic data (McCaffrey et al., 2007). The consistency between the long-term paleomagnetic data and short-term, decadal geodetic data rotation rates suggests that the cause is permanent motion in the upper plate, as opposed to elastic strain or earthquake-induced effects that are time-dependent (Wells and McCaffrey, 2013). Near Mount Baker in Washington, a series of stocks and calderas that are progressively older to the northeast reveal a magmatic migration rate of 6.0 mm/yr, of which 3.5 mm/yr can be attributed to block motion (Wells and McCaffrey, 2013). In Oregon, Miocene plutons that are offset to the northwest, in the direction of the current plate motion, reveal magmatic migration rates of 3.1 mm/yr to 3.5 mm/yr in northern and southern Oregon, respectively (Wells and McCaffrey, 2013). GPS rates at these same locations are 4.1 mm/yr and 7.7 mm/yr, respectively (Wells and McCaffrey, 2013). The difference between the magmatic migration rates and GPS rates is attributed to an additional component of westward arc migration driven by slab rollback, where rollback occurs in the opposite direction of block motion in Washington and rollback and block motion are both to the west in Oregon (Wells and McCaffrey, 2013).

2.4 Precipitation Trend

A modern orographic precipitation gradient results in relatively uniform mean annual precipitation as high as 4.0 m/yr (Figure 2.1) (Reiners et al., 2003; Wells and McCaffrey, 2013). The eastern flank of the Cascade Range is situated in a rain shadow and receives 0.2 m or less of precipitation per year (Reiners et al., 2003). The timing of the development of this orographic precipitation gradient remains debated. A decrease in $\delta^{18}O$ compositions of fossil equid (horse) teeth support a monotonic increase in elevation of the Oregon Cascades and subsequent rain shadow developments in two periods: from ~27 Ma to 15.4 Ma and after 7.2 Ma (Kohn et al., 2002). Oxygen and carbon isotope dating of authigenic smectites and pedogenic carbonates along the eastern flank of the southern Washington Cascades suggest rain shadow development occurred between ~5–15 Ma (Takeuchi and Larson, 2005; Takeuchi et al., 2010). Paleoenvironmental interpretations based on volcanic glass support Cascade topography has existed since at least the mid-Miocene and potentially as early as the Oligocene (J. Bershaw, personal communication, 2018).

2.5 Exhumation and Erosion Rates

Apatite (U-Th)/He ages of samples from the western flank of the Washington Cascades range from ~6–12 Ma, which support a period of rapid cooling occurring during the late Miocene (Reiners et al., 2002). Younger apatite (U-Th)/He ages (1–5 Ma) at other locations suggest localized younger cooling. Age-elevation transects reveal an apparent exhumation rate of 0.5–1.0 km/m.y. during the late Miocene (Reiners et al., 2002). On the eastern flank, rapid cooling occurred in the early Tertiary followed by slow exhumation throughout the Oligocene (~0.2 km/m.y.) based on apatite (U-Th)/He ages and fission track ages (Reiners et al., 2002).

Reiners et al. (2003) calculated erosion rates in the Washington Cascades using numerical modeling that related apatite (U-Th)/He ages to closure temperature and depth based on parameters such as the geothermal gradient, He diffusion kinetics, and depth to constant temperature. Erosion rates on the eastern flank and near the topographic crest ranged from 0.02–0.04 km/m.y., and the erosion rate two-thirds up the western flank was 0.33 km/m.y. The average erosion rate across the Washington Cascades was 0.10 km/m.y., and those authors assumed exhumation was driven by erosional unroofing due to the lack of obvious, active structures in the Washington Cascades that could have driven exhumation by other mechanisms.

2.6 Seismicity

The Cascade arc can be subdivided into three regions that relate to modern seismicity: the northern compressional arc (western Washington and Vancouver Island), the central extensional arc (southwestern Washington and western Oregon), and the southern transtensional arc (northern California) (Wells et al., 2002). The northern compressional arc and the southern transtensional arc are seismically active in the lower and upper plates today, while the central extensional arc exhibits anomalously low seismicity (Wells et al., 2002). The lack of in-slab earthquakes in southwestern Washington and western Oregon could be due to 1) a decrease in convergence rate between 47 °N and 46 °N or 2) a low stress environment in the subducting plate (Wells et al., 2002). Evidence of a low stress environment under Oregon can be found in the slab thickness under the continent. In Washington, the slab can be teleseismically imaged to depths of ~500 km while in Oregon no deeper slab is seen below ~150 km (Rasmussen and Humphreys, 1988). If there is no deeper slab under Oregon, then slab-pull forces would be less, leading to a lower stress environment (Wells et al., 2002).

3. METHODS

3.1 Sample Lithologies and Geologic Relationship

The unique geologic relationship of Cenozoic plutons exposed in incised fluvial valleys situated below ridge-capping basalts allows for the reconstruction of a multipart exhumation pathway from pluton crystallization to near-surface exposure (Figure 3.1–3.2). The hypidiomorphic-granular petrographic texture of the plutons suggests they were shallowly emplaced at depths of less than 5 km (Dilles, 1987; Utevsky, 2015). Further evidence for shallow emplacement of the Western Cascades plutons comes from below average $\delta^{18}O$ values that suggest hydrothermal interaction with meteoric water (Taylor Jr., 1971). The basalts were interpreted as flowing down paleo-river valleys because they often cap fluvial gravel deposits (Conrey et al., 2002). Topographic inversion has resulted in the basalts now situated along modern ridges, and the plutons are exposed in modern river valleys (Conrey et al., 2002). The difference in elevation between the plutons and ridge-capping basalts range from 665–847 m across the sample locations in this study. This geologic relationship demonstrates that the plutons were exhumed to depths of 665–847 m beneath the earth's surface by the timing of basalt emplacement. Sites V and VI are the exceptions, where the pluton is located at a higher elevation compared to the ridge-capping basalt. Sample 17OR-12 at Site II was not a ridge-capping basalt, but rather a basaltic sill, plug, or dike that fed the ridge-capping basalt flows. Sample 17OR-04 collected at Site V is an upper – middle Miocene lava flow as opposed to the Pliocene – upper Miocene ridge-capping basalt unit.

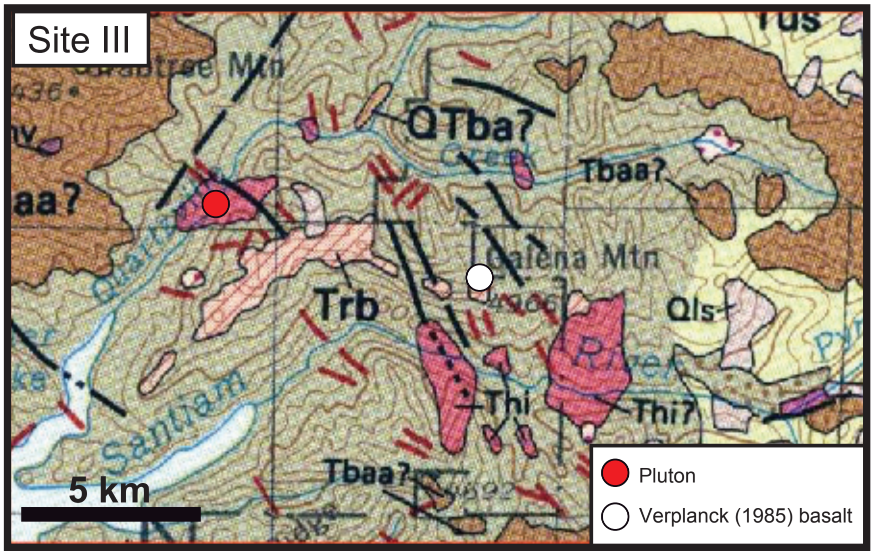

Figure 3.1: Geologic map inset of Site III showing relationships between plutons (Thi), ridge-capping basalts (Trb), and fluvial incision. Basalts are located on ridges present-day, and plutons are exposed in river valleys. Map modified after Walker and MacLeod (1991).

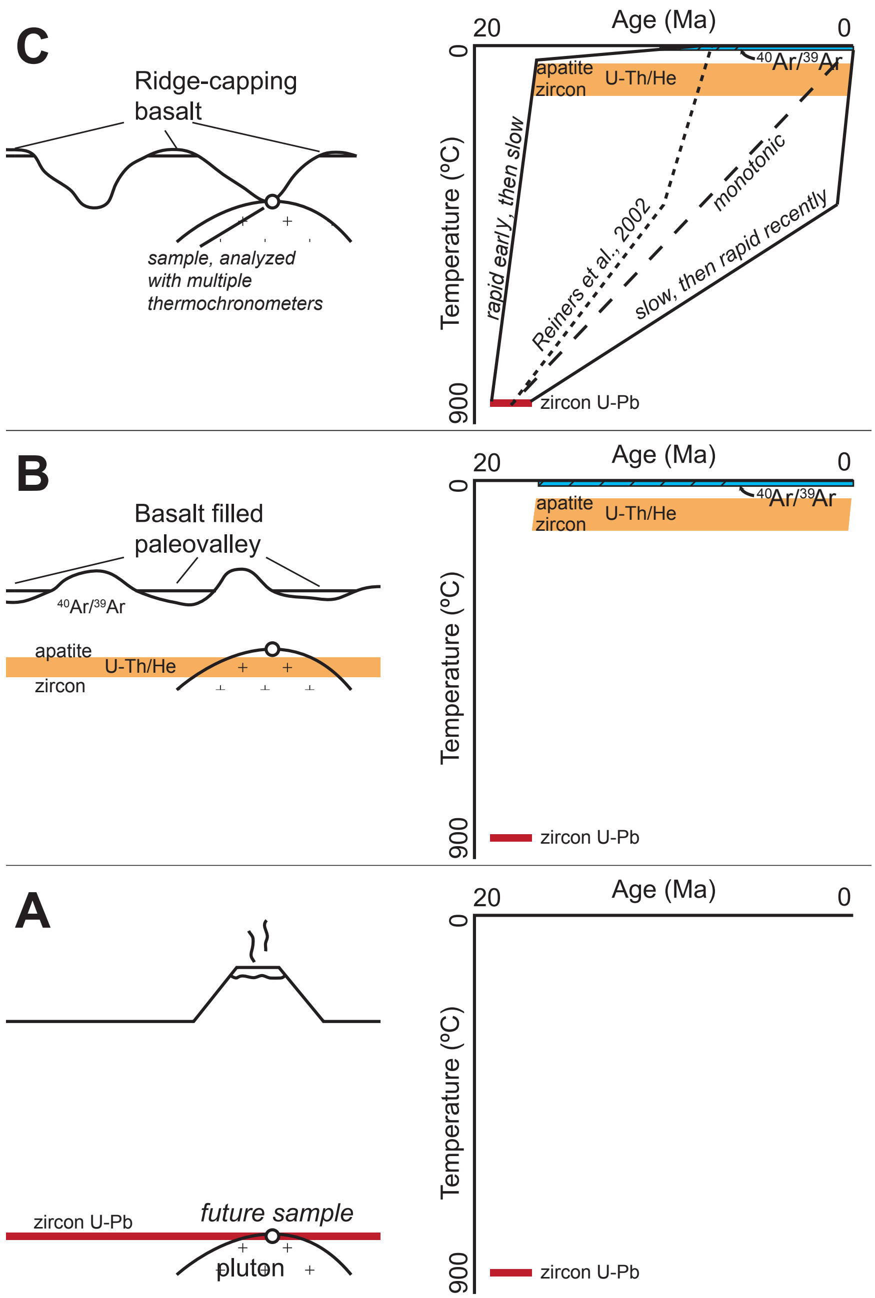

Figure 3.2: Schematic diagram illustrating geologic model and construction of time-temperature pathway diagrams, with the youngest time represented in A and oldest in C. Zircon U-Pb ages provide pluton crystallization constraint (A), zircon and apatite (U-Th)/He ages provide cooling constraints (B), and basalt groundmass ^{40}Ar/^{39}Ar ages provide a minimum constraint on when the plutons were near the surface (C). The slope of the line between these points determines the pace of exhumation, where a steep slope indicates a rapid cooling pathway and a shallow slope indicates a slow cooling pathway.

3.2 Geochronology and Thermochronology

The geochronology and thermochronology methods used include zircon U-Pb, apatite and zircon (U-Th)/He, and basalt groundmass $^{40}Ar/^{39}Ar$, which provide constraints on the crystallization age, the timing of exhumation, and when the pluton was within ~600–900 meters of the surface, respectively. This approach is unique in that the potential for combining multiple thermochronometers allows for the calculation of cooling rates for individual samples. However, the ages obtained from these systems only constrain the amount of rock uplift in this region since the early to mid-Miocene, and the contributions to surface uplift and erosion of pre-existing topography are not evaluated. The following sections describe each of these systems in more detail.

3.2.1 Zircon U-Pb Geochronology and Ti-in-zircon thermometry

Zircon U-Pb geochronology determines the age of pluton crystallization. U and Th decay to Pb with time, and the concentrations of the parent and daughter isotopes can be measured using laser ablation inductively coupled plasma mass spectrometers (LA-ICP-MS) (Gradstein et al., 2012). Four sources of error that must be accounted for in the final age uncertainty in addition to measurement error include the elemental fractionation correction, the common Pb correction, the uncertainty in the reference standard age, and the uncertainty of ^{238}U, ^{235}U, and ^{232}Th decay constants (Thomson et al., 2012). To account for the differential fractionation of U, Th, and Pb during the laser ablation process, a suitable reference standard must be selected (Thomson et al., 2012). Ideally the reference standard should have a similar composition and ablation characteristics to the unknown sample, but the variability in initial Pb adds to the uncertainty of the final age (Thompson et al., 2016). Common lead refers to nonradiogenic lead laboratory contamination and/or nonradiogenic lead incorporated into the crystal during its formation, which is measured as the ^{204}Pb concentration (Andersen, 2002). The ^{206}Pb, ^{207}Pb, and ^{208}Pb radiogenic isotope measurements are then corrected using their relative abundances in proportion to the common lead (Andersen, 2002).

Ti-in-zircon thermometry constrains the zircon pluton crystallization temperature, and existing results from Utevsky (2015) were used in this study during HeFTy modeling. The titanium content in zircon crystals that coexists with rutile and other Ti-rich mineral phases is strongly dependent on temperature (Degeling, 2003; Troitzsch and Ellis, 2004, 2005; Watson et al., 2006; Zack et al., 2004). Ti concentration in zircon crystals can be measured during SHRIMP-RG and LA-ICP-MS analyses, and the methods used by Utevsky (2015) follow those of Ferry and Watson (2007).

3.2.2 Apatite and Zircon (U-Th)/He Thermochronology

Thermochronology is the study of a rock's thermal history as it is advected to the Earth's surface. Multiple thermochronometer systems exist, which can be used to determine the timing at which specific minerals pass through corresponding closure temperatures (Dodson, 1973). This study focuses on low-temperature apatite and zircon (U-Th)/He systems. As a simplified definition, the closure temperature represents the boundary below which diffusion of the daughter product from the system occurs and above which the daughter product is retained in the system, although the transition is gradual (Dodson, 1973). The partial retention zone refers to the range of temperatures in which He diffusivity is variable. At temperatures greater than ~85 °C, apatite grains do not retain He, and at temperatures less than ~40 °C, the apatite retains He fully (Wolf et al., 1998). For grains that have remained within the partial retention zone for an extended amount of time, the measured isotope concentrations may not reflect the true age of the sample. Therefore, one must have a constraint on the sample, such as an age-elevation transect, multiple thermochronometers, or an accurate diffusion model.

As U and Th isotopes decay to Pb in apatite or zircon grains, He is emitted as an alpha particle and retained within the crystal lattice at temperatures of ~40–85 or ~180–200 °C in apatite and zircon, respectively. The concentrations of the radiogenic ^{4}He and U, Th, and Sm are obtained through heating and de-gassing intervals or by laser ablation methods (Boyce et al., 2006; Shuster and Farley, 2005). The resulting (U-Th)/He ages can be modeled to constrain the timing of exhumation. One complication of this method arises if an alpha particle less than 20 μm from the grain edge gains sufficient energy to eject from the grain, resulting in an age that appears younger than the true age of the sample (Farley et al., 1996; Shuster and Farley, 2005). The α-ejection correction can be computed by dividing the age calculation by the α-retention factor F_t, which is determined by a polynomial equation outlined in (Farley et al., 1996).

The closure temperature for apatite depends on the grain size and cooling rate, where a grain of a larger half prism width, such as 100 μm, cooled under a fast rate, such as 15 °C/Myr, will have a higher closure temperature (~75 °C) than a grain of a smaller half prism width, such as 50 μm, cooled under a slower rate, such as 5 °C/Myr, which results in a closure temperature of ~57 °C (Farley, 2000). A limitation of this method concerns defects in the crystal structure as a result of naturally-occurring radioactivity (Ewing et al., 1995; Weber et al., 1998). Shuster et al. (2006) consider radiation damage to be the most important control on helium diffusivity, wherein helium diffusion is hindered by "traps" in the crystal structure and accumulates in excess concentrations. The radiogenic ^{4}He concentration was used as a proxy for radiation damage in this model, called HeTM, resulting in a variation of closure temperatures over time (Shuster et al., 2006). Higher effective uranium concentrations [eU] (ppm) correspond to the formation of more damage traps, and in turn higher closure temperatures, where [eU] = [U] + 0.234[Th] + 0.0047[Sm] (Shuster et al., 2006). The radiation damage accumulation and annealing model (RDAAM) developed by Flowers et al. (2009) builds on the HeTM model but uses effective fission-track density rather than He concentration as a proxy for radiation damage. They propose this model produces more accurate (U-Th)/He ages, as He concentration and radiation damage do not correspond proportionally in all cases (Flowers et al., 2009).

3.2.3 Apatite U-Pb Thermochronology

Apatite is suitable for U-Pb thermochronology as it contains sufficient amounts of lattice-bound uranium (Chew et al., 2011; Harrison et al., 2002; Willigers et al., 2002). This system has a closure temperature of ~450–500 °C for both rapid and slow cooling rates (Chamberlain and Bowring, 2002; Willigers et al., 2002). This system follows the same methods and corrections as described in the zircon U-Pb system (Section 3.2.1).

3.2.4 Basalt Groundmass ^{40}Ar/^{39}Ar Geochronology

^{40}Ar/^{39}Ar geochronology of basalt groundmass constrains the emplacement age of the basalts that unconformably overlie the plutons. ^{40}K decays to ^{40}Ar over time, and the concentrations of the parent and daughter isotopes can be used to determine the age of the sample through the decay equation and constants outlined by Renne et al. (2010). The parent ^{40}K undergoes neutron bombardment to convert to ^{39}Ar so the parent and daughter concentrations can be measured using the same instrumentation (Harrison and Zeitler, 2005). The parent and daughter concentrations are obtained through heating the grain in increments and measuring the contents of the gas released (Harrison and Zeitler, 2005). The diffusive loss of ^{40}Ar, if present, can be determined by the pattern produced by comparing the percent of ^{39}Ar released at incremental heat steps and the ^{40}Ar/^{39}Ar age. A sample that has been undisturbed since initial crystallization yields a horizontal linear age spectrum, whereas a sample that has experienced ^{40}Ar loss produces a “stair-step” pattern with a span of ^{40}Ar/^{39}Ar ages (Harrison and Zeitler, 2005). A variable, non-linear age spectrum pattern can result through the process of argon recoil (Figure 3.3). During the irradiation process but before sample analysis, the kinetic energy released during neutron bombardment can cause the converted ^{39}Ar atom to be ejected to neighboring phases (McDougall and Harrison, 1999). This phenomenon occurs more often in fine-grained material and glass, and the resulting age spectrums are difficult to interpret for an accurate ^{40}Ar/^{39}Ar age.

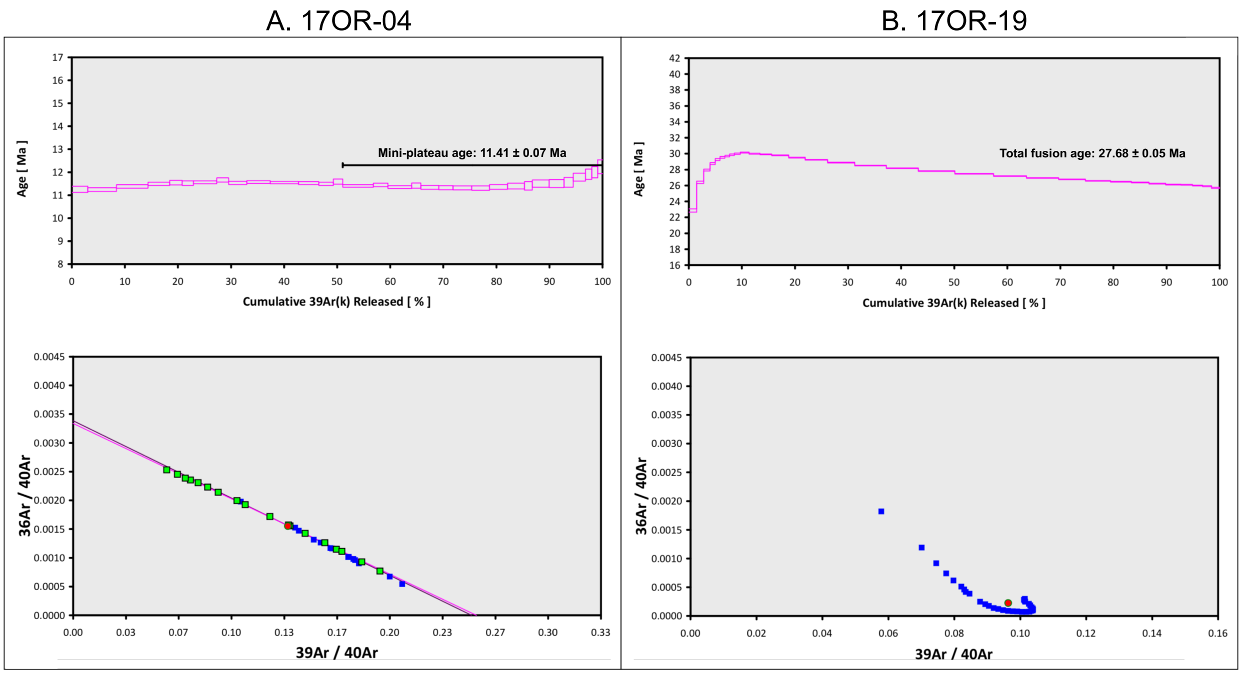

Figure 3.3: A) ^{40}Ar/^{39}Ar age spectrum for basalt sample 17OR-04 that is well-behaved and produces a mini-plateau age of 11.41 ± 0.07 Ma. B) ^{40}Ar/^{39}Ar age spectrum for basalt sample 17OR-19 that produces a non-linear pattern, characteristic of argon recoil, in which the total fusion age of 27.68 ± 0.05 Ma is the best estimate for the age of the sample.

3.3 Sample Preparation

Seven pluton samples and seven basalt samples were collected at six locations spanning from southern Oregon to southern Washington (Figure 2.1). Weathered surfaces were removed before the following mineral separation steps.

3.3.1 Pluton Samples

Pluton samples were crushed with a large jaw-crusher, disc milled, and sorted by gravity using a Wilfley table. Magnetic minerals from the heavy fractions were separated at intervals of .2, .5, .8, 1.0, 1.2, and up to 1.5 amps using a Frantz magnetic separator. The nonmagnetic fractions were sorted by density using bromoform and methylene iodide to separate apatite and zircon fractions. A pyrite dissolution procedure was performed on the MEI heavy fractions of samples 17OR-06 and 17OR-09, where the fractions were heated to ~70 °C with water before adding nitric acid.

Apatite and zircon grains were handpicked using a binocular microscope. Apatite grains were selected for dating based on size, geometry, and presence of inclusions (see Appendix Table A.1 for individual grain dimensions). Ideal grains exhibited two euhedral ends, however in some cases only one euhedral end or no euhedral ends were present. Many of the apatite crystals contained inclusions, and in these cases the crystals with the smallest and least amount of inclusions were selected for dating. Zircon grains were primarily selected based on grain size. Figure 3.4 shows microphotographs of some selected crystals. Some plutons did not yield both apatite and zircon grains.

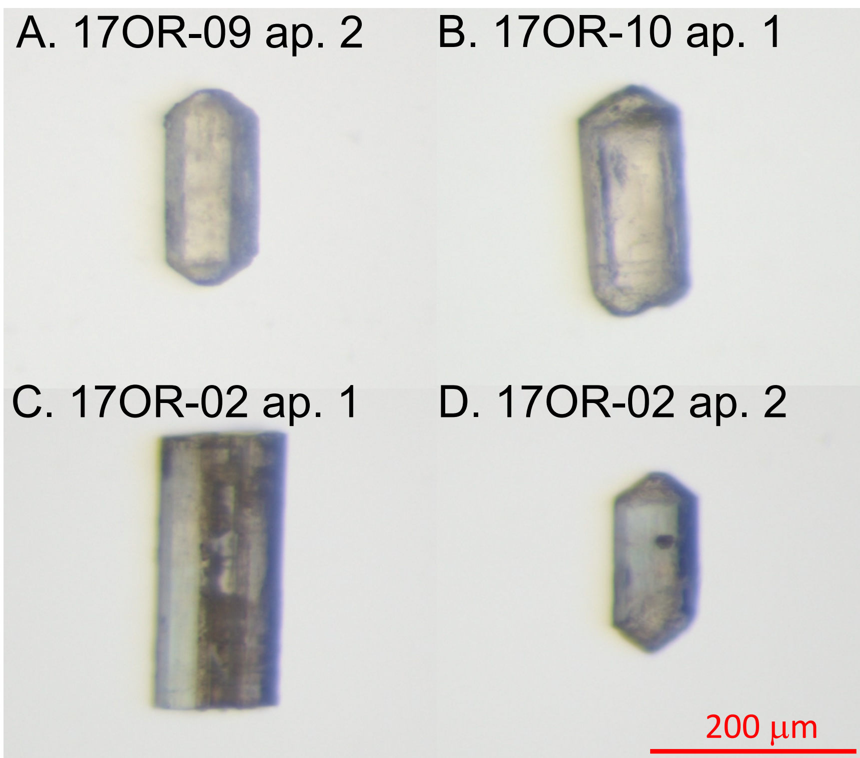

Figure 3.4: Selected microphotographs of apatite crystals. Ideal grains (A-B) had two euhedral ends and few inclusions. Non-ideal grains did not have euhedral ends (C) or contained inclusions (D).

3.3.1.1 Apatite (U-Th)/He Analyses

Four to five apatite grains from samples 17OR-02, 17OR-03, 17OR-09, 17OR-10, and 17OR-18 were selected for dating by conventional (U-Th)/He analyses. The length and width dimensions of the individual grains were measured prior to analysis in order to make the α-ejection correction. Each grain was packed in a niobium microcrucible, which was then crimped on both ends. Apatite (U-Th)/He analyses were conducted at the Group 18 Laboratory at Arizona State University using the ASI Alphachron. The (U-Th)/He methods used in this study follow that described in the supplementary material of van Soest et al. (2011). A 45 Watt, 980 nm infa-red diode laser was used to extract helium from the apatite grains, and exposure to a hot SAES NP-10 getter cleaned any reactive gases. To determine the unknown ^{4}He in each sample, a known ^{4}He aliquot was spiked with ^{3}He in between the analyses of each sample. Durango fluorapatite was used as the age standard.

After extracting the He, the grains were then dissolved in preparation for the U-Th analysis. Each apatite grain in a Pt capsule was put into 2 ml polypropylene vials, and the grains were dissolved using 25 μl of 50% nitric acid. The spike used during this process includes ^{149}Sm-^{232}Th-^{233}U-^{236}U as opposed to that mentioned in the van Soest et al. (2011) supplementary information. The ThermoElectron X-series ICP-MS at Arizona State University was used to measure the U and Th concentrations. The ^{235}U concentration were derived from the measured ^{238}U concentration using the known ratios of these isotopes that occur in nature. The raw apatite ages were corrected for alpha ejection after Farley et al. (1996).

3.3.1.2 Zircon (U-Th)/He and U-Pb Analyses

Five to seven zircon grains from samples 17OR-06, 17OR-10, 17OR-11, and 17OR-18 were selected for dating by laser ablation U-Pb and (U-Th)/He methods. The advantage of the laser ablation method over the conventional method described in Section 3.3.1.1 is that the α-ejection correction is not needed and broken or non-euhedral grains can be analyzed (Tripathy-Lang et al., 2013). The analytical procedures for zircon laser ablation (U-Th)/He and U-Pb analyses used in this study follow those of Horne et al. (2016). The zircon grains were mounted in a puck using

Torr Seal and then polished to erode 20–30 μm of the crystals. Cathodoluminescence (CL) and backscatter electron (BSE) imaging were conducted on the puck before re-polishing to aid in selecting inclusion-free regions of the grain during analyses (Horne et al., 2016). Laser ablation analyses were conducted at the Group 18 Laboratory at Arizona State University using the Analyte G2 laser system. To measure the ^{4}He concentrations, a 25 μm spot size was selected for the zircons, and the grains were ablated for 15 seconds with a 10 Hz pulse frequency. ^{4}He concentrations were measured after ablation and gas purification using the ASI Alphachron analytical system and a Pfeiffer-Balzers Prisma quadrupole mass spectrometer. An ADE PhaseShift MicroZAM interferometric microscope was used to measure the volume of the ablated pit and the ^{4}He concentration with an in-house Matlab script (Horne et al., 2016).

The parent isotopes were measured by LA-ICPMS using the Analyte G2 laser system with a Photon Machines HelEx Active two-volume ablation cell and a Thermo Scientific iCAP Q quadrupole mass spectrometer (Horne et al., 2016). The same spots from the ^{4}He analyses were ablated for 40 seconds, increasing the spot sizes to ~40–45 μm and the laser pulse frequency to 10 Hz. The volume of the ablated pit was determined using the same interferometric microscope and software as the ^{4}He analyses. Age standards used include Plesovice (337.13 ± 0.37 Ma) (Sláma et al., 2008) and 94–35 (55.5 ± 1.5 Ma) (Klepeis et al., 1998).

Two zircon grains from sample 17OR-02 were dated by LA-ICP-MS at the Texas A&M Radiogenic Isotope Geosciences Facility for U-Pb analyses. Grains were mounted in a 25 cm diameter puck using EpoThin Epoxy Resin, which was then polished to remove approximately half of the crystal. U-Pb analyses were conducted on the iCAP Inductively Coupled Plasma Mass Spectrometer. The zircon grains were ablated for 30 seconds using a spot size of 30 μm. The primary standard used was 91500 and secondary standards were FC-1 and Plesovice. The final ages were calculated using Iolite (Igor Pro) data reduction software.

3.3.1.3 Apatite U-Pb Analyses

Apatite U-Pb analyses were conducted at the Texas A&M Radiogenic Isotope Geosciences Facility for samples 17OR-03, 17OR-09, 17OR-10, and 17OR-18 following the LA-ICP-MS methods described for zircon U-Pb analyses in Section 3.3.1.2. The primary standard was Madagascar apatite, and the secondary standard was FC-1.

3.3.2 Basalt Samples

Basalt samples 17OR-04, 17OR-05, 17OR-07, 17OR-12, 17OR-19, and 17OR-20 were crushed with a small jaw-crusher and sieved to obtain <150, 150–250, 250–355, and 355–600 μm fractions. Groundmass concentrates were picked from the 150–250 and 250–355 μm fractions. To remove alteration effects, an acid leaching treatment was performed on the samples using a combination of HCl and HNO_3 at varying acid strengths (Koppers et al., 2000). The groundmass concentrates were irradiated for 6 hours (Irradiation 18-OSU-04) in the OSU TRIGA Reactor (CLICIT-position) nuclear reactor at Oregon State University. Fish Canyon Tuff (FCT-2-NM) sanidine flux monitor was irradiated with the samples, with a calibrated age of 28.201 ± 0.023 Ma 1σ after Kuiper et al. (2008).

3.3.2.1 Basalt Groundmass $^{40}Ar/^{39}Ar$ Analyses

The $^{40}Ar/^{39}Ar$ analyses were performed by incremental step-heating using the ARGUS-VI-E mass spectrometer at Oregon State University. The ARGUS-VI-E mass spectrometer has two Faraday collectors fitted with 10^{12} Ohm resistors on argon masses 41 and 40, three Faraday collectors fitted with 10^{13} Ohm resistors on argon masses 39, 38, and 37, and one ion-counting CuBe electron multiplier. The electron multiplier is located next to the lowest mass Faraday collector and allows all argon isotopes to be measured at the same time. This set-up allows the full multi-collector to run while measuring the lowest peak of mass 36 on the highly sensitive electron multiplier. The irradiated samples were loaded into a Cu-planchette using an ultra-high vacuum sample chamber and were then heated with a defocused 25 W CO_2 laser beam in a pattern across the sample that released the gas evenly. After heating was complete, the reactive gases were cleaned using an SAES Zr-Al ST101 getter at 400 °C for approximately 10 minutes along with two SAES Fe-V-Zr ST172 getters at 200 °C and room temperature. J-values were calculated by using parabolic extrapolation of the measured flux gradient against the irradiation height. The Steiger and Jager (1977) decay constant of 5.530 ± 0.097 x 10^{10} 1/yr (2σ) reported by Min et al. (2000) was used to calculate the $^{40}Ar/^{39}Ar$ ages, and all other constants used in the age calculations can be found in Table 2 of Koppers et al. (2003). Plateau ages and isochron ages were calculated using the ArArCALC v2.6.2 software developed by Koppers et al. (2000) (available at http://earthref.org/ArArCALC/).

3.4 HeFTy Inverse Thermal Modeling

HeFTy is a thermal modeling software that can forward model the expected data distribution for a given thermal history or inverse model apatite and zircon (U-Th)/He ages to produce potential thermal pathways (Ketcham, 2005). HeFTy uses a 'Frequentist' statistical method that assesses the goodness-of-fit between the input cooling ages and the predicted thermal pathways (Ketcham, 2005). This results in a built-in quality control mechanism that will not produce any models for geologically impossible scenarios, which is a major advantage of this program over other thermal modeling software. The downside is that HeFTy cannot model large, precise data sets and will not produce any pathways if the groups of grains modeled do not overlap within 1σ uncertainty.

User inputs include the range of the crystallization temperature and age, the present-day temperature, grain radius, [U] and [Th] ppm, grain age, and constraint boxes. One has the option of correcting for the alpha ejection in the input window, or directly inputting corrected He ages. The result is a time-temperature plot (Appendix Figures G.1–G.5). The "p-value", a statistical value that defines the probability that an observed value will be "at least as extreme" the least squares goodness of fit statistic under the Chi square distribution, defines whether a path is 'acceptable' (p-value cut-off of 0.05) or 'good' (p-value cut-off of 0.5) (Ketcham, 2005).

3.4.1 Model Parameters

Crystallization ages and temperature range were defined by zircon U-Pb dating and Ti-in-zircon thermometry, respectively, from these new and existing data (Utevsky, 2015). See Appendix Tables F.1–F.2 for specific model inputs. The present-day temperature was defined as 10 ± 5 °C. The redistribution alpha ejection method was selected, and the Ketcham et al. (2011) method was selected for the stopping distance for un-corrected (U-Th)/He ages and age alpha correction method.

The calibration settings selected were Flowers et al. (2009) RDAAM for apatite and Guenther et al. (2013) for zircon. All models were run under 'Best' precision.

Constraint boxes, which define where the thermal history must pass in time-temperature space, were defined by the closure temperatures for apatite (~40–80 °C) and zircon (~160–200 °C). For models that included both apatite and zircon data, the constraint box encompassed the range from 40–200 °C. The stratigraphic range of the constraint box was defined by the maximum depositional age within 2σ error and by the $^{40}Ar/^{39}Ar$ basalt age. The basalt constraint at Site I was modeled as 2.6 Ma, which was the minimum age of the ridge-capping basalt unit stratigraphic range. The basalt constraint at Site V was defined by sample 17OR-05.

3.4.2 Model Approach

Several considerations were taken into account when modeling the apatite and zircon (U-Th)/He data. First, some zircon and apatite ages were close to or older than the U-Pb age. Thus, zircon and apatite ages that were not within 2σ error uncertainty of the U-Pb age were excluded from modeling. Second, poor reproducibility of the data resulted in a spread of cooling ages. The approach was then to group grains with similar ages together and multiple potential combinations (Appendix Tables F.1–F.2). Third, multiple U-Pb ages were given by Utevsky (2015) at Site III. Both the older and younger U-Pb ages were modeled using the manner described above in Section 3.4.1.

3.4.3 Exhumation Rates

Exhumation rates were calculated from the HeFTy model results by using the minimum and maximum range in slopes of the period of rapid cooling (°C/Ma) at each site and dividing that value by an assumed geothermal gradient between 20–40 °C/km (Appendix Figures G.1–G.5). These rates only constrain the amount of rock uplift.

4. RESULTS

The following results combine existing data from Perez et al. (2017), Reiners et al. (2002, 2003), Verplanck (1985), and Utevsky (2015) with new data. Perez et al. (2017) samples consist of apatite and zircon grains from Utevsky (2015) separates. Figure 4.1 shows time-temperature paths for each sample site from pluton crystallization to basalt emplacement, and Figure 4.2 shows a map view compilation of the raw data. All (U-Th)/He ages reported are corrected for alpha ejection and error uncertainties as 2σ unless otherwise noted.

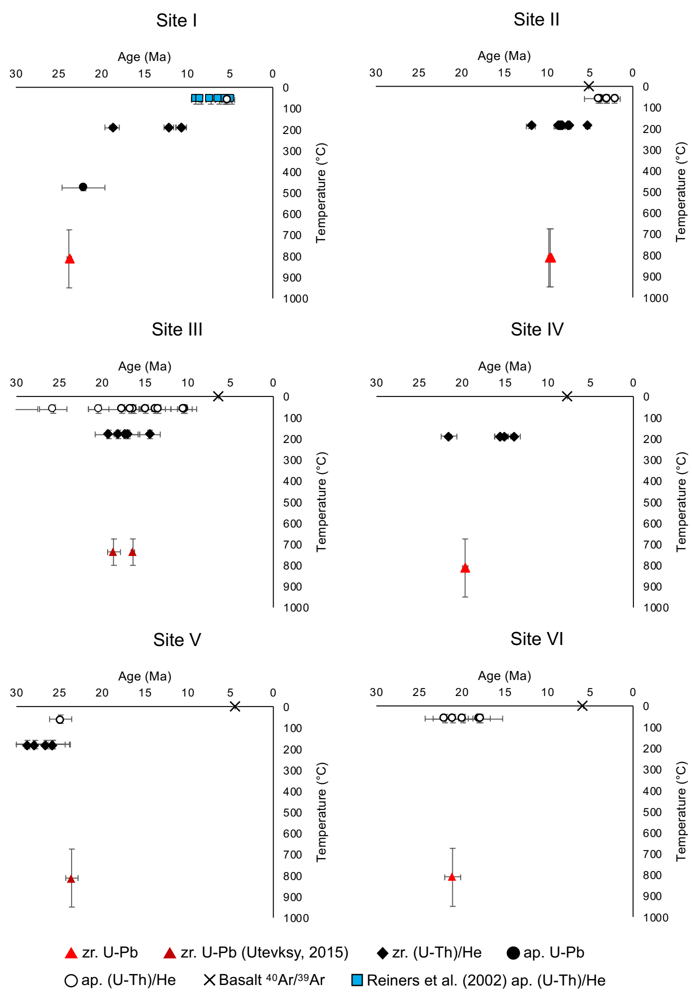

Figure 4.1: Time-temperature plots for each sample site location. Age error bars are reported in 2σ, and temperature error bars encompass approximate closure temperature for each system.

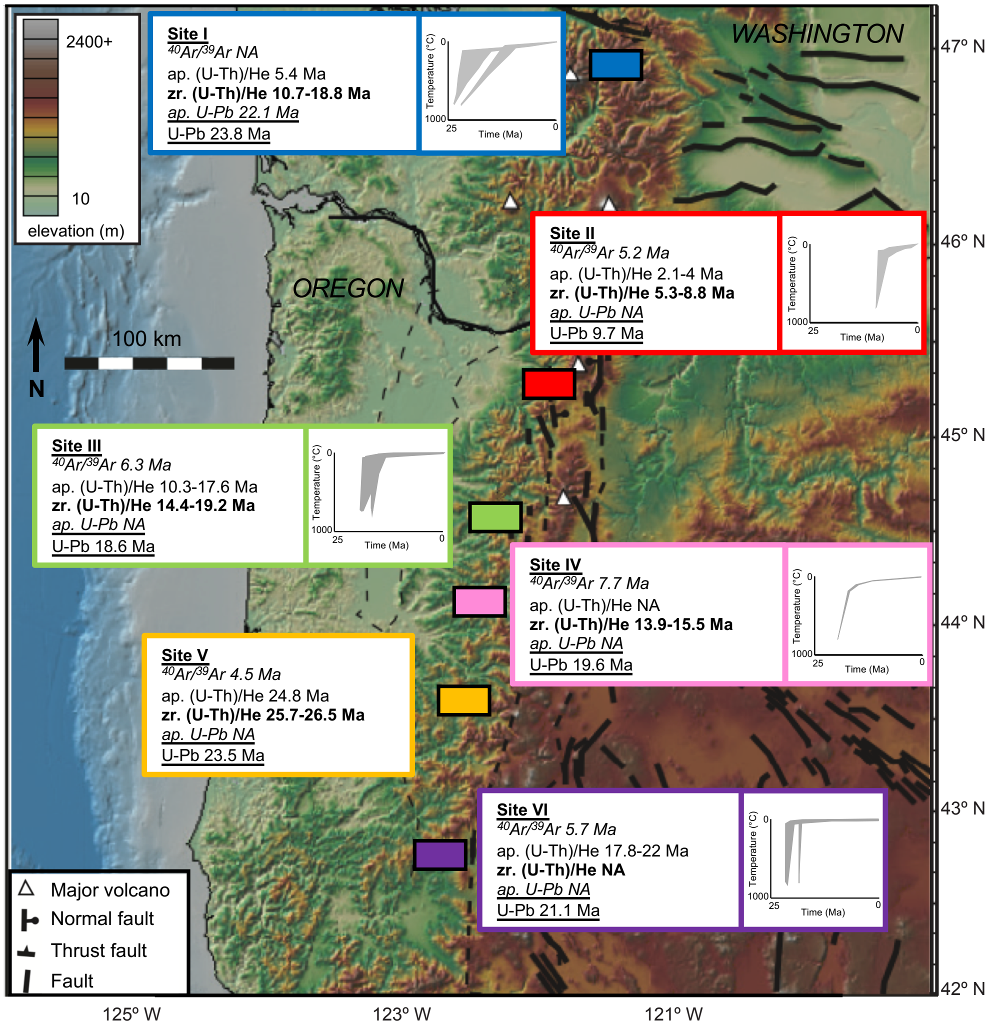

Figure 4.2: Map of study region with geochronology and thermochronology ages for each site. Apatite and zircon (U-Th)/He ages reported are corrected for alpha ejection. HeFTy plots are shown in the right panel for each site and display the range of weighted mean paths from various models. Site V did not produce any acceptable or good HeFTy model paths.

4.1 Site I

The zircon U-Pb age for sample 17OR-18 at Site I in southern Washington is 23.76 ± 0.26 Ma. The apatite U-Pb age for sample 17OR-18 is 22.10 ± 2.50 Ma. Zircon (U-Th)/He ages range from 10.68 ± 0.60 to 18.76 ± 0.84 Ma. Apatite (U-Th)/He ages are 5.40 ± 0.19 and 5.40 ± 0.54 Ma. The groundmass total fusion age of basalt sample 17OR-19 is 27.68 ± 0.05 Ma, which is significantly older than the apatite and zircon (U-Th)/He ages and the other ridge-capping basalts. This age suggests the pluton likely intruded into this unit, and therefore the minimum age of the stratigraphic range of the ridge-capping basalt unit was used to constrain the HeFTy model (Appendix Table F.1). The range of the weighted mean HeFTy model paths of all potential groupings at each site were considered as viable cooling histories (Figure 4.3). The model results for Site I, which include apatite (U-Th)/He ages from Reiners et al. (2002), show rapid cooling occurring between ~10–24 Ma. The calculated exhumation rate is between 3–16 km/Ma and 2–8 km/Ma assuming geothermal gradients of 20 °C/km and 40 °C/km, respectively (Appendix Figure G.1).

4.2 Site II

The zircon U-Pb ages for samples 17OR-10 and 17OR-11 at Site II in northern Oregon are 9.72 ± 0.18 and 9.56 ± 0.08 Ma, respectively. Zircon (U-Th)/He ages for samples 17OR-10 and 17OR-11 range from 7.52 ± 0.34 to 8.66 ± 0.38 Ma and 5.26 ± 0.24 to 11.91 ± 0.52 Ma, respectively. Apatite (U-Th)/He ages for sample 17OR-10 range from 2.13 ± 0.67 to 4.00 ± 1.63 Ma. The groundmass total fusion age of basalt sample 17OR-12 is 5.15 ± 0.01 Ma. The model results for Site II show rapid cooling occurring between ~7–9 Ma (Figure 4.3). The calculated exhumation rate is between 11–66 km/Ma and 5–33 km/Ma assuming geothermal gradients of 20 °C/km and 40 °C/km, respectively (Appendix Figure G.2).

4.3 Site III

The zircon U-Pb age of sample WCOS-2 at Site III in northern-central Oregon is 18.6 ± 0.75 Ma, acquired by LA-ICP-MS methods (Utevsky, 2015). The same sample dated by SHRIMP-RG yields a zircon U-Pb age of 16.4 ± 0.2 Ma (Utevsky, 2015). Zircon (U-Th)/He ages from sample WCOS-2 range from 14.4 ± 1.2 to 19.2 ± 1.6 Ma (Perez et al., 2017). Apatite (U-Th)/He ages from samples WCOS-2 and 17OR-09 range from 13.4 ± 0.8 to 31.1 ± 3.6 Ma (Perez et al., 2017) and 10.33 ± 0.86 to 17.64 ± 3.93 Ma, respectively. An existing K-Ar age of a ridge-capping basalt at this location is 6.30 ± 0.10 Ma (Verplanck, 1985). The HeFTy model results show rapid cooling occurring between ~13–19 Ma (Figure 4.3). The calculated exhumation rate is between 6–66 km/Ma and 3–33 km/Ma assuming geothermal gradients of 20 °C/km and 40 °C/km, respectively (Appendix Figure G.3).

4.4 Site IV

The zircon U-Pb age of sample 17OR-06 in central Oregon is 19.63 ± 0.31 Ma. Zircon (U-Th)/He ages range from 13.90 ± 0.70 to 21.52 ± 0.92 Ma. Sample 17OR-06 did not yield any apatite grains. The groundmass total fusion age of basalt sample 17OR-07 is 7.70 ± 0.02 Ma. The HeFTy model results show rapid cooling occurring between ~15–20 Ma (Figure 4.3). The calculated exhumation rate is between 11–14 km/Ma and 6–7 km/Ma assuming geothermal gradients of 20 °C/km and 40 °C/km, respectively (Appendix Figure G.4).

4.5 Site V

The zircon U-Pb age of sample WCOSNU-25 in central-southern Oregon is 23.52 ± 0.72 Ma (Utevsky, 2015). Zircon (U-Th)/He ages range from 25.7 ± 2.0 to 31.1 ± 2.4 Ma (Perez et al., 2017). The apatite (U-Th)/He age from sample 17OR-03 is 24.83 ± 1.29 Ma. The groundmass mini-plateau ages of basalt samples 17OR-04 and 17OR-05 are 11.41 ± 0.07 and 4.46 ± 0.02 Ma, respectively. These apatite and zircon (U-Th)/He ages are all older than the U-Pb age from Utevsky (2015). The (U-Th)/He ages that overlapped within 2σ were modeled, but no acceptable or good paths were produced. Thus, the exhumation rate could not be calculated at this site.

4.6 Site VI

Samples WCOSNU-11 and 17OR-02 in southern Oregon are from two separate plutons of different lithologies located approximately 19 km apart. The zircon U-Pb age of sample WCOSNU-11 is 18.15 ± 0.43 Ma (Utevsky, 2015), and the zircon U-Pb age of sample 17OR-02 is 21.08 ± 0.93 Ma. Apatite (U-Th)/He ages from sample WCOSNU-11 range from 18.0 ± 1.2 to 27.3 ± 1.6 Ma (Perez et al., 2017), and apatite (U-Th)/He ages from sample 17OR-02 range from 17.81 ± 2.57 to 21.96 ± 2.34 Ma. The groundmass total fusion age of basalt sample 17OR-20 is 5.77 ± 0.01 Ma. Both samples were modeled independently, and the HeFTy model results show rapid cooling occurring between ~17–22 Ma at this location (Figure 4.3). The calculated exhumation rate is between 28–91 km/Ma and 14–45 km/Ma assuming geothermal gradients of 20 °C/km and 40 °C/km, respectively (Appendix Figure G.5).

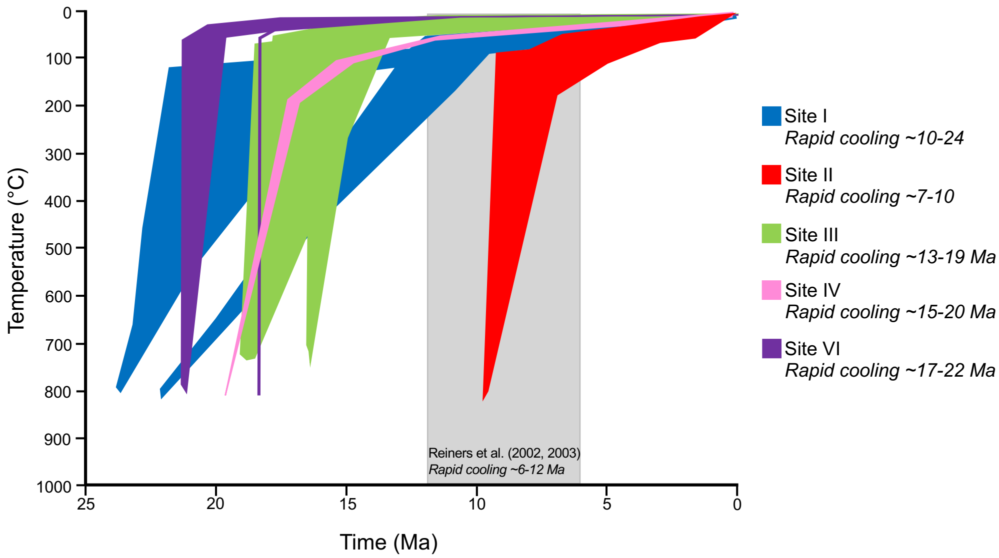

Figure 4.3: Envelopes of all HeFTy weighted mean paths for each site location. Gray box indicates ~6–12 Ma timing of exhumation reported by Reiners et al. (2002, 2003) in the Washington Cascades. The timing of exhumation generally increases from Site I in southern Washington to Site VI in southern Oregon, with Site II in northern Oregon displaying the youngest cooling ages.

4.7 Effective Uranium Concentration

The [eU] of apatite grains from sample 17OR-18 at Site I in southern Washington range from 9.7–42.4 ppm. The [eU] of apatite grains from sample 17OR-10 at Site II in northern Oregon range from 1.3–9.2 ppm. The [eU] of apatite grains from samples 17OR-09 and WCOS-2 at Site III in northern-central Oregon range from 2.8–5.9 ppm and 6.6–43.3 ppm, respectively. The [eU] of zircon grains from sample WCOS-2 range from 251.1–547.6 ppm. The [eU] of zircon grains from sample 17OR-06 at Site IV in central Oregon range from 65.9–279.7 ppm. The [eU] of the apatite grain from sample 17OR-03 at Site V in central-southern Oregon is 16.3 ppm. The [eU] of zircon grains from sample WCOSNU-25 at Site V range from 83.3–251.3 ppm. The [eU] of apatite grains from samples 17OR-02 and WCOSNU-11 at Site VI in southern Oregon range from 2.6–3.8 ppm and 24.8–38.6 ppm, respectively. Figure 4.4 and Figure 4.5 show [eU] from all samples at each site plotted against the respective apatite or zircon (U-Th)/He age. There are no clear trends in the data that link anomalously old apatite and zircon (U-Th)/He ages with [eU].

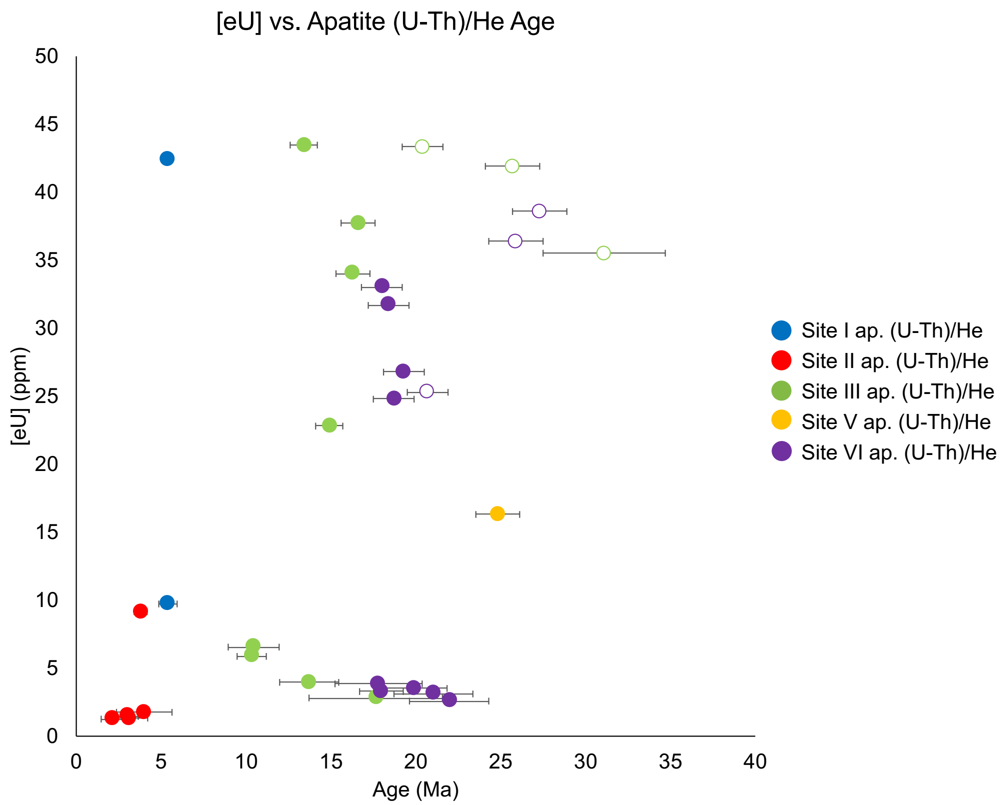

Figure 4.4: [eU] of samples from each site plotted against apatite (U-Th)/He age, where hollow markers indicate apatite (U-Th)/He ages that are older than the zircon U-Pb age. Error bars are reported in 2σ.

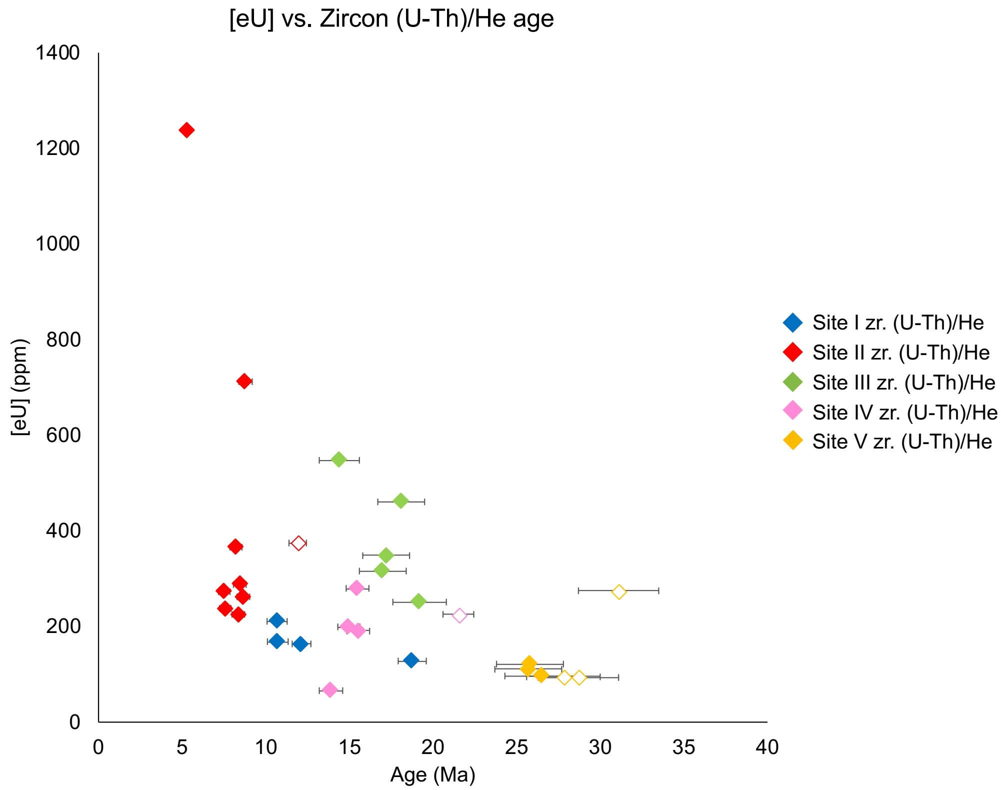

Figure 4.5: [eU] of samples from each site plotted against zircon (U-Th)/He age, where hollow markers indicate zircon (U-Th)/He ages that are older than the zircon U-Pb age. Error bars are reported in 2σ.

4.8 Equivalent Sphere Radius

The equivalent sphere radius (ESR) values of apatite and zircon grains from sample 17OR-18 at Site I in southern Washington range from 60.9–71.7 μm and 36.5–51.5 μm, respectively. The ESR values of apatite and zircon grains from sample 17OR-10 at Site II in northern Oregon range from 55.2–80.9 μm and 50.2–68.8 μm, respectively. The ESR values of zircon grains from sample 17OR-11 at Site II range from 45.5–75.2 μm. The ESR values of apatite grains from samples 17OR-09 and WCOS-2 at Site III in northern-central Oregon range from 44.4–53.1 μm and 32.4–53.2 μm, respectively. The ESR values of zircon grains from sample WCOS-2 range from 38.8–52.6 μm. The ESR values of zircon grains from sample 17OR-06 at Site IV in central Oregon range from 46.5–51.7 μm. The ESR value of the apatite grain from sample 17OR-03 at Site V in central-southern Oregon is 53.0 μm. The ESR values of zircon grains from sample WCOSNU-25 at Site V range from 36.2–48.5 μm. The ESR values of apatite grains from samples 17OR-02 and WCOSNU-11 at Site VI in southern Oregon range from 42.5–69.1 μm and 37.7–54.0 μm, respectively. Figure 4.6 and Figure 4.7 show ESR values from all samples at each site plotted against the respective apatite or zircon (U-Th)/He age. Some of the anomalously old apatite and zircon (U-Th)/He ages correspond to smaller grain size, but this trend is not consistent across all sites.

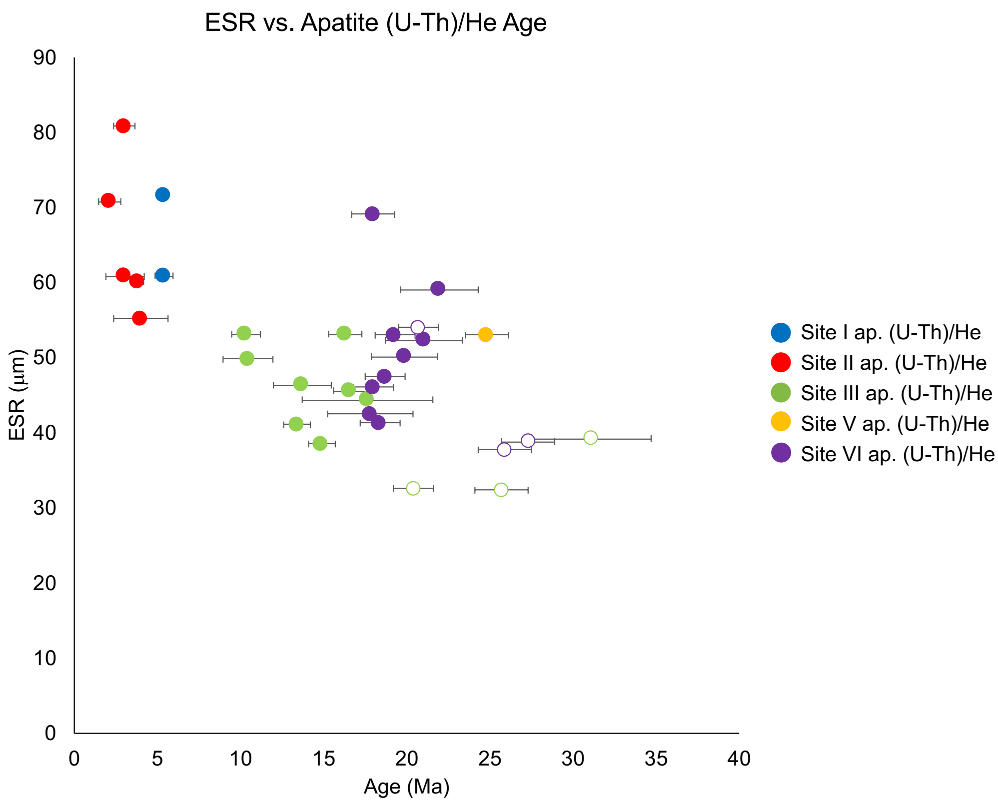

Figure 4.6: ESR concentrations of all samples from each site plotted against apatite (U-Th)/He age, where hollow markers indicate apatite (U-Th)/He ages that are older than the zircon U-Pb age. Error bars are reported in 2σ.

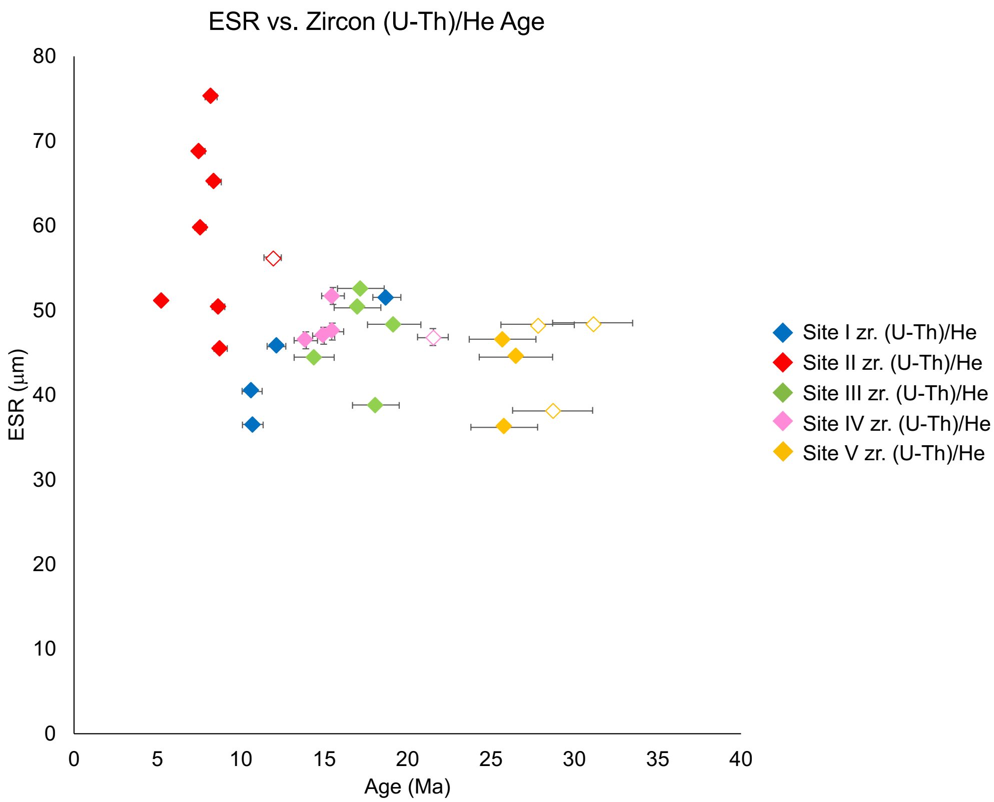

Figure 4.7: ESR concentrations of all samples from each site plotted against zircon (U-Th)/He age, where hollow markers indicate zircon (U-Th)/He ages that are older than the zircon U-Pb age. Error bars are reported in 2σ.

5. DISCUSSION

5.1 Recording Magmatic Cooling vs. Exhumation Signal

The majority of the cooling models generated from this study support early rapid cooling of the plutons immediately after crystallization followed by relatively slow and low-magnitude cooling. One potential interpretation of such results is that the thermochronologic data are recording cooling associated with pluton crystallization and not exhumation related to rock uplift. We contend, based on two arguments, that most of the apatite and zircon (U-Th)/He ages in this study record the exhumation signal, with the exception of apatite (U-Th)/He ages at Site II and the results at Site V. First, the difference between the apatite and zircon (U-Th)/He ages and the zircon U-Pb is on the scale of millions of years. Models suggest magmatic cooling occurs on a timescale of thousands of years (Nabelek et al., 2012). If these data were recording magmatic cooling, then one would expect the apatite and zircon (U-Th)/He ages to be nearly the same as the zircon U-Pb age. These new data however show a range of cooling ages that are mostly millions of years younger than the crystallization age. At Site III for example, apatite (U-Th)/He ages are between one and eight million years younger than the older zircon U-Pb age reported by Utevsky (2015), excluding those that are anomalously older than the zircon U-Pb age.

The data from Site II in northern Oregon are unusual in that the apatite (U-Th)/He ages are younger than the basalt emplacement age. These data were modeled using the same constraints described in Section 3.4, but more acceptable and good paths were produced when a reheating constraint was added during the timing of the basalt emplacement (Appendix Table F.1). The constraint box spanned from 40–100 °C so the model had the option of reheating or not reheating. The zircon (U-Th)/He ages are older than the basalt emplacement age, which suggests these ages were not reset and represent the exhumation signal. At Site V in central-southern Oregon, the anomalously old apatite and zircon (U-Th)/He ages produced no acceptable or good cooling paths from the HeFTy models.

Second, the apatite and zircon (U-Th)/He cooling ages are out-of-phase with the zircon U-Pb crystallization ages. If the cooling ages were reflecting magmatic cooling, one would expect consistency between the offset of the apatite and zircon (U-Th)/He ages and the zircon U-Pb age across the six sample sites. This trend is not seen in the data however. For example, at Site III the apatite (U-Th)/He ages differ from the zircon U-Pb age by ~1–8 Ma. At Site VI, this difference is about ~3 Ma. Additionally, there does not appear to be systematic trend in the zircon (U-Th)/He ages relative to the U-Pb ages or the apatite (U-Th)/He ages. These observations highlight the value of using multiple geo- and thermochronometers on the same sample at various sites as these relationships may not be apparent otherwise.

5.1.1 Anomalously Old Apatite and Zircon (U-Th)/He Ages

Anomalously old apatite and zircon (U-Th)/He cooling ages are observed in the data that are not believed to record the exhumation signal. This issue occurs particularly at Sites III, V, and VI in central to southern Oregon where some apatite and zircon (U-Th)/He ages are older than the zircon U-Pb crystallization, including some ages given by Utevsky (2015). Zircons from Utevsky (2015) sample separates were re-dated in this study, and our new U-Pb ages confirm those reported by Utevsky (2015) (Appendix Figures B.1 – B.4). Grain size and radiation damage are known to affect helium diffusivity (Flowers et al., 2009; Gautheron et al., 2009; Hansen and Reiners, 2006; Reiners and Farley, 2001; Shuster et al., 2006), but the expected positive slope relationship between age and [eU] characteristic of radiation damage accumulation and annealing effects is observed in only some of the data (Appendix Figures D.1–D.2). A weak negative correlation between ESR and grain size is observed (Figure 4.6–4.7), perhaps due to inaccuracies in the F_t correction as more area of the grain would be susceptible to the alpha ejection effect. Other potential explanations for the anomalously old (U-Th)/He ages include inclusions, zoning, or ^{4}He implantation from a "bad neighbor" scenario or U-Th-rich grain boundary phases.

U-Th-rich mineral inclusions, such as zircon, titanite, or monazite, could be a potential explanation for the unusually old (U-Th)/He ages. Mineral inclusions that are not dissolved during the dissolution process could result in "parentless" ^{4}He, as the Sm-Th-U concentrations are measured only from the grain. Many of the apatite crystals from the samples in this study contained small inclusions, so it could be possible that the results were affected by this issue (Figure 3.4). Zoning could be another reason for the old (U-Th)/He ages, as the alpha ejection correction assumes an equal distribution of U and Th in the crystal. This effect could result in either younger or older ages and is more common in zircon grains as opposed to apatite (Ault and Flowers, 2012; Farley et al., 2011; Gautheron et al., 2012; Johnstone et al., 2013).

He implantation is another possible explanation for the old apatite (U-Th)/He ages. The alpha ejection effect could result in the implantation of excess ^{4}He ejected from U-Th rich minerals into neighboring grains with lower [U] and [Th] (<5 ppm) (Spiegel et al., 2009). This scenario would also result in "parentless" ^{4}He. Some have attributed anomalously old apatite (U-Th)/He ages to implantation from U-Th-rich grain boundary phases (GBPs) that appear as a precipitate on the crystal surface (Murray et al., 2014). These authors found apatite grains from an igneous bedrock sample that were heavily coated with a thin (1–10 μm) red-orange precipitate and other grains from the same sample that had no apparent coating. These coatings were found to be enriched in Fe, and potentially Al, K, Ca, Mn, Mg, U, and Th, with an [eU] of 2–10 times more than the grain itself (Murray et al., 2014). A thick GBP coat (~3 mm) was found to have an [eU] of 90 ppm (Murray et al., 2014). Additionally, these authors note the GBP precipitates are likely to fall off during the mineral separation process, so one may not even be aware of their presence and effect until after lab analyses. The timing of GBP is particularly important in how the apatite (U-Th)/He age is affected. If GBPs form before or near to the time of cooling and are then lost prior to analyses, during the mineral separation process for example, the resulting age can be skewed older than it should be due to the implantation of excess ^{4}He (Murray et al., 2014). If GBPs form well after the grain has cooled, there may be no effect or the age may be too young if the GBP is analyzed along with the grain (Murray et al., 2014). The effect of GBPs on apatite helium ages is a complex problem, as the timing of GBP formation, the implantation effect, diffusion properties, coverage (distribution and thickness), and composition are variable (Murray et al., 2014). A possible solution is to use apatite fission track thermochronometry in conjunction with apatite (U-Th)/He dating as this method allows regions of the crystal with unusually high track densities to be excluded from counting (Murray et al., 2014).

No coatings were observed on the apatite grains of samples from this study, although it is possible they were removed during the mineral separation process. These grains did however have low [U] and [Th], many of which were <5 ppm (Appendix Table A.1). If U-Th rich GBPs were present on the grains and removed during the mineral separation process, the effect may still be present in the resulting data. He implantation could have occurred in the zircon grains as well, but the effect may not be as significant considering the higher [eU], which are above 100 ppm in most of the grains (Appendix Table A.2).

5.1.2 Incorporating Effects of Radiation Damage and He Implantation

A negative slope on an age vs [eU] plot can be indicative of apatite grains affected by a "bad neighbor" scenario involving ^{4}He implantation from U-Th-rich GBPs (Murray et al., 2014). If this is the case, the grains with the highest [eU] (i.e. the youngest ages) are closest to the true age and represent the maximum cooling age of the sample (Murray et al., 2014). A negative-slope-age-[eU] pattern is observed with the apatite (U-Th)/He data at Sites III and VI (Figure 5.1). Only the apatite grains with the highest [eU] were selected for HeFTy modeling to exclude those potentially affected by He implantation (Figure 5.2). A positive-slope-age-[eU] pattern can be indicative of radiation damage to the crystal, and He implantation and radiation damage effects can be present in the same sample (Murray et al., 2014). The RDAAM model developed by Flowers et al. (2009) can correct for radiation damage effects in HeFTy modeling.

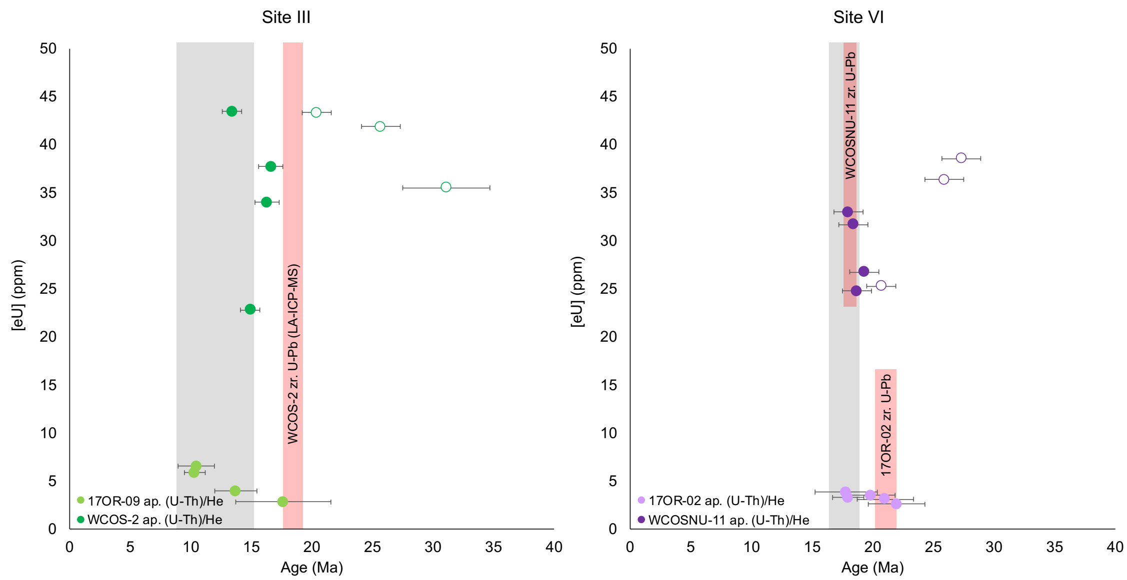

Figure 5.1: [eU] of samples from selected sites plotted against age that display a negative-slope-age-[eU] relationship. Hollow markers indicate apatite (U-Th)/He ages that are older than the zircon U-Pb age. Gray boxes indicate the (U-Th)/He ages with higher [eU], which are closest to the true maximum cooling age and used in preferred HeFTy models. Red boxes indicate the zircon U-Pb crystallization age given by Utevsky (2015) for samples WCOS-2 and WCOSNU-11 or obtained from this study for sample 17OR-02. Error bars are reported in 2σ.

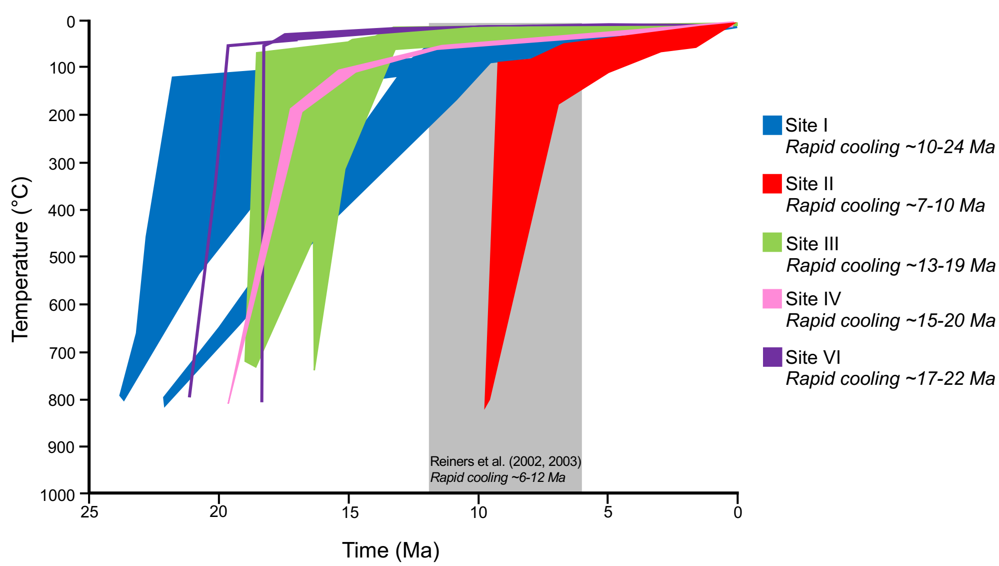

Figure 5.2: Preferred envelopes of HeFTy weighted mean paths using youngest apatite (U-Th)/He ages at Sites III and VI. The timing of rapid cooling at each site does not change significantly from envelopes of HeFTy weighted mean paths using all apatite grains.

5.2 North-South Trends in Exhumation Timing

The zircon U-Pb ages demonstrate that the plutons crystallized during the early to mid-Miocene and lack a systematic progression of ages from north to south. The zircon (U-Th)/He trend is variable along-strike, but the ages generally increase from north to south with Site II in northern Oregon having the youngest ages. The apatite (U-Th)/He ages also generally increase from north to south, with Site II having the youngest ages, although this location was likely affected by partial resetting during basalt emplacement. These generalized trends tentatively suggest that exhumation timing is broadly older in the south and becomes younger northward. The basalt $^{40}Ar/^{39}Ar$ ages suggest basalt emplacement occurred during the Late Miocene to early Pliocene, but no spatial pattern is discerned.

Reiners et al. (2002, 2003) found the timing of exhumation along the western flank of the Washington Cascades to be ~6–12 Ma based on apatite fission track and (U-Th)/He ages. The apatite (U-Th)/He ages in Washington from this study are consistent with these findings. With the exception of Site II in northern Oregon, the apatite (U-Th)/He ages from this study in Oregon are generally older than the ~6–12 Ma range in Washington (Reiners et al., 2002, 2003) and range from ~10–25 Ma (Figure 4.2). The apatite (U-Th)/He ages at Site II range from ~2–4 Ma and are younger than the ~6–12 Ma range given by Reiners et al. (2002, 2003). However, we attribute these ~2–4 Ma ages to resetting by basalt emplacement, which do not reflect exhumational cooling. HeFTy modeling that included apatite and/or zircon (U-Th)/He ages show the timing of exhumation ranging from ~13–19 Ma in central Oregon and ~17–22 Ma in southern Oregon. Thus, the results from this study support an early to mid-Miocene exhumation that occurred mostly before the timing of exhumation constrained in Washington.

5.3 Comparison with Previous Findings

5.3.1 Analytical Methods

At Site I in southern Washington, pluton sample 17OR-18 was collected at the same site as samples 00193 and 00193b from Reiners et al. (2002, 2003) to compare the analytical results. The apatite (U-Th)/He ages from sample 17OR-18 are 5.40 ± 0.19 and 5.40 ± 0.54 Ma. The apatite (U-Th)/He ages from sample 00193 and 00193b (Reiners et al., 2002, 2003) are 8.96 ± 0.54 and 8.42 ± 0.51 Ma, respectively. The difference between the ages could be a result of the analytical method used. The single crystal (U-Th)/He method was used in this study, whereas the Reiners et al. (2002, 2003) samples used both single and multi-crystal aliquots. Samples 00193 and 00193b (Reiners et al., 2002, 2003) used multi-crystal analyses. Multi-crystal aggregates were used in early (U-Th)/He dating to ensure $^4He/^3He$ could be measured above the blank level (Farley et al., 2010). More recent findings have shown that even small differences in each crystal's diffusivity can result in inaccurate $^4He/^3He$ spectrum and incorrect assumptions of Arrhenius parameters when multi-crystal aggregates are analyzed together (Farley et al., 2010). This could explain the ~3 Ma discrepancy between the age results of this study and previous work by Reiners et al. (2002, 2003).

5.3.2 Exhumation and Erosion Rates

The apparent exhumation rate of samples from the western flank of the Washington Cascades was found to be 0.5–1.0 km/m.y. from ~6–12 Ma based on an age-elevation transect (Reiners et al., 2002). An age-elevation transect was not performed in this study given that the sample locations in the Oregon Cascades lacked sufficient topographic relief. As an alternative, exhumation rates were calculated using the relationship among the multiple geo- and thermochronometers (see Section 3.4.3). The calculated exhumation rates from this study, which range from 3–16 to 28–91 km/Ma and 2–8 to 14–45 assuming geothermal gradients of 20 °C/km and 40 °C/km respectively, are higher than those found by Reiners et al. (2002), but the results show the rate of exhumation increases from north to south along the range. This study does not provide a direct comparison to the erosion rates calculated by Reiners et al. (2003).

5.4 Role of Climate and Tectonics in Driving Rock Uplift

The contribution of climate and tectonics in driving rock uplift can be evaluated by comparing the apatite and zircon (U-Th)/He cooling ages to spatial trends in precipitation and deformation over time. Cooling ages from previous findings by Reiners et al. (2002, 2003) range from ~6–12 Ma in Washington and are younger than the ∼17 Ma onset of Yakima Fold Belt compression (Figure 5.3) (Blakely et al., 2011). Those ages were attributed to exhumation guided by climatic patterns that focused increased precipitation and erosion along the western Cascade flank and supported by the lack of a relationship between the cooling ages and mapped structural features (Reiners et al., 2002, 2003). However, the possibility that these ages are driven by deeper structures with no surface expression still exists, as Yakima Fold Belt shortening has been active throughout the interval that Washington exhumation is observed (Kelsey et al., 2017; Staisch et al., 2017, 2018) and western Washington is seismically active (Wells et al., 2002).

The new cooling ages from this study in Oregon are older than the ∼12 Ma onset of Basin and Range extension and were collected from regions that are situated north of the northernmost Basin and Range deformation (Figure 5.3) (Colgan et al., 2004; Dilles and Gans, 1995; Surpless et al., 2002; Trench et al., 2012). These ages could represent monotonic cooling that is indistinguishable from emplacement, or alternatively these results may reflect apatite and zircon grains that remained in the partial retention zone for an extended amount of time during lateral movement associated with the vertical axis rotation experienced by the Oregon block. In a compressional tectonic regime, such as the Yakima Fold Belt, the three-dimensional trajectory of the plutons during exhumation would contain a larger component of vertical motion as opposed to lateral motion. In contrast, the three-dimensional movement of plutons during exhumation in an extensional tectonic regime, such as the Basin and Range province, could contain a large component of lateral motion in addition to vertical motion. Apatite and zircon grains located within the partial retention zone for an extended amount of time would have altered diffusion kinetics, which may contribute to the dispersion observed among the (U-Th)/He ages.

All cooling ages, including from previous work (Reiners et al., 2002, 2003) and this study, are younger than the ∼27 Ma development of the Cascades rain shadow (Figure 5.3) (Kohn et al., 2002). However, the onset of the Cascades rain shadow could have varied along-strike as paleoclimate studies are specific to the sample region. Previous work attributed exhumation in the Coast

Mountains of Alaska and the Washington Cascades as climate-driven due to the similarity in exhumation timing and the same precipitation trend (Reiners et al., 2002, 2003), but these new data show the timing of exhumation in the Oregon Cascades is not consistent with these previous findings. The difference in the timing of exhumation, in addition to previous work that suggests surface processes alone cannot account for the total amount of rock uplift in central Oregon (Lopez and Meigs, 2016), open the possibility for an additional component of tectonic- or magmatic-driven exhumation in the Oregon and Washington Cascades. Although the precise contribution from various surface and tectonic mechanisms remains poorly constrained, our data supports the concept that the interactions among these processes are active in driving exhumation in the Cascades.

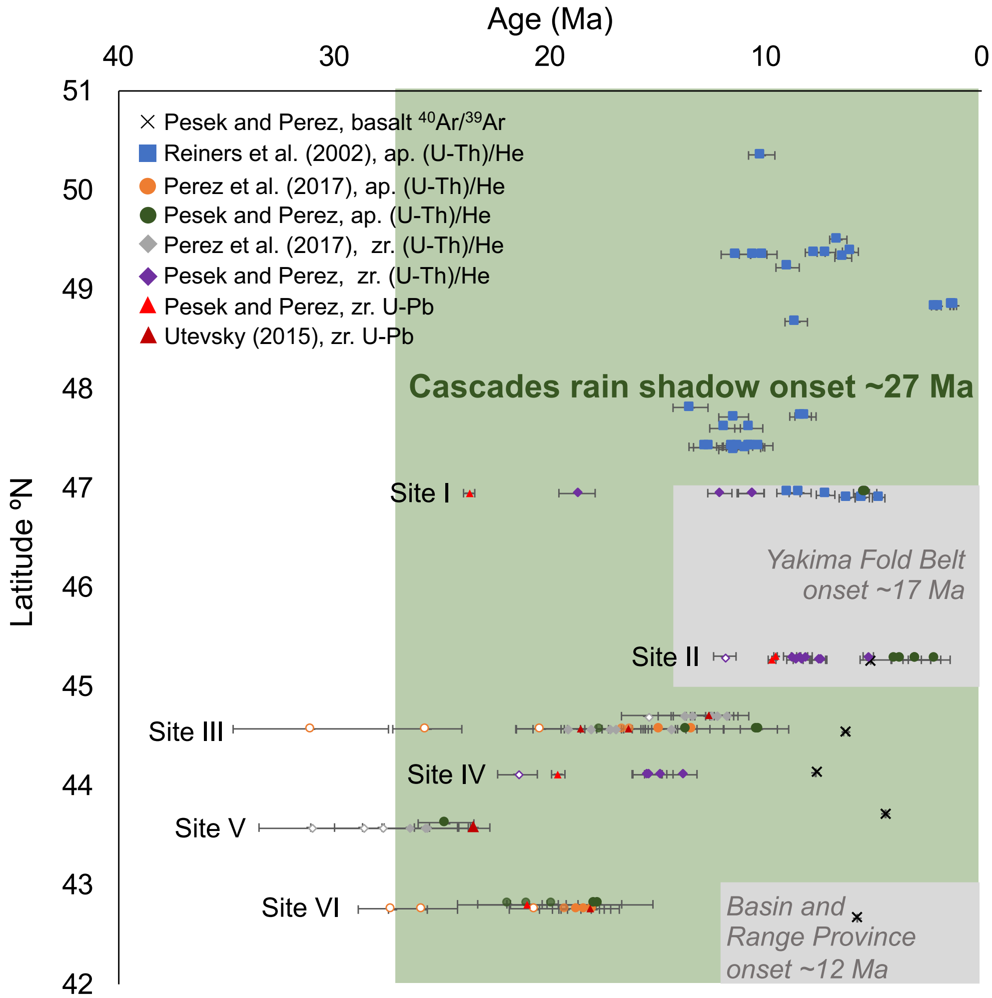

Figure 5.3: All geochronology and thermochronology for each site plotted against latitude. Green box is the geographical extent and oldest onset of Cascades rain shadow (Kohn et al., 2002), and gray boxes show geographical extent and timing of tectonic events (Blakely et al., 2011; Colgan et al., 2004; Dilles and Gans, 1995; Surpless et al., 2002; Trench et al., 2012). White markers indicate apatite and zircon (U-Th)/He ages that are older than the zircon U-Pb age. Error bars are reported in 2σ.

6. CONCLUSIONS

Determining the contributions of climate and tectonics to rock uplift is a challenging task, yet fundamental to understand Earth systems. The Oregon and Washington Cascades provide an ideal setting to evaluate the feedbacks among climate, erosion, and tectonics due to the unique along-strike trends in deformation, magmatic activity, and precipitation. This study used multiple geo- and thermochronometers, including zircon U-Pb, apatite and zircon (U-Th)/He, and basalt groundmass $^{40}Ar/^{39}Ar$ dating, to define the timing and pace of exhumation in Oregon and southern Washington. The timing of exhumation ranged from ~7–22 Ma in Oregon, where most plutons cooled early and rapidly over the course of ~3–6 Ma, followed by slower, gradual cooling over the next ~7–17 Ma.

These data support the timing of exhumation occurred earlier in Oregon than the ~6–12 Ma timing in Washington found by previous studies (Reiners et al., 2002). The timing of exhumation generally increases from north to south, although the location near Mount Hood in northern Oregon displays the youngest crystallization and (U-Th)/He ages. This general southward increase in exhumation timing is inconsistent with synchronous exhumation predicted by regionally consistent surface processes drivers. Instead, north to south variations in the timing, style, and magnitude of tectonics and magmatic activity likely have a significant impact on the diachronous exhumation timing in this region. These results support tectonic and/or magmatic processes as important drivers to exhumation in the Oregon and Washington Cascades, and highlight the role of interactions among climate, erosion, and tectonics processes on orogen development.

REFERENCES

Andersen, T. (2002). Correction of common lead in U – Pb analyses that do not report 204 Pb. *Chemical Geology*, 192(1–2):59–79.

Ault, A. and Flowers, R. (2012). Is apatite U–Th zonation information necessary for accurate interpretation of apatite (U–Th)/He thermochronometry data? *Geochimica et Cosmochimica Acta*, 79:60–78.

Blakely, R. J., Sherrod, B. L., Weaver, C. S., Wells, R. E., Rohay, A. C., Barnett, E. A., and Knepprath, N. E. (2011). Connecting the Yakima fold and thrust belt to active faults in the Puget Lowland, Washington. *Journal of Geophysical Research: Solid Earth*, 116(7):1–34.

Boyce, J. W., Hodges, K. V., Olszewski, W. J., Jercinovic, M. J., Carpenter, B. D., and Reiners, P. W. (2006). Laser microprobe (U-Th)/He geochronology. *Geochimica et Cosmochimica Acta*, 70(12):3031–3039.

Burbank, D. W., Blythe, A. E., Putkonen, J. L., Pratt-Situala, B. A., Gabet, E. J., Oskin, M. E., Barros, A. P., and Ohja, T. P. (2003). Decoupling of erosion and climate in the Himalaya. *Nature*, 426:652–655.

Chamberlain, K. and Bowring, S. (2002). Apatite–feldspar U–Pb thermochronometer: a reliable mid-range (~450 °C), diffusion controlled system. *Chemical Geology*, 172:173–200.

Chew, D., Sylvester, P., and Tubrett, M. (2011). U-Pb and Th-Pb dating of apatite by LA-ICPMS. *Chemical Geology*, 280:200–216.

Christiansen, R. and Yeats, R. (1992). Post-Laramide geology of the U.S. Cordilleran region. In Burchfiel, B., Lipman, P., and Zoback, M., editors, *The Cordilleran orogen: Conterminous U.S.*, pages 261–406. Boulder, CO: Geological Society of America, Geology of North America, G-3 edition.

Colgan, J., Dumitru, T., and Miller, E. (2004). Diachroneity of Basin and Range extension and Yellowstone hotspot volcanism in northwestern Nevada. *Geological Society of America Bulletin*, 32:121–124.

Conrey, R. M., Taylor, E. M., Donnelly-Nolan, J. M., and Sherrod, D. R. (2002). North-Central Oregon Cascades: Exploring Petrologic and Tectonic Intimacy in a Propagating Intra-Arc Rift. *Field Guide to Geologic Processes in Cascadia: Oregon Department of Geology and Mineral Industries*, 36:47–90.

Degeling, H. (2003). *Zr equilibria in metamorphic rocks*. Unpublished PhD thesis, Australian National University.

Dilles, J. and Gans, P. (1995). The chronology of Cenozoic volcanism and deformation in the Yerington area, western Basin and Range and Walker Lane. *Geological Society of America Bulletin*, 197:474–486.

Dilles, J. H. (1987). Petrology of the Yerington Batholith, Nevada: Evidence for evolution of porphyry copper ore fluids. *Economic Geology*, 82(7):1750–1789.

Dodson, M. (1973). Closure temperature in cooling geochronological and petrological systems. *Contributions to Mineralogy and Petrology*, 40:259–274.

du Bray, E. and John, D. (2011). Petrologic, tectonic, and metallogenic evolution of the Ancestral Cascades magmatic arc, Washington, Oregon, and northern California. *Geosphere*, 7(5):1102–1133.

Duncan, R. and Kulm, L. (1989). Plate tectonic evolution of the Cascades arc-subduction complex. In Winterer, E., Hussong, D., and Decker, R., editors, *The eastern Pacific Ocean and Hawaii*, pages 413–438. Boulder, CO: Geological Society of America, Geology of North America.

Enkelmann, E., Ehlers, T. A., Merli, G., and Methner, K. (2015). Thermal and exhumation history of the Eocene Chumstick Basin, Washington State, USA. *Tectonics*, 34(5):951–969.

Ewing, R., Weber, W., and Clinard, J. (1995). Radiation effects in nuclear waste forms for high-level radioactive waste. *Progress in Nuclear Energy*, 29(2):63–127.

Farley, K., Shuster, D., and Ketcham, R. (2011). U and Th zonation in apatite observed by laser ablation ICPMS, and implications for the (U–Th)/He system. *Geochimica et Cosmochimica Acta*, 75(16):4515–4530.

Farley, K. A. (2000). Helium diffusion from apatite: General behavior as illustrated by Durango fluorapatite. *Journal of Geophysical Research: Solid Earth*, 105(B2):2903–2914.

Farley, K. A., Shuster, D. L., Watson, E. B., Wanser, K. H., and Balco, G. (2010). Numerical investigations of apatite ^{4}He/^{3}He thermochronometry. *Geochemistry, Geophysics, Geosystems*, 11(10):1–18.

Farley, K. A., Wolf, R. A., and Silver, L. T. (1996). The effects of long alpha-stopping distances on (U-Th)/He ages. *Geochimica et Cosmochimica Acta*, 60(21):4223–4229.

Ferry, J. and Watson, E. (2007). New thermodynamic models and revised calibrations for the Ti-in-zircon and Zr-in-rutile thermometers. *Contributions to Mineralogy & Petrology*, 154:429–437.

Fitzgerald, P. G., Baldwin, S. L., Webb, L. E., and O'Sullivan, P. B. (2006). Interpretation of (U–Th)/ He single grain ages from slowly cooled crustal terranes: A case study from the Transantarctic Mountains of southern Victoria Land. *Chemical Geology*, 225:91–120.

Flowers, R. M., Ketcham, R. A., Shuster, D. L., and Farley, K. A. (2009). Apatite (U-Th)/He thermochronometry using a radiation damage accumulation and annealing model. *Geochimica et Cosmochimica Acta*, 73:2347–2365.

Forte, A. M., Whipple, K. X., Bookhagen, B., and Rossi, M. W. (2016). Decoupling of modern shortening rates, climate, and topography in the Caucasus. *Earth and Planetary Science Letters*, 449:282–294.

Gautheron, C., Tassan-Got, L., Barbarand, J., and Pagel, M. (2009). Effect of alpha-damage annealing on apatite (U–Th)/He thermochronology. *Chemical Geology*, 266:157–170.

Gautheron, C., Tassan-Got, L., Ketcham, R., and Dobson, K. (2012). Accounting for long alpha-particle stopping distances in (U–Th–Sm)/He geochronology: 3D modeling of diffusion, zoning, implantation, and abrasion. *Geochimica et Cosmochimica Acta*, 96:44–56.

Gradstein, F., Ogg, J., and Ogg, G. (2012). *The Geologic Time Scale 2012*. Elsevier Science, ProQuest E edition.

Guenther, W., Reiners, P., Ketcham, R., Nasdala, L., and Giester, G. (2013). Helium diffusion in natural zircon: Radiation damage, anisotropy, and the interpretation of zircon (U-Th)/He thermochronology. *American Journal of Science*, 313(3):145–198.

Gulick, S. P. S., Jaeger, J. M., Mix, A. C., Asahi, H., Bahlburg, H., Belanger, C. L., Berbel, G. B. B., Childress, L., Cowan, E., Drab, L., Forwick, M., Fukumura, A., Ge, S., Gupta, S., Kioka, A., Konno, S., LeVay, L. J., Marz, C., Matsuzaki, K. M., McClymont, E. L., Moy, C., Muller, J., Nakamura, A., Ojima, T., Ribeiro, F. R., Ridgway, K. D., Romero, O. E., Slagle, A. L., Stoner, J. S., St-Onge, G., Suto, I., Walczak, M. D., Worthington, L. L., Bailey, I., Enkelmann, E., Reece, R., and Swartz, J. M. (2015). Mid-Pleistocene climate transition drives net mass loss from rapidly uplifting St. Elias Mountains, Alaska. *Proceedings of the National Academy of Sciences of the United States of America*, 112:15042–15047.

Gulick, S. P. S., Reece, R. S., Christeson, G. L., Avendonk, H. V., Worthington, L. L., and Pavlis, T. L. (2013). Seismic images of the Transition fault and the unstable Yakutat–Pacific–North American triple junction. *Geology*, 41(5):571–575.

Hansen, K. and Reiners, P. (2006). Low temperature thermochronology of the southern East Greenland continental margin: evidence from apatite (U–Th)/He and fission track analysis and implications for intermethod calibration. *Lithos*, 92:117–136.

Harrison, T., Catlos, E., and Montel, J. (2002). U-Th-Pb dating of phosphate minerals. In Kohn, M., Rakovan, J., and Hughes, J., editors, *Phosphates: Geochemical, Geobiological, and Materials Importance*, pages 523–558. Washington, D.C.: Mineralogical Society of America.

Harrison, T. and Zeitler, P. (2005). Fundamentals of Noble Gas Thermochronometry. In Reiners, P., Ehlers, T., and Zeitler, P., editors, *Low-temperature thermochronology: techniques, interpretations, and applications*, pages 123–149. Volume 58: Mineralogical Society of America Geochemical Society.

Hickes, H. (2001). *Apatite and zircon (U-Th)/He thermochronology of the northern Coast Mountains, southeast Alaska*. M.S. thesis, Washington State University.

Hickes, H., Reiners, P., Donelick, R., and Stowell, H. (2000). Apatite and zircon (U-Th)/He-thermochronometry of the Northern Coast Mountains, Southeast Alaska. *Eos (Transactions, American Geophysical Union)*, 81, Abstract T51C-10.

Hodges, K. V., Wobus, C., Ruhl, K., Schildgen, T., and Whipple, K. (2004). Quaternary deformation, river steepening, and heavy precipitation at the front of the Higher Himalayan ranges. *Earth and Planetary Science Letters*, 220:379–389.

Horne, A. M., van Soest, M. C., Hodges, K. V., Tripathy-Lang, A., and Hourigan, J. K. (2016). Integrated single crystal laser ablation U/Pb and (U-Th)/He dating of detrital accessory minerals - Proof-of-concept studies of titanites and zircons from the Fish Canyon tuff. *Geochimica et Cosmochimica Acta*, 178:106–123.

Horstwood, M., Kosler, J., Gehrels, G., Jackson, S., McLean, N., Paton, C., Pearson, N., Sircombe, K., Sylvester, P., Vermeesch, P., Bowring, J., Condon, D., and Schoene, B. (2016). Community-Derived Standards for LA-ICP-MS U-(Th-)Pb Geochronology – Uncertainty Propagation, Age Interpretation and Data Reporting. *Geostandards and Geoanalytical Research*, 40(3):311–332.

Huntington, K. W., Klepeis, K. A., and 66 community contributors (2017). Challenges and opportunities for research in tectonics: Understanding deformation and the processes that link Earth systems, from geologic time to human time. A community vision document submitted to the U.S. National Science Foundation. Technical report.

Johnstone, S., Hourigan, J., and Gallagher, C. (2013). LA-ICP-MS depth profile analysis of apatite: protocol and implications for (U–Th)/He thermochronometry. *Geochimica et Cosmochimica Acta*, 109:143–161.

Kelsey, H., Ladinsky, T., Staisch, L., Sherrod, B., Blakely, R., Pratt, T., Stephenson, W., Odum, J., and Wan, E. (2017). The Story of a Yakima Fold and How It Informs Late Neogene and Quaternary Backarc Deformation in the Cascadia Subduction Zone, Manastash Anticline, Washington, USA. *Tectonics*, 36:2085–2107.

Ketcham, R., Gautheron, C., and Tassan-Got, L. (2011). Accounting for long alpha-particle stopping distances in (U-Th-Sm)/He geochronology: Refinement of the baseline case. *Geochimica et Cosmochimica Acta*, 75:7779–7791.

Ketcham, R. A. (2005). Forward and Inverse Modeling of Low-Temperature Thermochronometry Data. *Reviews in Mineralogy and Geochemistry*, 58(1):275–314.

Klepeis, K., Crawford, M., and Gehrels, G. (1998). Structural history of the crustal-scale Coast shear zone north of Portland Canal, southeast Alaska and British Columbia. *Journal of Structural Geology*, 20:883–904.

Kohn, M. J., Miselis, J. L., and Fremd, T. J. (2002). Oxygen isotope evidence for progressive uplift of the Cascade Range, Oregon. *Earth and Planetary Science Letters*, 204:151–165.

Koppers, A. A., Staudigel, H., and Wijbrans, J. R. (2000). Dating crystalline groundmass separates of altered Cretaceous seamount basalts by the 40Ar/39Ar incremental heating technique. *Chemical Geology*, 166(1-2):139–158.

Koppers, A. A. P., Staudigel, H., Pringle, M. S., and Wijbrans, J. R. (2003). Short-lived and discontinuous intraplate volcanism in the South Pacific: Hot spots or extensional volcanism? *Geochemistry, Geophysics, Geosystems*, 4(10):1–49.

Kuiper, K. F., Deino, A., Hilgen, F. J., Krijgsman, W., Renne, P. R., and Wijbrans, J. R. (2008). Synchronizing Rock Clocks of Earth History. *Science*, 320(5875):500–504.

Lopez, W. and Meigs, A. (2016). *Post 6.3 Ma Erosionally Driven Rock Uplift and Landscape Evolution of the Cascade Range in the Pacific Northwest*. Undergraduate thesis, Oregon State University.

McCaffrey, R., Qamar, A. I., King, R. W., Wells, R., Khazaradze, G., Williams, C. A., Stevens, C. W., Vollick, J. J., and Zwick, P. C. (2007). Fault locking, block rotation and crustal deformation in the Pacific Northwest. *Geophysical Journal International*, 169:1315–1340.

McDougall, I. and Harrison, T. M. (1999). *Geochronology and Thermochronology by the 40Ar/39Ar Method*. Oxford University Press, 2nd edition.

Min, K., Mundil, R., Renne, P., and Ludwig, K. (2000). A test for systematic errors in Ar-40/Ar-39 geochronology through comparison with U/Pb analysis of a 1.1-Ga rhyolite. *Geochimica et Cosmochimica Acta*, 64(1):73–98.

Murray, K. E., Orme, D. A., and Reiners, P. W. (2014). Effects of U-Th-rich grain boundary phases on apatite helium ages. *Chemical Geology*, 390:135–151.

Nabelek, P. I., Hofmeister, A. M., and Whittington, A. G. (2012). The influence of temperature-dependent thermal diffusivity on the conductive cooling rates of plutons and temperature-time paths in contact aureoles. *Earth and Planetary Science Letters*, 317-318:157–164.

Pavlis, T., Chapman, J., Bruhn, R., Ridgway, K., Worthington, L., Gulick, S., and Spotila, J. (2012). Structure of the actively deforming fold-thrust belt of the St . Elias orogen with implications for glacial exhumation and three-dimensional tectonic processes. *Geosphere*, 8(5):991–1019.

Perez, N. D., Meigs, A., Pesek, M., and Stockli, D. (2017). *Does erosional exhumation explain Late Cenozoic rock uplift of the Western Cascades, OR? Preliminary Results*, Poster session presented at the Feedbacks Among Climate, Erosion, and Tectonics II, Corvallis, OR.

Priest, G. R. (1990). Volcanic and Tectonic Evolution of the Cascade Volcanic Arc, Central Oregon. *Journal of Geophysical Research*, 95(B12):19583–19599.

Rasmussen, J. and Humphreys, E. (1988). Tomographic image of the Juan de Fuca Plate beneath Washington and western Oregon using teleseismic P-wave travel times. *Geophysical Research Letters*, 15(12):1417–1420.

Reiners, P. and Farley, K. (2001). Influence of crystal size on apatite (U-Th)/He thermochronology: an example from the Bighorn Mountains, Wyoming. *Earth and Planetary Science Letters*, 188:413–420.

Reiners, P. W., Ehlers, T. A., Garver, J. I., Mitchell, S. G., Montgomery, D. R., Vance, J. A., and Nicolescu, S. (2002). Late Miocene exhumation and uplift of the Washington Cascade Range. *Geology*, 30(9):767–770.

Reiners, P. W., Ehlers, T. A., Mitchell, S. G., and Montgomery, D. R. (2003). Coupled spatial variations in precipitation and long-term erosion rates across the Washington Cascades. *Nature*, 426:645–647.

Renne, P. R., Mundil, R., Balco, G., Min, K., and Ludwig, K. R. (2010). Joint determination of 40K decay constants and 40Ar*/40K for the Fish Canyon sanidine standard, and improved accuracy for 40Ar/39Ar geochronology. *Geochimica et Cosmochimica Acta*, 74(18):5349–5367.

Schmandt, B. and Humphreys, E. (2011). Seismically imaged relict slab from the 55 Ma Siletzia accretion to the northwest United States. *Geology*, 39(2):175–178.

Shuster, D. and Farley, K. (2005). 4He/3He Thermochronometry: Theory, Practice, and Potential

Implications. In Reiners, P., Ehlers, T., and Zeitler, P., editors, *Low-temperature thermochronology: techniques, interpretations, and applications*, pages 181–203. Volume 58: Mineralogical Society of America Geochemical Society.

Shuster, D. L., Flowers, R. M., and Farley, K. A. (2006). The influence of natural radiation damage on helium diffusion kinetics in apatite. *Earth and Planetary Science Letters*, 249(3-4):148–161.

Sláma, J., Kosler, J., Condon, D., Crowley, J., Gerdes, A., Hanchar, J., M.S.A., H., Morris, G., Nasdala, L., Norberg, N., Schaltegger, U., Schoene, B., Tubrett, M., and Whitehouse, M. (2008). Plesovice zircon – a new natural reference material for U-Pb and Hf isotopic microanalysis. *Chemical Geology*, 249:1–35.

Spiegel, C., Kohn, B., Belton, D., Berner, Z., and Gleadow, A. (2009). Apatite (U–Th–Sm)/He thermochronology of rapidly cooled samples: the effect of He implantation. *Earth and Planetary Science Letters*, 285:105–114.

Staisch, L., Blakely, R., Kelsey, H., Styron, R., and Sherrod, B. (2018). Crustal Structure and Quaternary Acceleration of Deformation Rates in Central Washington Revealed by Stream Profile Inversion, Potential Field Geophysics, and Structural Geology of the Yakima Folds. *Tectonics*, 37(6):1750–1770.

Staisch, L., Kelsey, H., Sherrod, B., Möller, A., Paces, J., Blakely, R., and Styron, R. (2017). Miocene – Pleistocene deformation of the Saddle Mountains: Implications for seismic hazard in central Washington , USA. *Geological Society of America Bulletin*, 130(3-4).

Steiger, R. and Jager, E. (1977). Subcommission on geochronology: Convention on the use of decay constants in geo- and cosmochronology. *Earth and Planetary Science Letters*, 36:359–362.

Surpless, B. E., Stockli, D. F., Dumitru, T. A., and Miller, E. L. (2002). Two-phase westward encroachment of Basin and Range extension into the northern Sierra Nevada. *Tectonics*, 21(1):2–1–13.

Swanson, D. and Wright, T. (1976). Field Guide to field trip between Pasco and Pullman, Washington, emphasizing stratigraphy, vent areas, and intracanyon flows of the Yakima Basalt. In

Geological Society of America Cordilleran Section meeting, Pullman, Washington, Field Guide.

Takeuchi, A., Hren, M. T., Smith, S. V., Chamberlain, C. P., and Larson, P. B. (2010). Pedogenic carbonate carbon isotopic constraints on paleoprecipitation: Evolution of desert in the Pacific Northwest, USA, in response to topographic development of the Cascade Range. *Chemical Geology*, 277(3-4):323–335.

Takeuchi, A. and Larson, P. B. (2005). Oxygen isotope evidence for the late Cenozoic development of an orographic rain shadow in eastern Washington, USA. *Geology*, 33(4):313–316.

Taylor Jr., H. P. (1971). Oxygen Isotope Evidence for Large-Scale Interaction between Meteoric Ground Waters and Tertiary Granodiorite Intrusions, Western Cascade Range, Oregon. *Journal of Geophysical Research*, 76(32):7855–7874.

Thompson, J., Meffre, S., Maas, R., Kamenetsky, V., Kamenetsky, M., Goemann, K., Ehrig, K., and Danyushevsky, L. (2016). Matrix effects in Pb/U measurements during LA-ICP-MS analysis of the mineral apatite. *Journal of Analytical Atomic Spectrometry*, 31:1206–1215.

Thomson, S., Gehrels, G., Ruiz, J., and Buchwaldt, R. (2012). Routine low-damage apatite U-Pb dating using laser ablation-multicollector-ICPMS. *Geochemistry, Geophysics, Geosystems*, 13(2):1–23.

Trench, D., Meigs, A., and Grunder, A. (2012). Termination of the northwestern Basin and Range province into a clockwise rotating region of transtension and volcanism, southeast Oregon. *Journal of Structural Geology*, 39:52–65.

Tripathy-Lang, A., Hodges, K. V., Monteleone, B. D., and Van Soest, M. C. (2013). Laser (U-Th)/He thermochronology of detrital zircons as a tool for studying surface processes in modern catchments. *Journal of Geophysical Research: Earth Surface*, 118(3):1333–1341.

Troitzsch, U. and Ellis, D. (2004). High P–T study of solid solutions in the system ZrO2–TiO2: the stability of srilankite. *European Journal of Mineralogy*, 16(4):577–584.

Troitzsch, U. and Ellis, D. (2005). The ZrO2–TiO2 phase diagram. *Journal of Materials Science*, 40(17):4571–4577.

Utevsky, E. (2015). *Geochemistry of Plutonic Rocks of the Western Cascades, Washington &*

Oregon: Relationship to Crustal Segmentation and Ore Genesis. M.S. thesis, Oregon State University.

van Soest, M. C., Hodges, K. V., Wartho, J. A., Biren, M. B., Monteleone, B. D., Spray, J. G., and Thompson, L. M. (2011). (U - Th)/He dating of terrestrial impact structures: The Manicouagan example. *Geochemistry, Geophysics, Geosystems*, 12(5):1–8.

Vance, J., Clayton, G., Mattinson, J., and Naeser, C. (1987). Early and middle Cenozoic stratigraphy of the Mount Rainier-Tieton River area, southern Washington Cascades. *Washington Division of Geology and Earth Resources Bulletin*, 77:269–290.

Vermeesch, P. (2018). IsoplotR: a free and open toolbox for geochronology. *Geoscience Frontiers*, 9:1479–1493.

Verplanck, E. (1985). "Temporal variations in volume and geochemistry of volcanism in the Western Cascades, Oregon.".

Walker, G. and MacLeod, N. (1991). "Geologic map of Oregon".

Watson, E., Wark, D., and Thomas, J. (2006). Crystallization thermometers for zircon and rutile. *Contributions to Mineralogy and Petrology*, 151:413–433.

Weber, W., Ewing, R., Catlow, C., Diaz de la Rubia, T., Hobbs, L., Kinoshita, C., Motta, A., Nastasi, M., Salie, E., Vance, E., and Zinkle, S. (1998). Radiation effects in crystalline ceramics for the immobilization of high-level nuclear waste and plutonium. *Journal of Materials Research*, 13(6):1434–1484.

Wells, R. E., Blakely, R. J., and Weaver, C. S. (2002). Cascadia microplate models and within-slab earthquakes. In Kirby, S., Wang, K., and Dunlop, S., editors, *Intraslab earthquakes in the Cascadia subduction system: Science and Hazards*, pages 17–24. U.S. Geological Survey Open File Report 2002-328.

Wells, R. E. and McCaffrey, R. (2013). Steady rotation of the Cascade arc. *Geology*, 41(9):1027–1030.

Willett, S. D. (1999). Orogeny and orography: The effects of erosion on the structure of mountain belts. *Journal of Geophysical Research: Solid Earth*, 104(B12):28957–28981.

Willigers, B., Baker, J., Krogstad, E., and Peate, D. (2002). Precise and accurate in situ Pb–Pb dating of apatite, monazite, and sphene by laser ablation multiple-collector ICP-MS. *Geochimica et Cosmochimica Acta*, 66(6):1051–1066.

Wolf, R., Farley, K., and Kass, D. (1998). Modeling of the temperature sensitivity of the apatite (U-Th)/He thermochronometer. *Chemical Geology*, 148:105–114.

Worthington, L., van Avendonk, H., Gulick, S., Christeson, G., and Pavlis, T. (2012). Crustal structure of the Yakutat Terrane and the evolution of subduction and collision in southern Alaska. *Journal of Geophysical Research*, 117(B1):1–20.

Zack, T., Moraes, R., and Kronz, A. (2004). Temperature dependence of Zr in rutile: empirical calibration of a rutile thermometer. *Contributions to Mineralogy and Petrology*, 148(4):471–488.

APPENDIX A

APATITE AND ZIRCON (U-Th)/He DATA

Sample	Latitude	Longitude	Elevation (m)	Method	Rsph-eq*	Length (μm)	Width (μm)	[238U] (ppm)	[232Th] Th (ppm)	eU	Mean F_T	Corrected Age (Ma)	Corrected 2σ Error (Ma)	Notes
17OR-18 a3	46.948	-121.532	917	conventional single crystal	60.9	136.2	115.7	6.68	12.97	10	0.728	5.40	0.54	
17OR-18 a4	46.948	-121.532	917	conventional single crystal	-	183.9	160.2	-	-	-	-	-	-	No age can be calculated.
17OR-18 a5	46.948	-121.532	917	conventional single crystal	-	382.3	156.6	-	-	-	-	-	-	Grain had an obvious high re-extract during He analysis- indicative of an inclusion not processed further.
17OR-18 a6	46.948	-121.532	917	conventional single crystal	71.7	257.3	117.5	31.75	45.4	43	0.765	5.40	0.19	Piece of crystal end chipped off.
17OR-10 a1	45.27	-121.82	825	conventional single crystal	60.2	217.7	98.3	5.08	17.36	9.2	0.716	3.79	0.38	Small inclusions.
17OR-10 a2	45.27	-121.82	825	conventional single crystal	55.2	227.5	87.8	1.37	1.67	1.8	0.701	4.00	1.63	Grain not euhedral. Small inclusions.
17OR-10 a3	45.27	-121.82	825	conventional single crystal	60.8	370.9	91.0	1.13	0.85	1.3	0.727	3.05	1.15	Small crack in the crystal. Small inclusions.
17OR-10 a5	45.27	-121.82	825	conventional single crystal	80.9	284.2	133.0	1.22	0.98	1.5	0.792	3.01	0.64	
17OR-10 a6	45.27	-121.82	825	conventional single crystal	70.8	402.3	106.9	1.01	1.05	1.3	0.761	2.13	0.67	
17OR-09 a001	44.57	-122.40	452	conventional single crystal	44.4	121.1	78.4	1.58	5.26	2.8	0.630	17.64	3.93	Small black inclusions.
17OR-09 a002	44.57	-122.40	452	conventional single crystal	53.1	183.3	87.8	3.23	11.23	5.9	0.683	10.33	0.86	Small inclusions.
17OR-09 a003	44.57	-122.40	452	conventional single crystal	-	232.0	98.0	-	-	-	-	-	-	Grain had an obvious high re-extract during He analysis- indicative of an inclusion not processed further.
17OR-09 a004	44.57	-122.40	452	conventional single crystal	46.4	166.7	75.9	2.24	7.32	4.0	0.642	13.72	1.74	
17OR-09 a6	44.57	-122.40	452	conventional single crystal	49.8	157.8	84.1	3.53	12.86	6.6	0.664	10.45	1.50	Small crack in the crystal. Slightly high re-extract during He analysis.
17OR-03 a001	43.72	-122.40	866	conventional single crystal	-	301.7	102.3	-	-	-		-	-	Grain had an obvious high re-extract during He analysis- indicative of an inclusion not processed further.
17OR-03 a003	43.72	-122.40	866	conventional single crystal	53.0	122.4	99.4	10.16	26.14	16.0	0.689	24.83	1.29	Small crack in the crystal. Small inclusions.
17OR-03 a004	43.72	-122.40	866	conventional single crystal	-	127.6	115.2	-	-	-	-	-	-	Grain had an obvious high re-extract during He analysis- indicative of an inclusion not processed further.
17OR-03 a005	43.72	-122.40	866	conventional single crystal	-	194.5	111.8	-	-	-	-	-	-	Grain had an obvious high re-extract during He analysis- indicative of an inclusion not processed further.
17OR-02 a001	42.81	-122.56	1204	conventional single crystal	69.1	269.1	111.1	2.07	5.15	3.3	0.752	17.98	1.29	No euhedral ends.
17OR-02 a002	42.81	-122.56	1204	conventional single crystal	50.2	176.2	82.5	2.16	5.73	3.5	0.668	19.86	1.98	Black inclusions.
17OR-02 a003	42.81	-122.56	1204	conventional single crystal	42.5	119.2	74.4	2.42	6.10	3.9	0.619	17.81	2.57	
17OR-02 a004	42.81	-122.56	1204	conventional single crystal	52.3	146.4	91.6	1.94	4.97	3.1	0.683	21.04	2.32	Inclusions.
17OR-02 a005	42.81	-122.56	1204	conventional single crystal	59.1	188.7	99.5	1.75	3.55	2.6	0.717	21.96	2.34	Inclusions.

*Rsph-eq is the equivalent spherical radius.

Table A.1: Apatite (U-Th)/He data of samples 17OR-18 (Site I), 17OR-10 (Site II), 17OR-09 (Site III), 17OR-03 (Site V), and 17OR-02 (Site VI).

Sample	Latitude	Longitude	Elevation (m)	Method	Rsph-eq*	Length (μm)	Width (μm)	[238U] (ppm)	[232Th] Th (ppm)	eU	Age (Ma)	2σ Error (Ma)	Notes
17OR-18 z01	46.948	-121.532	917	single crystal laser ablation	36.5	103.2	63.6	143.6	105.7	168.4	10.72	0.61	
17OR-18 z02	46.948	-121.532	917	single crystal laser ablation	40.5	142.2	66.6	184.0	114.1	210.7	10.68	0.59	
17OR-18 z03	46.948	-121.532	917	single crystal laser ablation	45.8	122.7	81.2	142.9	88.6	163.6	12.14	0.55	
17OR-18 z04	46.948	-121.532	917	single crystal laser ablation	51.5	180.3	84.9	111.8	68.3	127.8	18.76	0.84	
17OR-10 z02	45.27	-121.82	825	single crystal laser ablation	68.8	234.6	114.0	233.6	167.2	272.7	7.52	0.34	
17OR-10 z03	45.27	-121.82	825	single crystal laser ablation	59.8	180.6	102.3	200.6	160.2	238.1	7.58	0.35	
17OR-10 z04	45.27	-121.82	825	single crystal laser ablation	50.2	175.4	82.8	190.4	149.5	225.4	8.36	0.38	
17OR-10 z05	45.27	-121.82	825	single crystal laser ablation	50.4	139.0	88.7	215.4	199.5	262.1	8.66	0.39	
17OR-11 z02	45.30	-121.82	858	single crystal laser ablation	56.2	215.9	90.7	292.1	352.6	374.6	11.91	0.53	Older than crystallization age.
17OR-11 z03	45.30	-121.82	858	single crystal laser ablation	45.5	166.2	74.2	521.9	812.7	712.0	8.79	0.39	
17OR-11 z04	45.30	-121.82	858	single crystal laser ablation	75.2	296.4	120.7	293.1	310.6	365.8	8.22	0.37	
17OR-11 z05	45.30	-121.82	858	single crystal laser ablation	51.2	146.0	89.0	940.2	1274.5	1238.4	5.26	0.23	
17OR-11 z06	45.30	-121.82	858	single crystal laser ablation	65.2	203.8	110.4	237.8	213.5	287.7	8.45	0.37	
17OR-06 z01	44.57	-122.40	452	single crystal laser ablation	47.0	135.1	81.6	175.0	103.4	199.2	14.97	0.66	
17OR-06 z02	44.57	-122.40	452	single crystal laser ablation	46.8	149.3	79.0	191.7	144.0	225.4	21.52	0.92	Older than crystallization age.
17OR-06 z03	44.57	-122.40	452	single crystal laser ablation	47.5	137.8	82.2	245.5	146.5	279.7	15.49	0.67	
17OR-06 z05	44.57	-122.40	452	single crystal laser ablation	51.7	229.0	81.1	161.4	124.3	190.5	15.53	0.68	
17OR-06 z06	44.57	-122.40	452	single crystal laser ablation	46.5	131.4	81.1	58.5	31.7	65.9	13.90	0.70	

*Rsph-eq is an estimated equivalent spherical radius. Length and width measurements used were of the exposed spots of the mounted zircons on the surface of the puck.

Table A.2: Zircon (U-Th)/He data of samples 17OR-18 (Site I), 17OR-10 (Site II), 17OR-11 (Site II), and 17OR-06 (Site IV).

APPENDIX B

ZIRCON U-Pb DATA

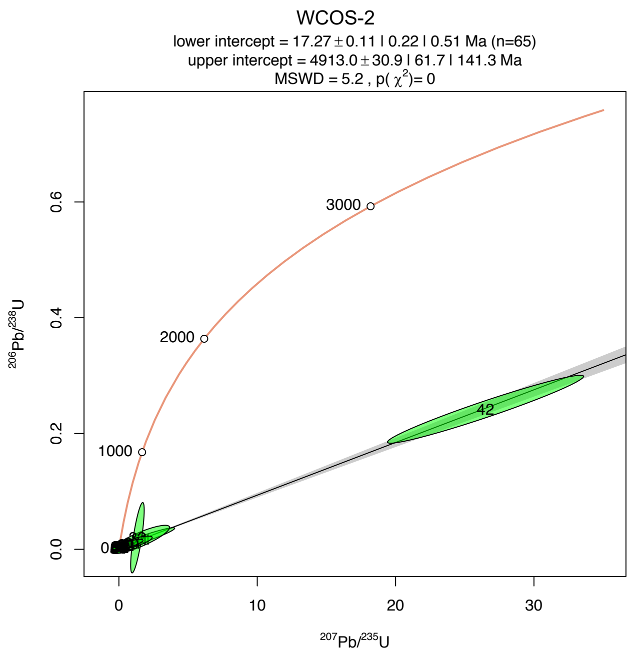

Figure B.1: Concordia diagram for re-dated Utevsky (2015) sample WCOS-2 (Site III) using IsoplotR by Vermeesch (2018).

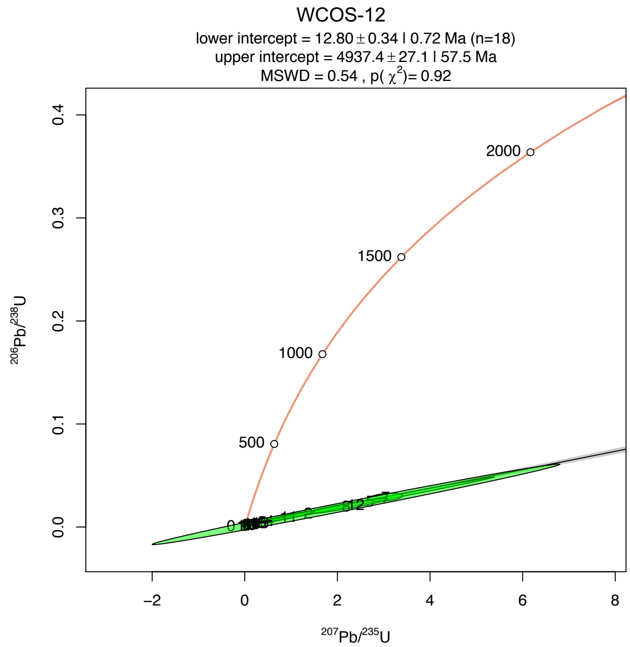

Figure B.2: Concordia diagram for re-dated Utevsky (2015) sample WCOS-12 using IsoplotR by Vermeesch (2018).

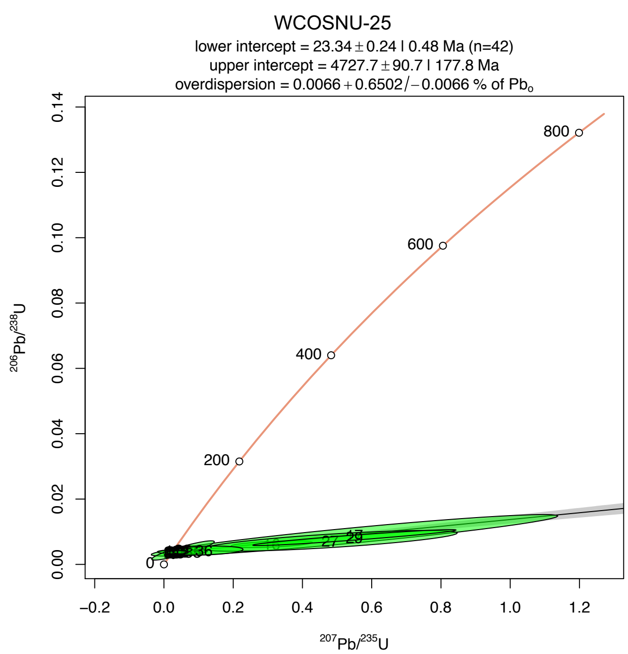

Figure B.3: Concordia diagram for re-dated Utevsky (2015) sample WCOSNU-25 (Site V) using IsoplotR by Vermeesch (2018).

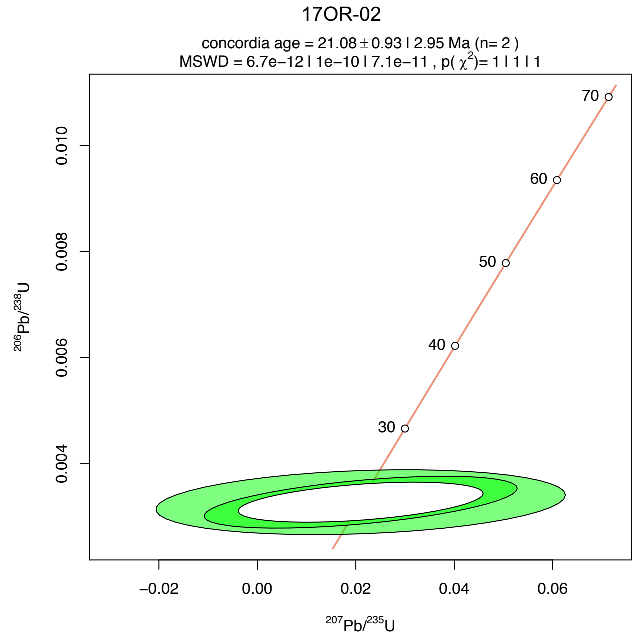

Figure B.4: Concordia diagram for sample 17OR-02 (Site VI) using IsoplotR by Vermeesch (2018).

Sample	Latitude	Longitude	Method	^{206}Pb/^{238}U Age	2σ Error (Ma)	^{207}Pb/^{235}U Age	2σ Error (Ma)	^{206}Pb/^{238}U	2σ Error	^{207}Pb/^{235}U	2σ Error	Weighted Mean Age (Ma)	2σ Error	Notes
17OR-18 z01	46.948	-121.532	LA-ICP-MS	23.94	0.51	26.2	2.2	0.0262	0.0022	0.003720	0.000079			
17OR-18 z02	46.948	-121.532	LA-ICP-MS	23.71	0.51	27.0	2.5	0.0270	0.0026	0.003685	0.000079	23.76	0.26	
17OR-18 z03	46.948	-121.532	LA-ICP-MS	23.80	0.55	27.2	2.0	0.0272	0.0020	0.003698	0.000086			
17OR-18 z04	46.948	-121.532	LA-ICP-MS	23.60	0.52	25.5	1.9	0.0255	0.0019	0.003668	0.000082			
17OR-10 z02	45.27	-121.82	LA-ICP-MS	9.66	0.22	12.2	1.2	0.001500	0.000035	0.0119	0.0011			
17OR-10 z03	45.27	-121.82	LA-ICP-MS	9.86	0.47	16.5	2.4	0.001531	0.000073	0.0163	0.0024	9.72	0.18	17OR-10 z04 affected by common Pb.
17OR-10 z04	45.27	-121.82	LA-ICP-MS	16.51	0.49	120.5	6.2	0.002565	0.000076	0.1266	0.0069			
17OR-10 z05	45.27	-121.82	LA-ICP-MS	9.84	0.41	15.3	2.3	0.001528	0.000064	0.0152	0.0023			
17OR-11 z02	45.30	-121.82	LA-ICP-MS	9.52	0.18	10.96	0.84	0.001478	0.000029	0.01086	0.00084			
17OR-11 z03	45.30	-121.82	LA-ICP-MS	9.60	0.15	11.02	0.74	0.001490	0.000023	0.01092	0.00074	9.55	0.08	
17OR-11 z04	45.30	-121.82	LA-ICP-MS	9.43	0.22	9.75	0.81	0.001463	0.000033	0.00966	0.00081			
17OR-11 z05	45.30	-121.82	LA-ICP-MS	9.55	0.14	9.85	0.43	0.001483	0.000021	0.00975	0.00043			
17OR-11 z06	45.30	-121.82	LA-ICP-MS	9.75	0.32	17.4	1.9	0.001514	0.000049	0.0191	0.0039			
17OR-06 z01	44.57	-122.40	LA-ICP-MS	19.48	0.8	42.6	5.5	0.00303	0.00012	0.043	0.0058			
17OR-06 z02	44.57	-122.40	LA-ICP-MS	19.78	0.59	48	6.5	0.003073	0.000092	0.047	0.0061	19.63	0.31	
17OR-06 z03	44.57	-122.40	LA-ICP-MS	19.56	0.6	40.4	4.2	0.003038	0.000093	0.0406	0.0043			
17OR-06 z05	44.57	-122.40	LA-ICP-MS	19.64	0.54	51.2	5.8	0.003052	0.000084	0.052	0.006			
17OR-06 z06	44.57	-122.40	LA-ICP-MS	20.56	0.95	55.9	6.2	0.00319	0.00015	0.0569	0.0065			

Table B.1: Zircon U-Pb data of samples 17OR-18 (Site I), 17OR-10 (Site II), 17OR-11 (Site II), and 17OR-06 (Site IV) collected concurrently with (U-Th)/He data.

Sample	$^{207}Pb/^{235}U$	± 2SE	$^{206}Pb/^{238}U$	± 2SE	$^{207}Pb/^{206}Pb$	± 2SE	$^{208}Pb/^{232}Th$	± 2SE	$^{206}Pb/^{208}Pb$	± 2SE	$^{207}Pb/^{235}U$ Age	± 2SE	$^{206}Pb/^{238}U$ Age	± 2SE	$^{208}Pb/^{232}Th$ Age	± 2SE	$^{207}Pb/^{206}Pb$ Age	± 2SE	$^{206}Pb/^{204}Pb$	$^{207}Pb/^{204}Pb$	$^{208}Pb/^{204}Pb$
WCOS-2-001	0.321	0.038	0.00513	0.00026	0.458	0.045	0.012	0.0025	0.738	0.096	285	31	33	1.7	242	51	4075	160	3300	1470	4100
WCOS-2-002	0.422	0.056	0.00628	0.00052	0.484	0.047	0.016	0.0035	0.676	0.088	351	39	40.4	3.3	321	69	4181	140	2000	890	2500
WCOS-2-003	0.026	0.01	0.00262	0.00021	0.076	0.032	0.00101	0.00031	4.6	1.2	25	10	16.9	1.3	20.3	6.2	600	830	2800	250	520
WCOS-2-004	0.0237	0.0038	0.002701	9.60E-05	0.0655	0.01	0.00109	0.00023	4.03	0.58	23.7	3.8	17.39	0.62	22	4.6	540	310	1500	65	230
WCOS-2-005	0.0344	0.0065	0.00291	0.00014	0.085	0.016	0.00137	0.0003	2.74	0.42	34.1	6.3	18.76	0.92	27.7	6	960	380	1100	69	350
WCOS-2-006	0.037	0.0049	0.00277	0.00014	0.104	0.017	0.00158	0.00033	2.49	0.39	36.8	4.8	17.84	0.9	31.8	6.7	1540	300	1600	140	470
WCOS-2-007	0.76	0.18	0.0091	0.0015	0.524	0.068	0.0243	0.0067	0.728	0.12	518	98	58	9.5	483	130	4170	230	1800	1110	3500
WCOS-2-008	0.0211	0.0032	0.002591	8.60E-05	0.0599	0.0095	0.000982	0.00021	4.85	0.9	21.1	3.2	16.68	0.55	19.8	4.2	390	300	600	65	250
WCOS-2-009	0.0191	0.0038	0.0027	0.00013	0.054	0.011	0.00098	0.00021	3.82	0.64	19.1	3.7	17.37	0.81	19.8	4.2	180	380	1600	104	420
WCOS-2-010	0.059	0.017	0.00303	0.00019	0.126	0.029	0.00231	0.00074	3.39	0.62	57	16	19.5	1.2	47	15	1520	370	2100	180	500
WCOS-2-011	0.0177	0.0037	0.00252	0.00011	0.053	0.011	0.000767	0.00016	5.11	0.86	17.7	3.7	16.21	0.69	15.5	3.3	-10	350	1400	49	310
WCOS-2-012	0.101	0.031	0.00334	0.00028	0.19	0.044	0.0048	0.0015	3.67	0.99	98	28	21.5	1.8	96	30	1870	510	900	230	700
WCOS-2-013	0.0193	0.0035	0.002632	9.60E-05	0.0545	0.0099	0.000856	0.00019	6.9	1.4	19.3	3.4	16.95	0.62	17.3	3.8	140	340	2300	141	630
WCOS-2-014	0.0168	0.0039	0.00266	0.00011	0.048	0.012	0.00096	0.00022	5.77	1	16.9	3.9	17.1	0.73	19.3	4.5	-40	410	2000	90	360
WCOS-2-015	0.0194	0.0043	0.00246	0.00014	0.06	0.014	0.00082	0.00019	6.1	1.3	19.5	4.3	15.85	0.91	16.5	3.9	380	460	1000	20	60
WCOS-2-016	0.0212	0.004	0.0027	0.00011	0.0563	0.011	0.000931	0.00018	2.49	0.35	21.3	4	17.41	0.73	18.8	3.7	320	390	3000	130	1100
WCOS-2-017	0.0217	0.0044	0.00276	0.00012	0.059	0.013	0.000851	0.00019	5.15	1	21.8	4.3	17.74	0.78	17.2	3.7	300	420	1400	95	290
WCOS-2-018	0.0229	0.0052	0.00278	0.00013	0.061	0.014	0.00091	0.00021	5.7	1.4	22.8	5.1	17.87	0.86	18.4	4.3	200	440	590	23	140
WCOS-2-019	0.084	0.03	0.0034	0.00032	0.163	0.043	0.0039	0.0013	2.4	0.57	79	27	21.9	2.1	79	27	1980	460	1500	170	640
WCOS-2-020	0.117	0.029	0.00367	0.00033	0.215	0.045	0.0059	0.002	2.31	0.63	109	26	23.6	2.1	118	39	2580	430	1600	130	500
WCOS-2-021	1.76	0.94	0.018	0.0079	0.62	0.12	0.059	0.031	0.52	0.11	860	310	115	49	1130	570	4420	430	2500	1300	4600
WCOS-2-023	0.053	0.02	0.00294	0.0002	0.109	0.034	0.00193	0.00071	4.11	0.74	50	18	18.9	1.3	39	14	860	470	6700	470	2000
WCOS-2-024	0.052	0.016	0.00292	0.00013	0.116	0.032	0.00176	0.00054	2.98	0.56	49	15	18.81	0.85	35.5	11	980	440	1200	370	1300
WCOS-2-025	0.037	0.013	0.003	0.00017	0.079	0.021	0.00159	0.00061	5.41	1	36	12	19.3	1.1	32	12	860	510	-100	50	130
WCOS-2-026	0.064	0.02	0.00306	0.00028	0.149	0.037	0.00265	0.00099	2.29	0.47	62	18	19.7	1.8	53	20	1930	520	1800	250	1040
WCOS-2-027	0.0162	0.0018	0.002685	6.00E-05	0.0442	0.005	0.00086	0.00017	4.76	0.62	16.3	1.8	17.29	0.39	17.38	3.4	-90	210	1000	-40	150
WCOS-2-028	0.0239	0.0049	0.00285	0.00012	0.067	0.014	0.00125	0.0003	6	1.2	23.9	4.8	18.33	0.76	25.2	6.1	400	380	1000	100	320
WCOS-2-029	0.0218	0.0037	0.00269	0.00011	0.0608	0.011	0.000939	0.0002	6.8	1.7	21.8	3.6	17.29	0.68	19	4	340	350	2400	40	170
WCOS-2-030	0.223	0.082	0.00429	0.00066	0.315	0.079	0.0051	0.0018	1.44	0.36	189	63	27.6	4.2	103	35	3100	450	5500	1700	7200
WCOS-2-031	0.178	0.09	0.00409	0.00081	0.218	0.083	0.0043	0.002	2.72	0.73	148	70	26.3	5.2	87	40	1820	720	70000	600	2000
WCOS-2-032	0.23	0.14	0.0045	0.0012	0.223	0.091	0.0056	0.0031	3.15	0.82	177	97	28.6	8	113	62	1860	710	0	900	1700
WCOS-2-033	1.54	0.88	0.017	0.01	0.66	0.22	0.04	0.021	0.59	0.17	840	350	108	64	780	400	4580	550	3700	2450	6200
WCOS-2-034	1.34	0.22	0.02	0.012	0.67	0.21	0.027	0.0067	0.79	0.53	857	91	128	75	538	130	4530	700	3700	3700	70000
WCOS-2-035	0.55	0.17	0.0079	0.0015	0.423	0.066	0.0219	0.0074	0.82	0.15	399	100	50.8	9.7	430	150	3880	250	4000	2700	5700
WCOS-2-036	0.99	0.58	0.0108	0.0049	0.42	0.15	0.04	0.024	1.63	0.72	530	270	69	31	780	460	3300	790	70000	3000	7100
WCOS-2-037	0.04	0.02	0.00284	0.00017	0.118	0.048	0.00137	0.0005	3.12	0.63	39	18	18.3	1.1	27.6	10	1110	520	8100	1190	3200
WCOS-2-038	0.0182	0.0028	0.002808	9.00E-05	0.0489	0.008	0.000993	0.0002	5.19	0.75	18.8	3.1	18.07	0.58	20.1	4.1	40	300	3200	390	570
WCOS-2-039	0.038	0.032	0.00265	0.00023	0.063	0.013	0.0016	0.0012	3.23	0.53	35	25	17.1	1.5	31	24	420	330	1000	500	1200
WCOS-2-040	0.512	0.1	0.00688	0.00087	0.51	0.067	0.0127	0.0031	0.71	0.14	403	70	44.2	5.6	255	62	4170	250	3800	4300	8500
WCOS-2-041	0.162	0.044	0.00404	0.00037	0.244	0.05	0.0058	0.0015	1.74	0.41	143	35	26	2.3	117	31	2390	530	-200	-120	-500
WCOS-2-042	0.82	0.39	0.0094	0.0032	0.38	0.11	0.0248	0.011	2.64	0.99	490	190	60	20	490	210	2680	780	300	1200	2600

Table B.2: Zircon U-Pb data for re-dated Utevsky (2015) sample WCOS-2 (Site III).

Sample	^{207}Pb/^{235}U	± 2SE	^{206}Pb/^{238}U	± 2SE	^{207}Pb/^{206}Pb	± 2SE	^{208}Pb/^{232}Th	± 2SE	^{206}Pb/^{208}Pb	± 2SE	^{207}Pb/^{235}U Age	± 2SE	^{206}Pb/^{238}U Age	± 2SE	^{208}Pb/^{232}Th Age	± 2SE	^{207}Pb/^{206}Pb Age	± 2SE	^{206}Pb/^{204}Pb	^{207}Pb/^{204}Pb	^{208}Pb/^{204}Pb
WCOS-2-043	0.0201	0.0026	0.002795	8.40E-05	0.0517	0.007	0.000944	0.00018	2.5	0.34	20.2	2.6	17.99	0.54	19.07	3.7	190	260	-40000	-270	0
WCOS-2-044	26.5	3.6	0.242	0.024	0.809	0.069	1.014	0.21	0.408	0.05	3350	140	1400	120	14120	2100	4983	160	4070	5460	10900
WCOS-2-045	0.0204	0.0027	0.002606	6.30E-05	0.0563	0.0072	0.000855	0.00017	3.44	0.47	20.5	2.7	16.78	0.4	17.3	3.5	330	250	-4600	-350	-700
WCOS-2-046	0.0209	0.0035	0.00277	0.00014	0.0563	0.01	0.001063	0.00022	3.85	0.68	20.9	3.5	17.85	0.9	21.5	4.4	270	350	-3200	-220	-700
WCOS-2-047	0.0251	0.0057	0.002673	8.00E-05	0.066	0.013	0.0011	0.00031	3.63	0.53	25	5.5	17.21	0.51	22.3	6.2	620	340	-60000	-600	-3500
WCOS-2-048	0.027	0.014	0.002652	9.90E-05	0.0572	0.01	0.00094	0.00021	5.18	1.1	26	12	17.07	0.64	19.1	4.2	270	350	-1400	-20	-100
WCOS-2-049	0.0239	0.0052	0.002607	9.20E-05	0.065	0.013	0.00093	0.00021	4.08	0.72	23.9	5.1	16.78	0.59	18.8	4.3	560	400	-18000	-900	-50000
WCOS-2-050	0.052	0.017	0.00296	0.00023	0.131	0.038	0.00226	0.00074	2.27	0.83	52	16	19.1	1.5	46	15	1990	670	24000	2500	17000
WCOS-2-051	0.0174	0.0024	0.002542	6.70E-05	0.0496	0.0068	0.000848	0.00017	4.59	0.62	17.5	2.4	16.36	0.43	17.13	3.4	110	270	14000	340	2600
WCOS-2-052	0.0203	0.003	0.00268	0.00011	0.055	0.0085	0.000889	0.00019	6.03	1	20.4	2.9	17.26	0.7	18	3.8	270	310	30000	0	300
WCOS-2-053	0.0178	0.0028	0.002637	7.10E-05	0.0479	0.007	0.000848	0.00018	5.47	0.83	17.9	2.8	16.98	0.46	17.1	3.6	10	260	23000	370	4600
WCOS-2-054	0.48	0.11	0.00634	0.00091	0.516	0.068	0.0139	0.0033	0.684	0.11	386	74	40.7	5.8	279	66	4240	200	48000	8300	94000
WCOS-2-055	0.0194	0.0038	0.00266	0.00011	0.052	0.011	0.00086	0.0002	7.2	1.4	19.4	3.8	17.13	0.7	17.3	4.1	130	380	67000	660	17000
WCOS-2-056	0.0253	0.0061	0.00284	0.00021	0.067	0.017	0.00121	0.00027	3.51	0.79	25.4	6	18.3	1.4	24.5	5.5	670	570	600000	450	900000
WCOS-2-057	0.0214	0.0044	0.00264	0.00015	0.057	0.012	0.00083	0.00018	6.11	1.1	21.4	4.4	17.03	0.94	16.8	3.6	360	420	-130000	-310	40000
WCOS-2-058	0.0192	0.0036	0.0025	0.00011	0.058	0.012	0.000925	0.0002	4.58	0.74	19.2	3.5	16.11	0.71	18.7	4	300	370	-27000	1000	-3400
WCOS-2-059	0.0286	0.0088	0.002652	9.80E-05	0.072	0.018	0.0013	0.00037	4.33	0.72	28.3	8.4	17.07	0.63	26.3	7.6	580	370	-29000	3200	-6000
WCOS-2-060	0.195	0.072	0.00416	0.00067	0.282	0.084	0.0086	0.0032	3.2	1.7	171	60	26.7	4.3	173	64	2510	850	-26000	75000	-33000
WCOS-2-061	0.0241	0.0064	0.00267	0.00021	0.062	0.014	0.00092	0.00029	6.2	1.6	24.1	6.4	17.2	1.4	18.6	5.9	530	510	-90000	14000	-1200
WCOS-2-062	0.0186	0.0027	0.00266	0.00012	0.0522	0.008	0.000793	0.00017	5.77	1.2	18.6	2.7	17.11	0.76	16	3.4	170	300	-500	-200	170
WCOS-2-063	0.0208	0.0044	0.002666	0.0001	0.059	0.013	0.00102	0.00022	6.29	1.2	20.8	4.4	17.16	0.66	20.7	4.4	160	390	-400	-70	-260
WCOS-2-064	0.0272	0.0054	0.00408	0.00015	0.048	0.0097	0.001246	0.00025	3.04	0.45	27.2	5.4	26.24	0.97	25.2	5	-10	370	-46000	-6100	-14800
WCOS-2-065	0.0379	0.0062	0.00354	0.00014	0.08	0.013	0.00154	0.00032	3.21	0.46	37.5	6	22.75	0.93	31.1	6.4	850	350	-13100	-2000	-5400
WCOS-2-066	0.025	0.0039	0.00375	0.00016	0.0504	0.0082	0.00139	0.00029	4.58	0.76	24.9	3.8	24.15	1	28	5.9	60	300	-600	20	0
WCOS-2-067	0.0168	0.0019	0.00246	7.10E-05	0.0503	0.0053	0.000812	0.00016	4.51	0.61	16.9	1.9	15.84	0.46	16.4	3.2	180	220	-29000	-2300	-70000

Table B.3: Zircon U-Pb data for re-dated Utevsky (2015) sample WCOS-2 (Site III) (continued).

Sample	$^{207}Pb/^{235}U$	± 2SE	$^{206}Pb/^{238}U$	± 2SE	$^{207}Pb/^{206}Pb$	± 2SE	$^{208}Pb/^{232}Th$	± 2SE	$^{206}Pb/^{208}Pb$	± 2SE	$^{207}Pb/^{235}U$ Age	± 2SE	$^{206}Pb/^{238}U$ Age	± 2SE	$^{208}Pb/^{232}Th$ Age	± 2SE	$^{207}Pb/^{206}Pb$ Age	± 2SE	$^{206}Pb/^{204}Pb$	$^{207}Pb/^{204}Pb$	$^{208}Pb/^{204}Pb$
WCOS-12-001	0.421	0.04	0.00535	0.00021	0.566	0.051	0.01104	0.0021	0.561	0.07	355	28	34.4	1.4	222	43	4404	140	5700	1400	11100
WCOS-12-002	1.37	0.28	0.0136	0.0022	0.667	0.068	0.0402	0.012	0.474	0.063	780	120	87	14	790	230	4650	160	6600	1300	10200
WCOS-12-003	0.373	0.077	0.00512	0.00071	0.506	0.073	0.0093	0.0027	0.709	0.12	322	60	32.9	4.5	186	53	4090	240	3400	540	3900
WCOS-12-004	0.0342	0.0072	0.00204	0.00013	0.12	0.022	0.00094	0.00022	1.75	0.29	34	7	13.12	0.86	19.1	4.5	1760	390	600	-40	-100
WCOS-12-005	0.54	0.12	0.0064	0.00088	0.56	0.067	0.0126	0.0037	0.606	0.086	418	75	41.1	5.6	253	72	4310	210	800	240	1400
WCOS-12-006	2.7	1.1	0.0251	0.0096	0.739	0.065	0.063	0.03	0.439	0.055	1170	210	157	58	1170	510	4823	150	3370	1500	7400
WCOS-12-007	0.087	0.018	0.00265	0.0003	0.248	0.054	0.00244	0.00052	1.23	0.23	84	17	17	1.9	49.3	11	2840	430	50	-20	-50
WCOS-12-008	0.044	0.011	0.00227	0.00018	0.125	0.03	0.00113	0.00029	2.51	0.64	44	11	14.6	1.2	22.8	5.8	1700	700	360	25	290
WCOS-12-009	3.04	0.28	0.0289	0.0016	0.785	0.078	0.0909	0.017	0.408	0.052	1413	71	183.6	10	1758	320	4930	180	3600	1590	8200
WCOS-12-010	0.0239	0.0062	0.00205	0.00013	0.087	0.022	0.00087	0.00024	2.17	0.4	23.8	6	13.18	0.85	17.6	4.8	1020	460	300	0	170
WCOS-12-011	0.0133	0.005	0.00197	0.00019	0.055	0.022	0.000632	0.00014	2.77	0.57	13.3	5	12.7	1.2	12.8	2.8	-20	660	-900	-24	-440
WCOS-12-012	2.19	0.41	0.0202	0.0031	0.783	0.078	0.056	0.015	0.415	0.052	1120	150	129	20	1100	280	4920	180	3400	1550	7500
WCOS-12-013	0.075	0.029	0.00258	0.0003	0.186	0.058	0.0016	0.00049	1.86	0.59	70	25	16.6	1.9	32.2	9.9	1720	660	700	60	430
WCOS-12-014	0.041	0.0099	0.00227	0.00016	0.137	0.031	0.00108	0.00028	1.45	0.21	40.4	9.5	14.6	1	21.9	5.7	1910	370	-500	-30	100
WCOS-12-015	0.074	0.014	0.00246	0.00019	0.207	0.03	0.00159	0.00041	1.141	0.16	72	13	15.8	1.2	32	8.3	2770	270	200	-10	200
WCOS-12-016	0.063	0.016	0.00235	0.00016	0.175	0.034	0.00137	0.00035	1.31	0.21	61	14	15.1	1.1	27.7	7	2260	420	1000	130	1100
WCOS-12-017	0.029	0.02	0.00271	0.00069	0.091	0.065	0.0008	0.00039	-24	30	28	19	17.5	4.4	16.2	7.9	100	1300	30	0	60
WCOS-12-018	0.95	0.24	0.0101	0.0023	0.671	0.076	0.0172	0.0052	0.485	0.066	640	120	64	14	344	100	4660	180	4600	2020	8700
WCOS-12-019	2.4	1.8	0.022	0.016	0.683	0.08	0.075	0.057	0.472	0.067	910	320	138	93	1300	940	4680	190	2700	1230	5000
WCOS-12-020	0.34	0.11	0.00437	0.00076	0.434	0.079	0.011	0.004	1.02	0.21	262	70	28.1	4.8	220	80	3760	300	20	80	260
WCOS-12-021	0.57	0.27	0.0071	0.0023	0.43	0.12	0.0156	0.0077	0.98	0.29	390	150	46	14	310	150	3540	610	-600	-280	-600
WCOS-12-022	0.073	0.015	0.0027	0.00017	0.203	0.039	0.00203	0.00053	1.65	0.3	71	14	17.4	1.1	41	11	2620	360	-90	0	-120
WCOS-12-023	0.059	0.017	0.0024	0.00021	0.176	0.042	0.00172	0.00052	1.35	0.25	58	16	15.4	1.4	34.8	10	2080	540	-1000	-60	-340
WCOS-12-024	0.226	0.065	0.00413	0.00084	0.386	0.071	0.0045	0.0021	0.749	0.13	201	51	26.6	5.4	91	42	3750	300	-200	-60	200
WCOS-12-025	0.145	0.069	0.00323	0.00059	0.275	0.091	0.0038	0.0018	1.09	0.26	130	57	20.8	3.8	76	37	2950	520	100	90	400
WCOS-12-026	0.283	0.046	0.00431	0.00035	0.473	0.063	0.00527	0.0011	0.676	0.1	249	36	27.7	2.2	106.2	22	4070	230	1400	610	1800
WCOS-12-027	0.082	0.054	0.00266	0.0006	0.186	0.058	0.0022	0.0012	1.8	0.32	72	39	17.1	3.9	44	24	2050	590	160	120	200
WCOS-12-028	0.046	0.02	0.00228	0.00027	0.135	0.047	0.00152	0.00052	1.94	0.39	44	18	14.7	1.7	30.7	11	1290	630	170	-20	-70
WCOS-12-029	0.0154	0.0036	0.002013	9.50E-05	0.054	0.013	0.000587	0.00013	3.18	0.54	15.4	3.6	12.96	0.61	11.9	2.5	140	430	500	34	210
WCOS-12-030	0.146	0.046	0.00341	0.0004	0.279	0.074	0.0043	0.0015	1.73	0.52	132	40	22	2.6	87	30	2460	690	100	90	290
WCOS-12-034	0.078	0.026	0.00255	0.00029	0.207	0.049	0.0028	0.0013	1.87	0.43	73	22	16.4	1.9	57	26	2110	600	100	47	50

Table B.4: Zircon U-Pb data for re-dated Utevsky (2015) sample WCOS-12.

Sample	$^{207}Pb/^{235}U$	± 2SE	$^{206}Pb/^{238}U$	± 2SE	$^{207}Pb/^{206}Pb$	± 2SE	$^{208}Pb/^{232}Th$	± 2SE	$^{206}Pb/^{208}Pb$	± 2SE	$^{207}Pb/^{235}U$ Age	± 2SE	$^{206}Pb/^{238}U$ Age	± 2SE	$^{208}Pb/^{232}Th$ Age	± 2SE	$^{207}Pb/^{206}Pb$ Age	± 2SE	$^{206}Pb/^{204}Pb$	$^{207}Pb/^{204}Pb$	$^{208}Pb/^{204}Pb$
WCOSNU-25-001	0.0254	0.0043	0.00336	0.00013	0.0545	0.0096	0.00125	0.00027	4.79	0.76	25.4	4.2	21.64	0.85	25.2	5.5	210	330	200	6	-50
WCOSNU-25-002	0.0243	0.0077	0.00354	0.00026	0.047	0.015	0.00135	0.0003	4.1	0.78	24.2	7.6	22.8	1.7	27.2	6.1	-60	550	1800	42	540
WCOSNU-25-003	0.025	0.011	0.00353	0.00038	0.056	0.025	0.0014	0.00044	5.6	1.6	24	11	22.7	2.5	28.2	8.8	0	810	600	-11	20
WCOSNU-25-004	0.0325	0.0044	0.00422	0.00019	0.0554	0.0072	0.00134	0.00028	5.22	0.96	32.5	4.3	27.1	1.2	27.1	5.6	410	310	-2500	-10	-400
WCOSNU-25-005	0.0243	0.0051	0.00353	0.00014	0.0505	0.011	0.00125	0.00027	5.76	1.1	24.2	5	22.7	0.88	25.3	5.5	-60	370	1400	32	360
WCOSNU-25-006	0.0302	0.0054	0.00361	0.00016	0.063	0.012	0.00156	0.00034	4.5	0.93	30	5.3	23.23	1	31.6	6.9	360	370	1700	62	590
WCOSNU-25-007	0.078	0.02	0.00417	0.00046	0.136	0.03	0.00311	0.00086	2.92	0.91	75	18	26.8	3	63	17	1970	440	1400	62	590
WCOSNU-25-008	0.028	0.007	0.00344	0.00027	0.06	0.016	0.00102	0.00027	5.5	1.3	28	6.9	22.1	1.8	20.6	5.4	410	530	1600	31	530
WCOSNU-25-009	0.0323	0.0058	0.00354	0.00014	0.07	0.014	0.00156	0.00035	4.35	0.83	32.1	5.7	22.81	0.9	31.5	7	580	370	2300	107	780
WCOSNU-25-010	0.0291	0.0091	0.00379	0.00046	0.057	0.021	0.0012	0.00043	9.2	9.7	29.1	8.9	24.4	3	24.2	8.6	290	720	-2000	-84	-600
WCOSNU-25-011	0.053	0.014	0.00391	0.0003	0.104	0.029	0.00189	0.00057	5.8	1.6	52	13	25.1	1.9	38.1	11	1080	550	900	130	140
WCOSNU-25-012	0.0274	0.0044	0.00419	0.00015	0.049	0.0085	0.00144	0.00031	10.9	1.9	27.3	4.3	26.94	0.94	29.1	6.3	30	310	-200	-66	-330
WCOSNU-25-013	0.0231	0.0076	0.00362	0.00016	0.045	0.014	0.00128	0.00029	4.39	0.75	23	7.4	23.3	1	25.8	5.8	-220	490	2600	90	2200
WCOSNU-25-014	0.0321	0.0068	0.00386	0.0002	0.06	0.012	0.0014	0.00032	5.09	0.94	31.9	6.7	24.8	1.3	28.2	6.5	320	390	-1600	-90	-1000
WCOSNU-25-015	0.0413	0.006	0.0038	0.0002	0.0776	0.012	0.00161	0.00035	3.83	0.64	41	5.8	24.5	1.3	32.6	7	1000	350	0	90	200
WCOSNU-25-016	0.311	0.054	0.00618	0.00043	0.344	0.052	0.0129	0.0031	1.23	0.28	264	42	39.7	2.8	259	62	3370	340	1100	530	80000
WCOSNU-25-017	0.55	0.24	0.0089	0.0026	0.386	0.082	0.022	0.012	1.25	0.29	400	140	57	16	420	220	3350	450	1900	700	20000
WCOSNU-25-018	0.0237	0.0051	0.00351	0.00025	0.051	0.011	0.00116	0.00029	4.97	1.1	23.7	5.1	22.6	1.6	23.5	5.8	190	430	800	10	10000
WCOSNU-25-019	0.047	0.027	0.00386	0.00029	0.092	0.053	0.00154	0.00043	4.8	1.7	46	26	24.8	1.8	31.1	8.7	600	1300	5500	340	-41000
WCOSNU-25-025	0.0267	0.0089	0.00368	0.0003	0.054	0.018	0.00105	0.00024	5.5	1.3	26.4	8.6	23.7	1.9	21.2	4.9	-40	530	-700	-18	10
WCOSNU-25-027	0.0344	0.0075	0.00366	0.00021	0.068	0.015	0.00129	0.00029	5.1	1	34.1	7.3	23.6	1.4	26	5.8	560	440	5100	171	570
WCOSNU-25-028	0.046	0.016	0.00399	0.00031	0.082	0.028	0.00194	0.00055	3.51	0.76	45	16	25.7	2	39.1	11	550	760	-700	11	-150
WCOSNU-25-029	0.0251	0.0047	0.00349	0.00014	0.0523	0.01	0.00121	0.00026	4.41	0.7	25.1	4.6	22.44	0.91	24.4	5.3	140	370	700	7	260
WCOSNU-25-031	0.0404	0.009	0.00377	0.00024	0.079	0.017	0.00222	0.00055	3	0.62	40	8.8	24.3	1.6	44.7	11	880	500	-400	-8	-140
WCOSNU-25-032	0.0362	0.0077	0.00357	0.00016	0.075	0.016	0.00135	0.00029	4.91	0.92	35.9	7.4	22.9	1	27.2	5.9	640	430	1300	6	190
WCOSNU-25-033	0.0278	0.0053	0.00381	0.00018	0.0541	0.011	0.0012	0.00026	4.22	0.76	27.7	5.2	24.5	1.1	24.2	5.3	170	380	10200	120	1500
WCOSNU-25-034	0.48	0.16	0.0072	0.0013	0.318	0.072	0.0139	0.0053	1.95	0.45	344	99	45.9	8.2	276	100	2620	510	-2000	-500	-3200
WCOSNU-25-035	0.055	0.037	0.00427	0.00095	0.08	0.032	0.0021	0.0011	3.32	0.73	50	30	27.5	6.1	42	22	670	630	9600	250	3600
WCOSNU-25-036	0.55	0.13	0.0082	0.001	0.421	0.057	0.0187	0.0053	0.841	0.12	407	76	52.5	6.6	372	100	3850	200	50000	-100	-1800
WCOSNU-25-037	0.0253	0.0054	0.00363	0.00016	0.052	0.012	0.00116	0.00025	5.39	1	25.2	5.3	23.37	1	23.5	5	0	390	41000	440	7400
WCOSNU-25-038	0.0372	0.0076	0.00366	0.00019	0.074	0.015	0.00155	0.00034	4.42	0.9	36.9	7.5	23.6	1.2	31.3	6.9	670	460	670000	9100	57000
WCOSNU-25-039	0.0303	0.0072	0.00351	0.0002	0.065	0.017	0.00134	0.0003	4.63	0.95	30.1	7.1	22.6	1.3	27	6.1	330	490	520000	4600	34000
WCOSNU-25-040	0.0246	0.0073	0.00367	0.00023	0.05	0.016	0.00126	0.00032	7.1	2.1	24.5	7.3	23.6	1.4	25.5	6.4	-110	550	-7.00E+07	-7300	-99600
WCOSNU-25-042	0.0577	0.0097	0.00419	0.00029	0.108	0.021	0.00207	0.00046	3.08	0.61	59.1	10	26.9	1.9	41.9	9.4	1480	360	170000	35000	-510000
WCOSNU-25-043	0.084	0.018	0.00372	0.00031	0.153	0.03	0.00369	0.00095	1.94	0.48	81	17	23.9	2	74	19	2180	430	88000	18000	280000
WCOSNU-25-044	0.116	0.046	0.00422	0.00057	0.175	0.068	0.0045	0.0017	2.8	0.93	105	40	27.1	3.7	90	34	1510	800	37000	2000	30000
WCOSNU-25-045	0.049	0.014	0.0041	0.00032	0.085	0.021	0.00238	0.00073	3.8	1.1	48	13	26.4	2.1	48	15	770	490	44000	990	20000
WCOSNU-25-047	0.0357	0.0063	0.00361	0.00019	0.075	0.014	0.00119	0.00027	6.2	1.3	35.4	6.2	23.2	1.2	24.1	5.4	640	380	20000	870	5000
WCOSNU-25-048	0.0392	0.0091	0.00376	0.00026	0.083	0.022	0.00194	0.00061	3.84	0.97	38.9	8.8	24.2	1.7	39.1	12	1020	490	25000	800	7800
WCOSNU-25-049	0.031	0.011	0.00359	0.00023	0.064	0.023	0.00146	0.00041	4.35	1	31	11	23.1	1.5	29.5	8.3	430	680	5500	160	1400
WCOSNU-25-050	0.0256	0.0065	0.00364	0.00019	0.052	0.013	0.00128	0.00029	3.51	0.61	25.5	6.4	23.4	1.2	25.9	5.9	30	470	3300	29	1600
WCOSNU-25-051	0.0476	0.0098	0.00373	0.00022	0.1	0.022	0.00189	0.00043	3.69	0.67	49	10	24	1.4	38.1	8.6	1100	500	3200	160	610
17OR-02-Z1	0.045	0.016	0.00353	0.00025	0.082	0.03	0.00237	0.00058	2.84	3.4	44	15	22.7	1.6	47.9	12	600	530	120	-9	24
17OR-02-Z2	0.15	0.066	0.00465	0.00067	0.236	0.038	0.00349	0.0018	1.156	0.094	142	52	29.9	4.3	70	37	3090	180	6600	3100	6100

Table B.5: Zircon U-Pb data for re-dated Utevsky (2015) sample WCOSNU-25 (Site V) and sample 17OR-02 (Site VI).

Sample Information	
Sample Designation	WCOS-2, WCOS-12, WCOSNU-25
Sample Type	pluton
Laboratory & Sample Preparation	
Laboratory name	Dept of Geology & Geophysics, Texas A&M University
Sample type/mineral	Bedrock zircons
Sample preparation	Conventional mineral separation, 1 inch resin mount, 1μm polish to finish
Imaging	optical scan
Analysis Date(s)	10/24/18
Laser ablation system	
Make, Model & type	ESI/New Wave Research, 193nm excimer, ns
Ablation cell & volume	NWR TV2 cell
Laser wavelength (nm)	193 nm
Pulse width (ns)	4 ns
Fluence ($J.cm^{-2}$)	4.6
Repetition rate (Hz)	15 Hz
Spot size (μm)	30 μm
Sampling mode / pattern	stationary circle
Carrier gas	He 0.6 l/min, Ar make-up gas 0.8 l/min combined 1/4 of way along sample line.
Ablation duration (secs)	30 s
Cell carrier gas flow (l/min)	0.6 l/min
ICP-MS Instrument	
Make, Model & type	ThermoScientific iCAP RQ
Sample introduction	Ablation aerosol directly to injector
RF power (W)	1450W
Make-up gas flow (l/min)	0.8 l/min Ar
Detection system	pulse / analog SEM (analog trigger >2.5M cps)
Masses measured	29Si, 31P, 45Sc, 49Ti, 88Sr, 89Y, 93Nb, 139La, 140Ce, 141Pr, 142Nd, 152Sm, 153Eu, 157Gd, 159Tb, 164Dy, 165Ho, 166Er, 169Tm, 174Yb, 175Lu, 178Hf, 181Ta, 202Hg, 204Pb, 206Pb, 207Pb, 208Pb, 232Th, 235U, 238U, 232Th.16O, 238U.16O
Integration time per peak (ms)	varies, 0.01 to 0.05 sec
Total integration time per reading (secs)	
Sensitivity / Efficiency (%, element)	7.5E3 to 10E3 CPS/ppm (NIST 612)
IC Dead time (ns)	20 ns
Data Processing	
Gas blank	10 second on-peak zero subtracted
Calibration strategy	91500 primary reference material (U-Th-Pb) and NIST 610, 612, 614 (concentrations)
Reference Material info	91500 (Wiedenbeck et al 1995)
Data processing package used / Correction for LIEF	Qtegra (concentrations) and Iolite (U-Th-Pb ages)
Mass discrimination	$^{207}Pb/^{206}Pb$ and $^{206}Pb/^{238}U$ normalised to reference material using Iolite; DRS: U-Pb Geochron 4; Parameters: Exponential down-hole correction, Cutoff Threshold = 10000, 235U calculated from 238U
Common-Pb correction, composition and uncertainty	not corrected; 204Pb not resolvable from zero after Hg correction
Uncertainty level & propagation	Ages are quoted at 2σ absolute, propagation is by quadratic addition. Excess uncertainty propagated.
Other information	Puck was heated in drying oven at 70°C for 24 hours prior to analysis to set the resin.

Table B.6: Metadata for zircon LA-ICP-MS U-Th-Pb analyses of re-dated Utevsky (2015) samples WCOS-2 (Site III), WCOS-12, and WCOSNU-25 (Site V). Modified from Horstwood et al. (2016).

Sample Information	
Sample Designation	17OR-02
Sample Type	pluton
Laboratory & Sample Preparation	
Laboratory name	Dept of Geology & Geophysics, Texas A&M University
Sample type/mineral	Bedrock zircons
Sample preparation	Conventional mineral separation, 1 inch resin mount, 1μm polish to finish
Imaging	optical scan
Analysis Date(s)	10/12/18
Laser ablation system	
Make, Model & type	ESI/New Wave Research, 193nm excimer, ns
Ablation cell & volume	NWR TV2 cell
Laser wavelength (nm)	193 nm
Pulse width (ns)	4 ns
Fluence ($J.cm^{-2}$)	4.6*
Repetition rate (Hz)	15 Hz
Spot size (μm)	30 μm
Sampling mode / pattern	stationary circle
Carrier gas	He 0.6 l/min, Ar make-up gas 0.8 l/min combined 1/4 of way along sample line.
Ablation duration (secs)	30 s
Cell carrier gas flow (l/min)	0.6 l/min
ICP-MS Instrument	
Make, Model & type	ThermoScientific iCAP RQ
Sample introduction	Ablation aerosol directly to injector
RF power (W)	1450W
Make-up gas flow (l/min)	0.8 l/min Ar
Detection system	pulse / analog SEM (analog trigger >2.5M cps)
Masses measured	29Si, 31P, 45Sc, 49Ti, 88Sr, 89Y, 93Nb, 139La, 140Ce, 141Pr, 142Nd, 152Sm, 153Eu, 157Gd, 159Tb, 164Dy, 165Ho, 166Er, 169Tm, 174Yb, 175Lu, 178Hf, 181Ta, 202Hg, 204Pb, 206Pb, 207Pb, 208Pb, 232Th, 235U, 238U, 232Th.16O, 238U.16O
Integration time per peak (ms)	varies, 0.01 to 0.05 sec
Total integration time per reading (secs)	
Sensitivity / Efficiency (%, element)	7.5E3 to 10E3 CPS/ppm (NIST 612)
IC Dead time (ns)	20 ns
Data Processing	
Gas blank	10 second on-peak zero subtracted
Calibration strategy	91500 primary reference material (U-Th-Pb) and NIST 610, 612, 614 (concentrations)
Reference Material info	91500 (Wiedenbeck et al 1995)
Data processing package used / Correction for LIEF	Qtegra (concentrations) and Iolite (U-Th-Pb ages)
Mass discrimination	$^{207}Pb/^{206}Pb$ and $^{206}Pb/^{238}U$ normalised to reference material using Iolite; DRS: U-Pb Geochron 4; Parameters: Exponential down-hole correction, Cutoff Threshold = 10000, 235U calculated from 238U
Common-Pb correction, composition and uncertainty	not corrected; 204Pb not resolvable from zero after Hg correction
Uncertainty level & propagation	Ages are quoted at 2σ absolute, propagation is by quadratic addition. Excess uncertainty propagated.
*Approximate fluence value.	

Table B.7: Metadata for zircon LA-ICP-MS U-Th-Pb analyses of sample 17OR-02 (Site VI). Modified from Horstwood et al. (2016).

APPENDIX C

APATITE U-Pb DATA

Of the four samples dated for apatite U-Pb by LA-ICP-MS, only sample 17OR-18 in southern Washington produced a meaningful cooling age, 22.10 ± 2.50 Ma, that was younger than the zircon U-Pb crystallization age, 23.76 ± 0.26 Ma. The apatite U-Pb results from samples 17OR-03, 17OR-09, and 17OR-10 were discarded from this study. In general, the apatite grains had very low U and Th concentrations, which could explain why some of the apatite U-Pb analyses were not successful.

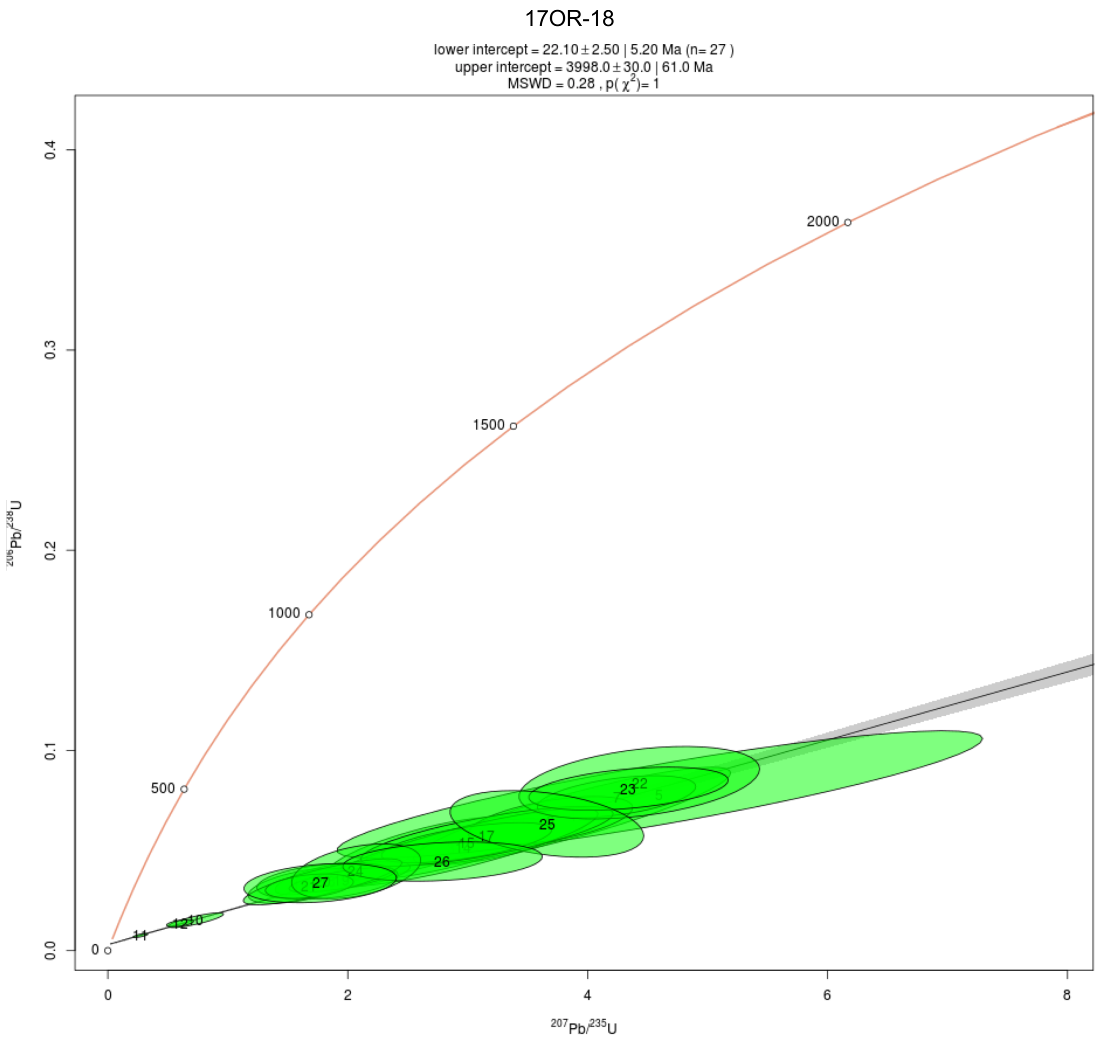

Figure C.1: Concordia diagram for sample 17OR-18 (Site I) using IsoplotR by Vermeesch (2018).

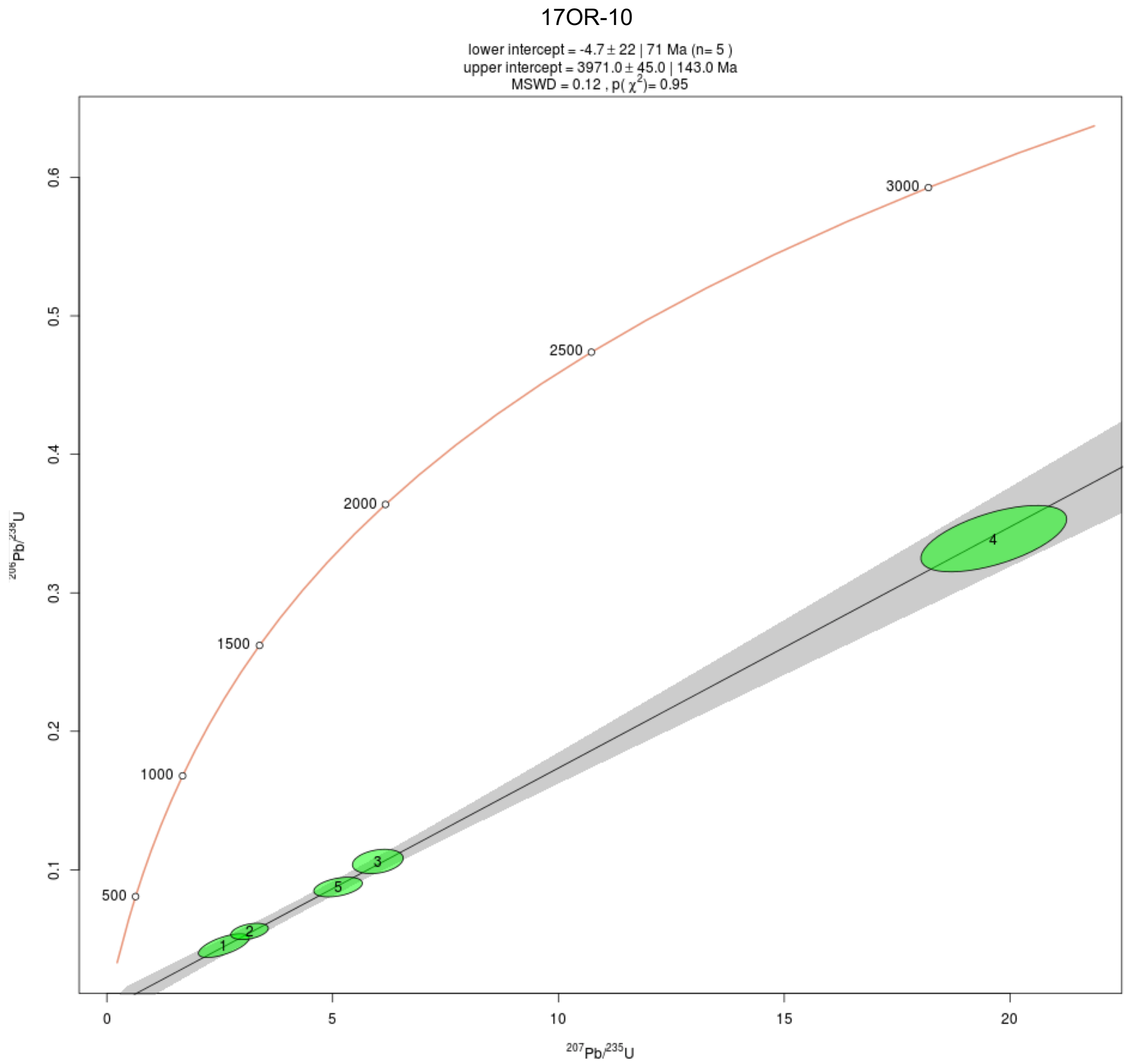

Figure C.2: Concordia diagram for sample 17OR-10 (Site II) using IsoplotR by Vermeesch (2018).

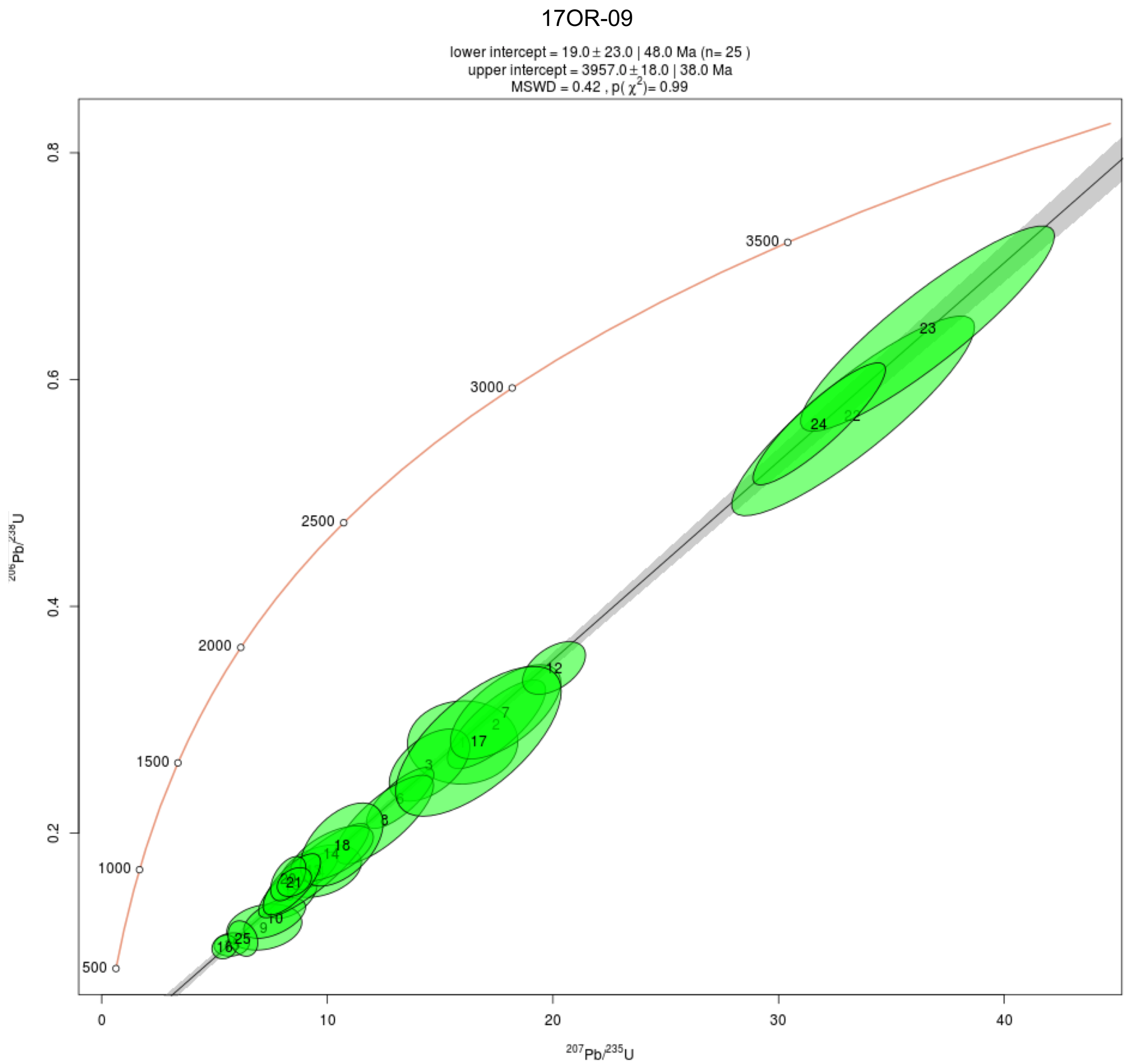

Figure C.3: Concordia diagram for sample 17OR-09 (Site III) using IsoplotR by Vermeesch (2018).

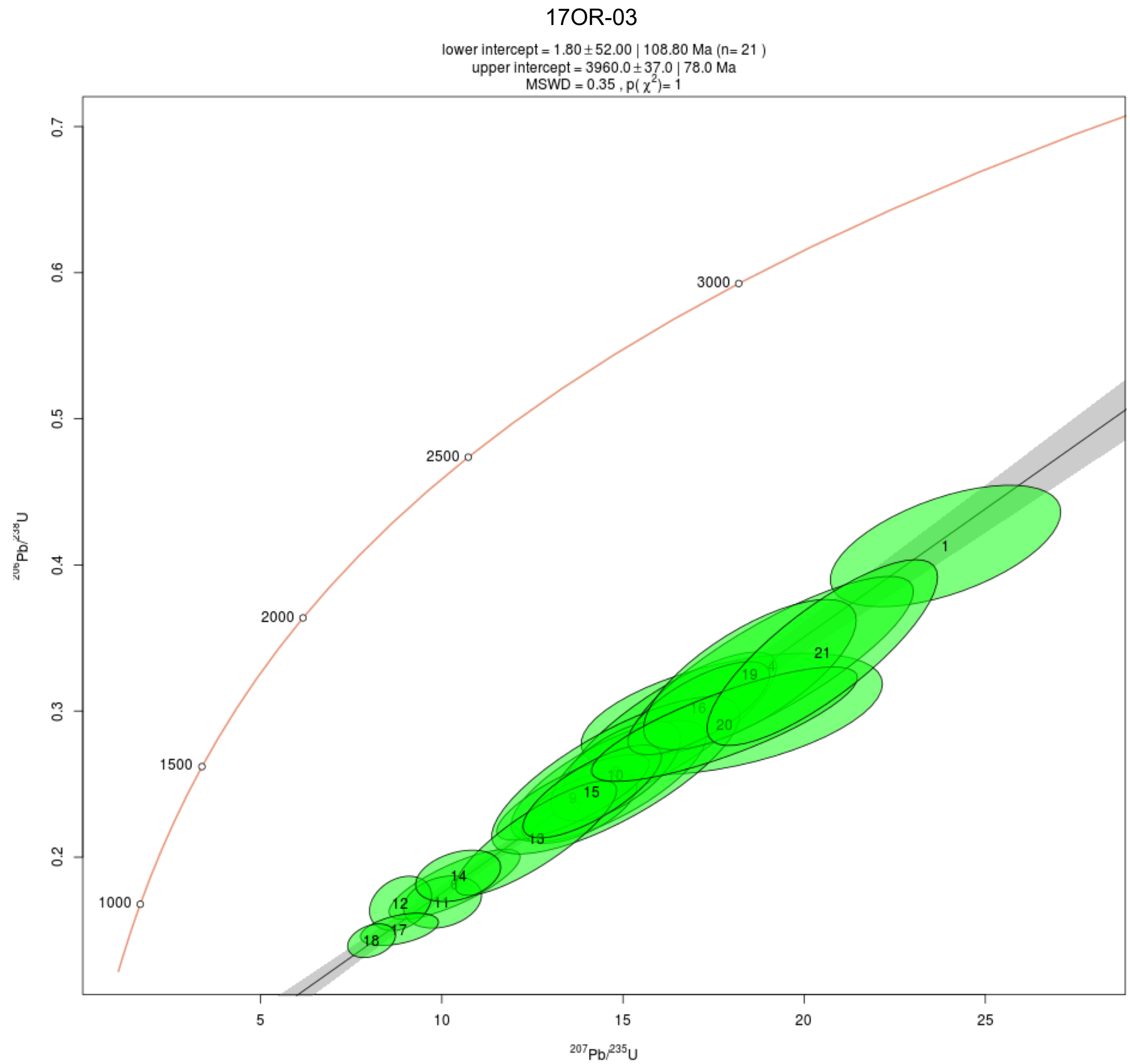

Figure C.4: Concordia diagram for sample 17OR-03 (Site V) using IsoplotR by Vermeesch (2018).

Sample	$^{207}Pb/^{235}U$	± 2SE	$^{206}Pb/^{238}U$	± 2SE	$^{207}Pb/^{206}Pb$	± 2SE	$^{208}Pb/^{232}Th$	± 2SE	$^{206}Pb/^{208}Pb$	± 2SE	$^{207}Pb/^{235}U$ Age	± 2SE	$^{206}Pb/^{238}U$ Age	± 2SE	$^{208}Pb/^{232}Th$ Age	± 2SE	$^{207}Pb/^{206}Pb$ Age	± 2SE	$^{206}Pb/^{204}Pb$	$^{207}Pb/^{204}Pb$	$^{208}Pb/^{204}Pb$
17OR18-002	3.26	0.4	0.0562	0.0056	0.418	0.04	0.0338	0.003	0.497	0.033	1463	110	351	34	671	59	3960	150	12	18	21
17OR18-003	2.61	0.37	0.051	0.0065	0.384	0.039	0.0316	0.0037	0.515	0.043	1276	100	319	40	627	72	3810	170	13	20	31
17OR18-004	2.86	0.4	0.0508	0.0063	0.425	0.042	0.0352	0.0043	0.487	0.033	1342	100	318	38	698	84	3960	150	22	31	60
17OR18-005	3.87	0.61	0.0674	0.01	0.416	0.038	0.0445	0.007	0.491	0.031	1560	120	431	64	870	130	3970	160	10.2	15	33
17OR18-006	4.6	1.1	0.078	0.013	0.4	0.054	0.0445	0.0077	0.507	0.043	1660	180	484	78	880	150	3830	200	12	15	33
17OR18-007	3.69	0.4	0.065	0.005	0.427	0.04	0.0706	0.0068	0.481	0.032	1546	83	405	30	1370	130	3950	140	10.5	13.3	27
17OR18-008	4.24	0.42	0.0769	0.0045	0.408	0.035	0.0802	0.0075	0.492	0.022	1664	82	477	27	1550	140	3894	140	12.8	21	48
17OR18-009	1.82	0.18	0.0359	0.002	0.377	0.035	0.01643	0.00063	0.51	0.03	1043	64	228	12	329	13	3770	130	9	9	24
17OR18-010	2.08	0.24	0.0376	0.003	0.411	0.039	0.0187	0.0015	0.481	0.032	1120	76	238	18	375	29	3890	140	7.2	16	52
17OR18-011	0.734	0.11	0.0152	0.0015	0.345	0.033	0.01014	0.00086	0.568	0.037	539	64	97.2	9.8	204	17	3650	140	5.7	5.3	10
17OR18-012	0.272	0.032	0.00755	0.00043	0.257	0.023	0.00621	0.0004	0.735	0.047	241	25	48.5	2.7	125.1	8	3190	150	22	11.4	40
17OR18-013	0.602	0.064	0.0137	0.00076	0.322	0.029	0.01209	0.00059	0.596	0.03	473	40	87.7	4.9	243	12	3530	140	-98	13.5	104
17OR18-014	1.76	0.2	0.0357	0.0033	0.367	0.034	0.0247	0.0028	0.521	0.029	1009	73	226	20	491	56	3740	160	-45	18	260
17OR18-015	2.96	0.51	0.0516	0.0081	0.439	0.045	0.0345	0.006	0.481	0.03	1310	130	322	49	680	120	3980	160	-21	13	150
17OR18-016	2.99	0.36	0.0539	0.0042	0.404	0.04	0.0338	0.0025	0.521	0.035	1378	84	338	25	670	48	3890	160	-48	28	330
17OR18-017	1.61	0.22	0.0324	0.0037	0.376	0.046	0.0215	0.0035	0.524	0.052	953	83	205	23	429	68	3730	180	-37	16	210
17OR18-018	3.16	0.49	0.0571	0.0062	0.395	0.042	0.0334	0.0041	0.519	0.035	1400	120	357	37	662	79	3830	160	-29	14	180
17OR18-019	1.83	0.28	0.0347	0.0037	0.396	0.059	0.0204	0.0024	0.493	0.043	1053	110	219	23	407	47	3840	230	-16	5	67
17OR18-020	1.95	0.23	0.0353	0.0026	0.396	0.035	0.0176	0.0015	0.513	0.036	1076	76	223	16	352	29	3850	140	-27	13	110
17OR18-021	1.79	0.31	0.0344	0.0048	0.38	0.04	0.0172	0.002	0.507	0.039	1003	93	217	29	345	40	3770	150	-77	25	160
17OR18-022	1.68	0.19	0.0322	0.0026	0.387	0.044	0.0173	0.0015	0.49	0.032	989	70	204	16	347	29	3790	160	-82	10	42
17OR18-023	4.43	0.53	0.0839	0.0076	0.387	0.046	0.0468	0.003	0.516	0.041	1705	95	519	45	924	59	3810	180	90	11	43
17OR18-024	4.34	0.47	0.0809	0.0046	0.384	0.037	0.0501	0.0034	0.511	0.035	1686	94	501	28	988	66	3820	140	46	20	56
17OR18-025	9.5	7.6	0.18	0.16	0.37	0.047	0.098	0.071	0.532	0.06	2080	550	930	630	1700	1100	3750	180	10	15	32
17OR18-026	2.07	0.27	0.0396	0.0056	0.392	0.059	0.0192	0.0015	0.551	0.083	1127	92	250	35	385	30	3800	250	10	15	25
17OR18-027	3.66	0.43	0.0633	0.0069	0.423	0.073	0.0362	0.0028	0.459	0.054	1553	92	395	42	719	55	3930	220	10	11	31
17OR18-028	2.79	0.4	0.0445	0.004	0.432	0.063	0.029	0.0026	0.458	0.061	1336	100	281	25	578	50	3960	230	6.7	12.2	20
17OR18-029	1.77	0.29	0.0337	0.0041	0.384	0.067	0.0222	0.0019	0.441	0.064	1017	110	213	25	443	37	3750	290	0.9	2	5
17OR18-030	11.2	3.3	0.198	0.052	0.39	0.035	0.12	0.034	0.48	0.046	2300	310	1130	280	2240	600	3880	150	22	37	63
17OR10-010	2.59	0.3	0.0452	0.0036	0.426	0.039	0.0542	0.0041	0.488	0.02	1273	85	284	22	1065	79	3960	140	4.9	9.7	11.3
17OR10-011	3.16	0.29	0.0555	0.0026	0.422	0.035	0.0704	0.0029	0.484	0.022	1439	73	348	16	1374	55	3963	120	7.6	14.4	17
17OR10-012	6	0.5	0.106	0.004	0.411	0.031	0.065	0.0023	0.484	0.018	1968	75	649	24	1272	43	3941	120	31	62	55
17OR10-013	19.64	1.6	0.3391	0.012	0.419	0.028	0.2393	0.0049	0.484	0.011	3067	79	1890	59	4336	81	3967	100	8.4	15.2	15.3
17OR10-014	5.12	0.44	0.0875	0.0033	0.424	0.031	0.0639	0.0024	0.476	0.018	1830	74	540	19	1251	46	3986	120	6	10.3	10

Table C.1: Apatite U-Pb data for samples 17OR-18 (site I) and 17OR-10 (Site II).

Sample	$^{207}Pb/^{235}U$	± 2SE	$^{206}Pb/^{238}U$	± 2SE	$^{207}Pb/^{206}Pb$	± 2SE	$^{208}Pb/^{232}Th$	± 2SE	$^{206}Pb/^{208}Pb$	± 2SE	$^{207}Pb/^{235}U$ Age	± 2SE	$^{206}Pb/^{238}U$ Age	± 2SE	$^{208}Pb/^{232}Th$ Age	± 2SE	$^{207}Pb/^{206}Pb$ Age	± 2SE	$^{206}Pb/^{204}Pb$	$^{207}Pb/^{204}Pb$	$^{208}Pb/^{204}Pb$
17OR09-001	16	1.6	0.28	0.016	0.406	0.041	0.1822	0.0099	0.481	0.029	2864	97	1591	81	3380	170	3900	150	-76	-7100	-570
17OR09-002	17.5	1.6	0.296	0.016	0.419	0.029	0.1839	0.0087	0.472	0.019	2955	86	1670	82	3410	150	3971	100	-80	-770	-469
17OR09-003	14.53	1.3	0.26	0.014	0.399	0.031	0.1615	0.0059	0.502	0.014	2779	87	1488	69	3025	100	3892	120	2780	-222	-720
17OR09-004	9.73	1	0.1666	0.01	0.413	0.041	0.1221	0.0065	0.494	0.043	2398	100	992	55	2330	120	3930	150	530	-220	-830
17OR09-005	8.35	0.79	0.1453	0.0088	0.41	0.035	0.0998	0.0051	0.481	0.037	2262	88	873	50	1921	93	3926	130	490	-200	-880
17OR09-006	13.23	1.2	0.231	0.012	0.408	0.028	0.1589	0.0077	0.484	0.012	2686	83	1349	57	2980	130	3929	100	320	-132	-493
17OR09-007	17.9	1.7	0.307	0.018	0.417	0.032	0.197	0.011	0.476	0.015	2973	93	1720	89	3630	180	3957	110	342	-112	-436
17OR09-009	12.53	1.3	0.212	0.017	0.425	0.033	0.1775	0.0067	0.482	0.021	2629	95	1234	88	3300	120	3985	110	640	-97	-350
17OR09-010	7.21	0.87	0.1172	0.0086	0.436	0.053	0.0875	0.0079	0.455	0.041	2126	110	714	50	1690	150	4000	190	1350	-93	-268
17OR09-011	7.67	0.8	0.1251	0.0077	0.439	0.039	0.0938	0.0061	0.47	0.023	2178	94	759	44	1810	110	4021	140	-1300	-107	-370
17OR09-012	9.46	0.81	0.1669	0.0074	0.412	0.029	0.169	0.0053	0.478	0.013	2373	81	994	41	3153	92	3941	100	-660	-95	-340
17OR09-013	20.05	1.6	0.3457	0.011	0.423	0.028	0.2315	0.0061	0.488	0.013	3091	78	1913	54	4208	100	3987	100	-319	-75.8	-246
17OR09-014	9.4	1.2	0.167	0.017	0.405	0.033	0.1262	0.0085	0.491	0.022	2340	130	988	97	2400	150	3906	130	-236	-69	-231
17OR09-015	10.21	1.1	0.182	0.011	0.4	0.034	0.1296	0.0047	0.497	0.021	2443	96	1079	58	2462	85	3892	130	-178	-84	-282
17OR09-016	5.76	0.54	0.1018	0.0046	0.411	0.037	0.0672	0.0022	0.488	0.026	1930	80	624	27	1315	43	3913	130	10	-2	-60
17OR09-017	5.45	0.47	0.0997	0.0047	0.396	0.033	0.0661	0.0024	0.486	0.024	1887	75	612	27	1293	45	3869	130	40	29	80
17OR09-018	16.7	1.9	0.281	0.027	0.422	0.041	0.0733	0.006	0.478	0.029	2901	120	1590	140	1430	110	3970	140	-108	-59	-188
17OR09-019	10.64	1.1	0.19	0.015	0.415	0.04	0.0916	0.0051	0.466	0.026	2482	94	1120	81	1770	94	3940	150	-91	-46	-142
17OR09-020	8.43	0.82	0.155	0.011	0.4	0.031	0.135	0.011	0.496	0.021	2264	88	929	62	2550	200	3889	120	-130	-64	-183
17OR09-021	8.27	0.69	0.1599	0.0085	0.387	0.03	0.0941	0.0042	0.478	0.016	2263	82	955	47	1816	77	3860	110	-104	-49	-150
17OR09-022	8.54	0.71	0.1569	0.0059	0.397	0.029	0.1071	0.0034	0.478	0.013	2283	74	939	33	2055	62	3879	110	-70	-35.7	-101
17OR09-023	33.3	3.3	0.568	0.037	0.423	0.028	0.36	0.02	0.468	0.012	3570	100	2890	160	6200	290	3985	98	-57.9	-32.3	-85
17OR09-024	36.6	3.6	0.645	0.039	0.409	0.027	0.382	0.021	0.476	0.016	3664	100	3190	160	6520	310	3937	98	-59.2	-33.4	-85.8
17OR09-025	31.8	2.7	0.561	0.024	0.4066	0.026	0.337	0.011	0.474	0.013	3538	83	2865	100	5870	170	3931	96	-53.1	-31.6	-78.1
17OR09-026	6.26	0.54	0.1071	0.0067	0.417	0.042	0.117	0.016	0.479	0.021	2010	75	655	39	2240	290	3950	140	20	70	30

Table C.2: Apatite U-Pb data for sample 17OR-09 (Site III).

Sample	^{207}Pb/^{235}U	± 2SE	^{206}Pb/^{238}U	± 2SE	^{207}Pb/^{206}Pb	± 2SE	^{208}Pb/^{232}Th	± 2SE	^{206}Pb/^{208}Pb	± 2SE	^{207}Pb/^{235}U Age	± 2SE	^{206}Pb/^{238}U Age	± 2SE	^{208}Pb/^{232}Th Age	± 2SE	^{207}Pb/^{206}Pb Age	± 2SE	^{206}Pb/^{204}Pb	^{207}Pb/^{204}Pb	^{208}Pb/^{204}Pb
17OR03-001	46.7	6.2	0.789	0.085	0.415	0.057	0.621	0.064	0.458	0.023	3920	130	3740	310	9740	790	3950	200	15.7	26.1	45.8
17OR03-002	63.6	10	1.04	0.11	0.427	0.036	0.73	0.12	0.463	0.063	4230	170	4580	350	11000	1400	4004	120	22	36	63
17OR03-003	22.7	2.8	0.372	0.04	0.428	0.036	0.26	0.021	0.493	0.017	3200	130	2030	190	4660	340	4001	130	29.8	47	73
17OR03-004	31.5	4.1	0.508	0.061	0.443	0.041	0.383	0.047	0.456	0.027	3510	130	2630	260	6510	700	4050	130	25.7	43	66
17OR03-005	27.3	4.4	0.444	0.051	0.427	0.041	0.324	0.033	0.48	0.039	3380	150	2360	230	5670	510	4000	150	30	40	70
17OR03-006	24.1	3.5	0.434	0.047	0.387	0.042	0.325	0.022	0.489	0.033	3260	140	2320	210	5680	340	3850	160	27.4	29.8	58.5
17OR03-007	31	5.7	0.555	0.085	0.392	0.05	0.368	0.066	0.496	0.043	3490	180	2820	350	6280	960	3850	190	58	50	109
17OR03-008	28	3	0.464	0.037	0.427	0.036	0.373	0.023	0.466	0.022	3406	110	2450	160	6400	330	3994	120	44.4	44	92
17OR03-009	23.9	2.2	0.413	0.018	0.409	0.031	0.307	0.017	0.487	0.024	3259	86	2228	84	5410	260	3932	110	48.3	47.7	92
17OR03-010	28.9	3.7	0.527	0.052	0.389	0.028	0.37	0.036	0.491	0.021	3450	150	2710	220	6330	540	3859	110	43.1	42.8	90
17OR03-011	24.2	2.7	0.425	0.039	0.405	0.033	0.319	0.03	0.481	0.021	3263	110	2270	180	5580	460	3916	120	36.6	39.6	80
17OR03-012	32.6	4.5	0.519	0.058	0.443	0.04	0.415	0.042	0.451	0.021	3540	140	2680	240	6980	610	4047	130	50	61	118
17OR03-016	18	2.2	0.298	0.018	0.423	0.043	0.244	0.017	0.488	0.021	2980	120	1678	88	4410	270	3980	150	48	60	109
17OR03-017	16.3	1.7	0.289	0.021	0.396	0.03	0.221	0.017	0.489	0.023	2880	110	1630	110	4030	280	3886	120	55	66	146
17OR03-019	20.7	2.8	0.352	0.04	0.416	0.034	0.274	0.034	0.471	0.026	3090	130	1930	190	4860	530	3954	120	69	61	126
17OR03-020	95	27	1.62	0.37	0.405	0.035	1.24	0.42	0.513	0.044	4570	300	6300	1100	16300	3600	3912	130	79.8	57.6	118
17OR03-021	19.1	2.1	0.331	0.025	0.406	0.031	0.264	0.024	0.496	0.022	3033	110	1840	120	4710	380	3924	120	81	52.7	119
17OR03-022	14.6	1.6	0.252	0.018	0.415	0.033	0.196	0.012	0.483	0.025	2771	100	1442	91	3610	200	3947	120	107	63	199
17OR03-023	10.35	1.1	0.1814	0.01	0.405	0.03	0.1406	0.0067	0.488	0.017	2438	94	1083	60	2660	120	3915	120	150	88	200
17OR03-024	13.79	1.2	0.234	0.011	0.42	0.03	0.1857	0.0071	0.487	0.021	2727	81	1352	58	3440	120	3985	120	192	94	238
17OR03-025	14.8	1.3	0.259	0.015	0.407	0.031	0.204	0.011	0.487	0.02	2804	92	1481	75	3740	180	3935	120	179	77	207
17OR03-026	13.62	1.3	0.241	0.013	0.413	0.029	0.1922	0.01	0.487	0.014	2706	93	1387	67	3550	170	3945	110	207	79	224
17OR03-027	14.8	1.8	0.256	0.022	0.425	0.036	0.218	0.017	0.462	0.02	2771	110	1460	110	3980	280	3974	130	302	109	322
17OR03-028	10.02	0.87	0.1693	0.0079	0.432	0.035	0.1371	0.0047	0.465	0.018	2428	81	1007	44	2596	83	4001	120	390	112	380
17OR03-029	8.86	0.75	0.1684	0.0082	0.392	0.031	0.1311	0.0038	0.489	0.019	2319	78	1002	45	2490	68	3859	120	390	109	340
17OR03-030	12.6	1.3	0.213	0.016	0.432	0.032	0.169	0.013	0.459	0.019	2632	91	1241	84	3150	220	4010	110	344	109	380
17OR03-031	10.45	0.92	0.1872	0.0079	0.408	0.032	0.1394	0.0042	0.49	0.018	2464	83	1105	43	2637	75	3929	110	2140	163	380
17OR03-032	14.15	1.3	0.245	0.013	0.419	0.03	0.197	0.009	0.468	0.015	2742	90	1409	69	3630	150	3962	110	-350	161	418
17OR03-033	17.09	1.5	0.302	0.014	0.412	0.029	0.235	0.011	0.482	0.015	2927	84	1697	71	4260	170	3941	100	-208	186	530
17OR03-034	8.83	0.79	0.1506	0.0053	0.421	0.032	0.1169	0.0036	0.483	0.018	2310	82	904	30	2234	64	3968	120	-50	10	70
17OR03-035	8.06	0.66	0.1428	0.0054	0.413	0.03	0.1141	0.0036	0.475	0.016	2232	73	859	30	2183	65	3939	110	-111	245	1300
17OR03-036	18.5	1.8	0.325	0.021	0.414	0.032	0.255	0.017	0.477	0.028	3024	100	1808	100	4580	270	3947	120	-108	332	4700
17OR03-037	17.8	2	0.291	0.017	0.414	0.032	0.236	0.015	0.484	0.023	2957	99	1680	110	4340	280	3962	130	-81.1	365	-3180
17OR03-038	20.5	2	0.34	0.027	0.426	0.032	0.291	0.015	0.452	0.031	3110	95	1880	130	5160	230	3996	110	-67	500	-1220
17OR03-039	20.5	1.8	0.362	0.034	0.412	0.049	0.289	0.019	0.492	0.047	3111	90	1990	160	5130	290	3940	170	-89	970	-980

Table C.3: Apatite U-Pb data for sample 17OR-03 (Site V).

Sample Information	
Sample Designation	17OR-03, 17OR-09, 17OR-10, 17OR-18
Sample Type	pluton
Laboratory & Sample Preparation	
Laboratory name	Dept of Geology & Geophysics, Texas A&M University
Sample type/mineral	Bedrock apatites
Sample preparation	Conventional mineral separation, 1 inch resin mount, 1μm polish to finish
Imaging	optical scan
Analysis Date(s)	5/2/18
Laser ablation system	
Make, Model & type	ESI/New Wave Research, 193nm excimer, ns
Ablation cell & volume	NWR TV2 cell
Laser wavelength (nm)	193 nm
Pulse width (ns)	4 ns
Fluence ($J.cm^{-2}$)	3.5
Repetition rate (Hz)	15 Hz
Spot size (μm)	60 μm
Sampling mode / pattern	stationary circle
Carrier gas	He 0.6 l/min, Ar make-up gas 0.8 l/min combined 1/4 of way along sample line.
Ablation duration (secs)	30 s
Cell carrier gas flow (l/min)	0.6 l/min
ICP-MS Instrument	
Make, Model & type	ThermoScientific iCAP RQ
Sample introduction	Ablation aerosol directly to injector
RF power (W)	1450W
Make-up gas flow (l/min)	0.8 l/min Ar
Detection system	pulse / analog SEM (analog trigger >2.5M cps)
Masses measured	29Si, 31P, 45Sc, 49Ti, 88Sr, 89Y, 93Nb, 139La, 140Ce, 141Pr, 142Nd, 152Sm, 153Eu, 157Gd, 159Tb, 164Dy, 165Ho, 166Er, 169Tm, 174Yb, 175Lu, 178Hf, 181Ta, 202Hg, 204Pb, 206Pb, 207Pb, 208Pb, 232Th, 235U, 238U, 232Th.16O, 238U.16O
Integration time per peak (ms)	varies, 0.01 to 0.05 sec
Total integration time per reading (secs)	
Sensitivity / Efficiency (%, element)	7.5E3 to 10E3 CPS/ppm (NIST 612)
IC Dead time (ns)	20 ns
Data Processing	
Gas blank	10 second on-peak zero subtracted
Calibration strategy	91500 primary reference material (U-Th-Pb) and NIST 610, 612, 614 (concentrations)
Reference Material info	91500 (Wiedenbeck et al 1995)
Data processing package used / Correction for LIEF	Qtegra (concentrations) and Iolite (U-Th-Pb ages)
Mass discrimination	$^{207}Pb/^{206}Pb$ and $^{206}Pb/^{238}U$ normalised to reference material using Iolite; DRS: U-Pb Geochron 4; Parameters: Exponential down-hole correction, Cutoff Threshold = 10000, 235U calculated from 238U
Common-Pb correction, composition and uncertainty	not corrected; 204Pb not resolvable from zero after Hg correction
Uncertainty level & propagation	Ages are quoted at 2σ absolute, propagation is by quadratic addition. Excess uncertainty propagated.
Other information	Puck was heated in drying oven at 70°C for 24 hours prior to analysis to set the resin.

Table C.4: Metadata for apatite LA-ICP-MS U-Th-Pb analyses of samples 17OR-18 (Site I), 17OR-10 (Site II), 17OR-09 (Site III), and 17OR-03 (Site V). Modified from Horstwood et al. (2016).

APPENDIX D

[eU] AND ESR

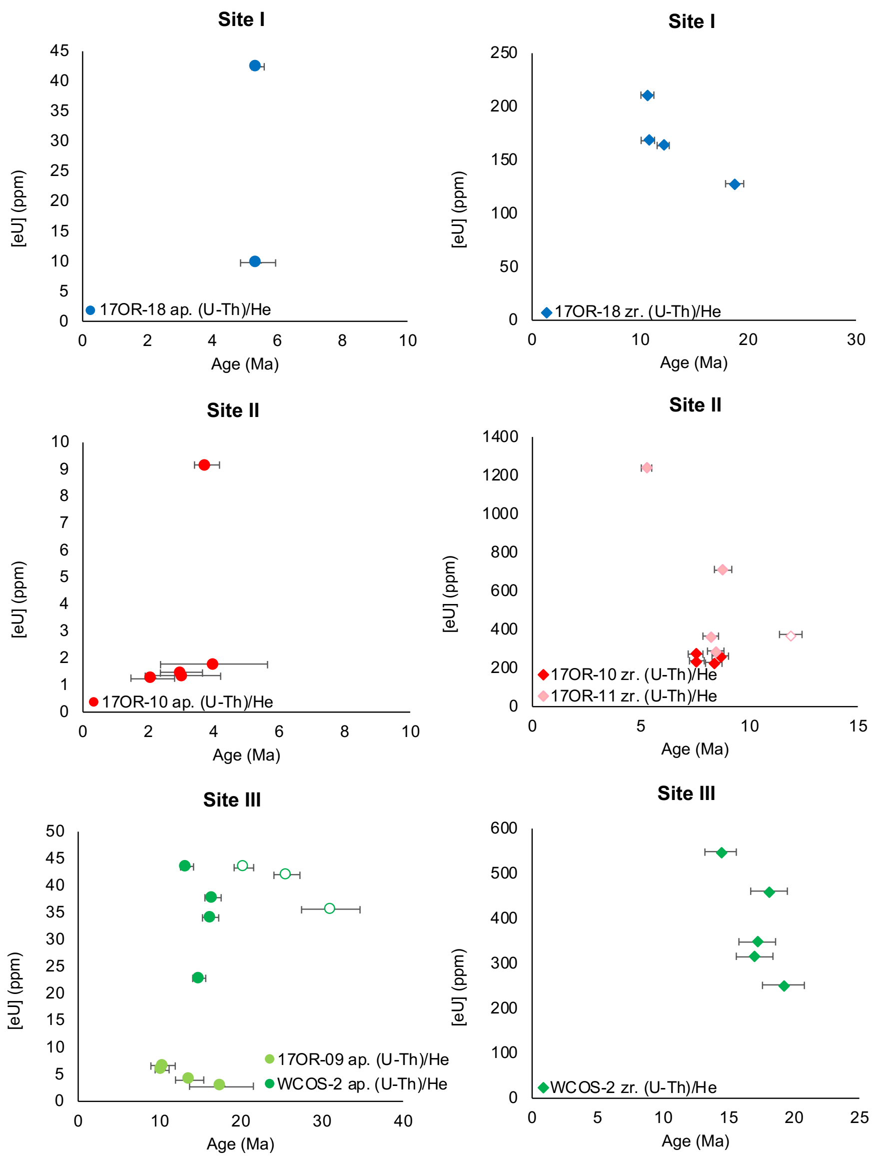

Figure D.1: Effective uranium concentration [eU] values plotted against apatite and/or zircon (U-Th)/He ages at Sites I-III. Hollow markers indicate apatite or zircon (U-Th)/He ages that are older than zircon U-Pb age. Error bars are reported in 2σ.

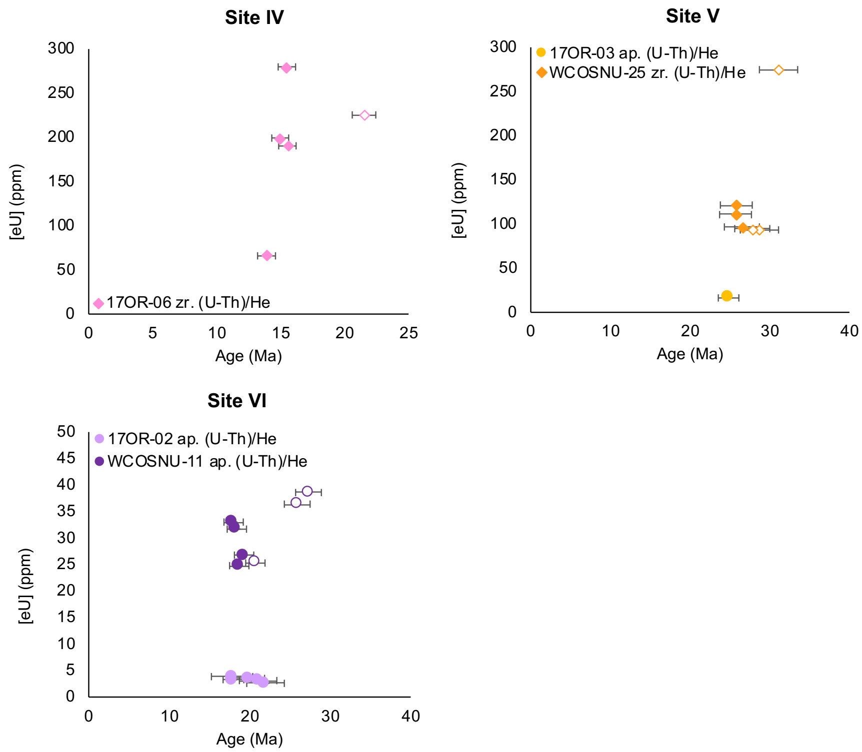

Figure D.2: Effective uranium concentration [eU] values plotted against apatite and/or zircon (U-Th)/He ages at Sites IV-VI. Hollow markers indicate apatite or zircon (U-Th)/He ages that are older than zircon U-Pb age. Error bars are reported in 2σ.

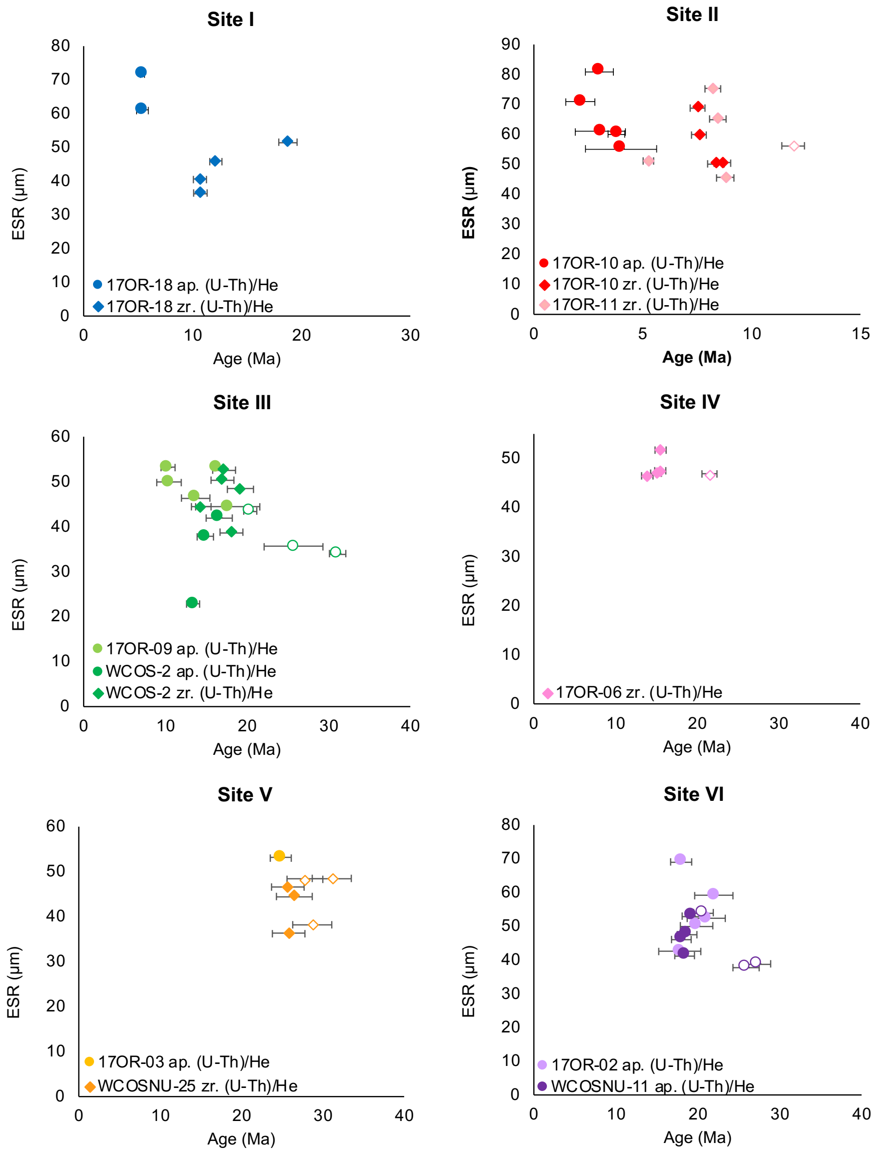

Figure D.3: Equivalent sphere radius (ESR) values plotted against apatite and/or zircon (U-Th)/He ages at each site location. Hollow markers indicate apatite or zircon (U-Th)/He ages that are older than zircon U-Pb age. Error bars are reported in 2σ.

APPENDIX E

BASALT $^{40}Ar/^{39}Ar$ DATA

EXP#18E21686 > 17OR-19 > Groundmass > PESEK (18-23)
WASHINGTON > WESTERN CASCADES
18-OSU-04 (4C2-18) > Incremental Heating > Dan Miggins

Information on Analysis and Constants Used in Calculations

Project = **PESEK (18-23)**
Sample = **17OR-19**
Material = **Groundmass**
Location = **Western Cascades**
Region = **Washington**
Analyst = **Dan Miggins**
Irradiation = **18-OSU-04 (4C2-18)**
Position = **X: 0 | Y: 0 | Z/H: 3.19 mm**
FCT-NM Age = **28.201 ± 0.023 Ma**
FCT-NM Reference = **Kuiper et al (2008)**
FCT-NM 40Ar/39Ar Ratio = **9.87648 ± 0.00919**
FCT-NM J-value = **0.00159140 ± 0.00000148**
Air Shot 40Ar/36Ar = **307.9280 ± 0.2679**
Air Shot MDF = **0.98989694 ± 0.00060647 (LIN)**
Experiment Type = **Incremental Heating**
Extraction Method = **Bulk Laser Heating**
Heating = **55 sec**
Isolation = **6.00 min**
Instrument = **ARGUS-VI-E**
Preferred Age = **Total Fusion**
Age Classification = **Eruption Age**
IGSN = Undefined
Rock Class = Undefined
Lithology = Undefined
Lat-Lon = Undefined - Undefined
Age Equations = **Min et al. (2000)**
Negative Intensities = **Allowed**
Collector Calibrations = **36Ar**
Decay 40K = **5.530 ± 0.048 E-10 1/a**
Decay 39Ar = **2.940 ± 0.016 E-07 1/h**
Decay 37Ar = **8.230 ± 0.012 E-04 1/h**
Decay 36Cl = **2.257 ± 0.015 E-06 1/a**
Decay 40K(EC,β^+) = **0.580 ± 0.009 E-10 1/a**
Decay 40K(β^-) = **4.950 ± 0.043 E-10 1/a**
Atmospheric 40/36(a) = **295.50 ± 0.70**
Atmospheric 38/36(a) = **0.1869**
Production 39/37(ca) = **0.0006425 ± 0.0000059**
Production 38/37(ca) = **0.0001800 ± 0.0000173**
Production 36/37(ca) = **0.0002703 ± 0.0000005**
Production 40/39(k) = **0.000607 ± 0.000059**
Production 38/39(k) = **0.012077 ± 0.000011**
Production 36/38(cl) = **262.80 ± 1.71**
Scaling Ratio K/Ca = **0.430**
Abundance Ratio 40K/K = **1.1700 ± 0.0100 E-04**
Atomic Weight K = **39.0983 ± 0.0001 g**

Results	40(a)/36(a) ± 2σ	40(r)/39(k) ± 2σ	Age ± 2σ (Ma)	MSWD	39Ar(k) (%,n)	K/Ca ± 2σ
Age Plateau Cannot Calculate						
Total Fusion Age		9.69284 ± 0.00334 ± 0.03%	**27.68 ± 0.05** **± 0.19%** Full External Error ± 0.62 Analytical Error ± 0.01		32	0.197 ± 0.000
Normal Isochron Cannot Calculate						
Inverse Isochron Cannot Calculate						

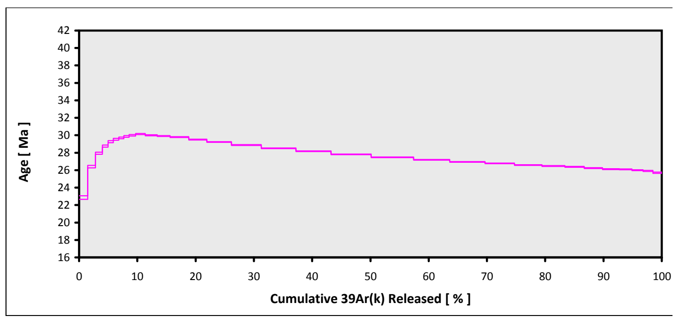

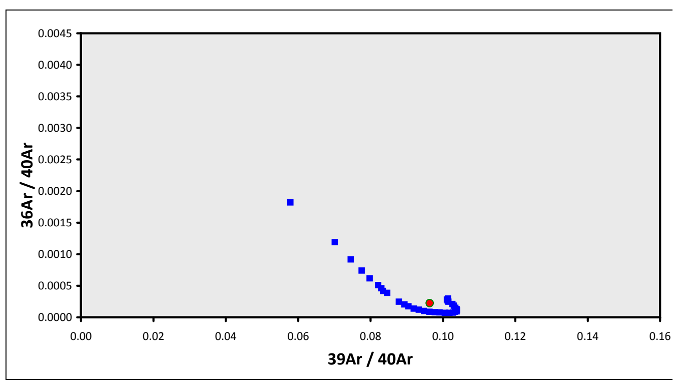

Figure E.1: Basalt $^{40}Ar/^{39}Ar$ results for sample 17OR-19 (Site I).

EXP#18E21861 > 17OR-07 > Groundmass > PESEK (18-23)
OREGON > WESTERN CASCADES
18-OSU-04 (4C3-18) > Incremental Heating > Dan Miggins

Information on Analysis and Constants Used in Calculations

Project = **PESEK (18-23)**
Sample = **17OR-07**
Material = **Groundmass**
Location = **Western Cascades**
Region = **Oregon**
Analyst = **Dan Miggins**
Irradiation = **18-OSU-04 (4C3-18)**
Position = **X: 0 | Y: 0 | Z/H: 4.84 mm**
FCT-NM Age = **28.201 ± 0.023 Ma**
FCT-NM Reference = **Kuiper et al (2008)**
FCT-NM 40Ar/39Ar Ratio = **9.87428 ± 0.00918**
FCT-NM J-value = **0.00159175 ± 0.00000148**
Air Shot 40Ar/36Ar = **308.0260 ± 0.2772**
Air Shot MDF = **0.98982051 ± 0.00060880 (LIN)**
Experiment Type = **Incremental Heating**
Extraction Method = **Bulk Laser Heating**
Heating = **55 sec**
Isolation = **6.00 min**
Instrument = **ARGUS-VI-E**
Preferred Age = **Total Fusion**
Age Classification = **Eruption Age**
IGSN = Undefined
Rock Class = Undefined
Lithology = Undefined
Lat-Lon = Undefined - Undefined
Age Equations = **Min et al. (2000)**
Negative Intensities = **Allowed**
Collector Calibrations = **36Ar**
Decay 40K = **5.530 ± 0.048 E-10 1/a**
Decay 39Ar = **2.940 ± 0.016 E-07 1/h**
Decay 37Ar = **8.230 ± 0.012 E-04 1/h**
Decay 36Cl = **2.257 ± 0.015 E-06 1/a**
Decay 40K(EC,β^+) = **0.580 ± 0.009 E-10 1/a**
Decay 40K(β^-) = **4.950 ± 0.043 E-10 1/a**
Atmospheric 40/36(a) = **295.50 ± 0.70**
Atmospheric 38/36(a) = **0.1869**
Production 39/37(ca) = **0.0006425 ± 0.0000059**
Production 38/37(ca) = **0.0001800 ± 0.0000173**
Production 36/37(ca) = **0.0002703 ± 0.0000005**
Production 40/39(k) = **0.000607 ± 0.000059**
Production 38/39(k) = **0.012077 ± 0.000011**
Production 36/38(cl) = **262.80 ± 1.71**
Scaling Ratio K/Ca = **0.430**
Abundance Ratio 40K/K = **1.1700 ± 0.0100 E-04**
Atomic Weight K = **39.0983 ± 0.0001 g**

Results	40(a)/36(a) ± 2σ	40(r)/39(k) ± 2σ	Age ± 2σ (Ma)	MSWD	39Ar(k) (%,n)	K/Ca ± 2σ
Age Plateau Cannot Calculate						
Total Fusion Age		2.68212 ± 0.00166 ± 0.06%	**7.70 ± 0.02** **± 0.20%** Full External Error ± 0.17 Analytical Error ± 0.00		32	0.180 ± 0.000
Normal Isochron Cannot Calculate						
Inverse Isochron Cannot Calculate						

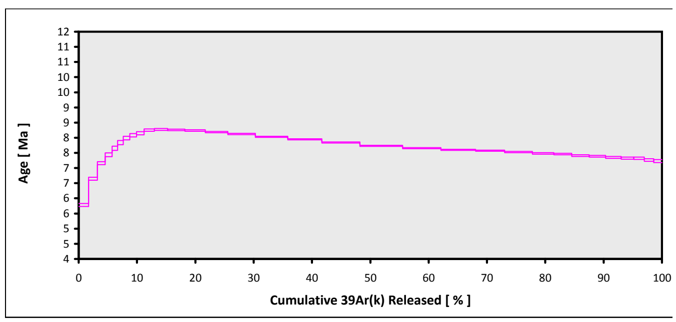

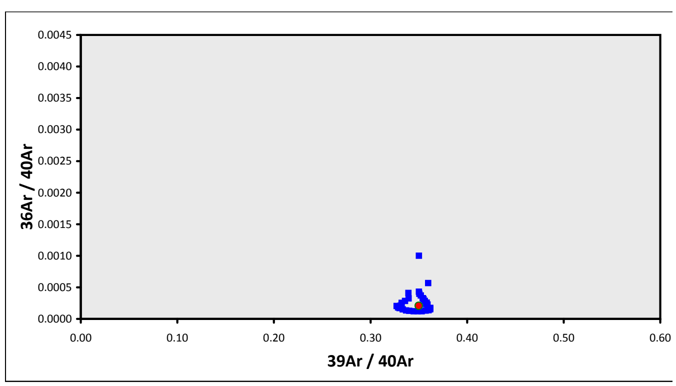

Figure E.2: Basalt $^{40}Ar/^{39}Ar$ results for sample 17OR-07 (Site IV).

EXP#18E21803 > 17OR-05 > Groundmass > PESEK (18-23)
OREGON > WESTERN CASCADES
18-OSU-04 (4C35-18) > Incremental Heating > Dan Miggins

Information on Analysis and Constants Used in Calculations

Project = **PESEK (18-23)**
Sample = **17OR-05**
Material = **Groundmass**
Location = **Western Cascades**
Region = **Oregon**
Analyst = **Dan Miggins**
Irradiation = **18-OSU-04 (4C35-18)**
Position = **X: 0 | Y: 0 | Z/H: 51.46 mm**
FCT-NM Age = **28.201 ± 0.023 Ma**
FCT-NM Reference = **Kuiper et al (2008)**
FCT-NM 40Ar/39Ar Ratio = **10.33437 ± 0.00920**
FCT-NM J-value = **0.00152089 ± 0.00000135**
Air Shot 40Ar/36Ar = **307.9600 ± 0.2556**
Air Shot MDF = **0.98987198 ± 0.00060316 (LIN)**
Experiment Type = **Incremental Heating**
Extraction Method = **Bulk Laser Heating**
Heating = **55 sec**
Isolation = **6.00 min**
Instrument = **ARGUS-VI-E**
Preferred Age = **Plateau Age**
Age Classification = **Eruption Age**
IGSN = Undefined
Rock Class = Undefined
Lithology = Undefined
Lat-Lon = Undefined - Undefined
Age Equations = **Min et al. (2000)**
Negative Intensities = **Allowed**
Collector Calibrations = **36Ar**
Decay 40K = **5.530 ± 0.048 E-10 1/a**
Decay 39Ar = **2.940 ± 0.016 E-07 1/h**
Decay 37Ar = **8.230 ± 0.012 E-04 1/h**
Decay 36Cl = **2.257 ± 0.015 E-06 1/a**
Decay 40K(EC,β⁺) = **0.580 ± 0.009 E-10 1/a**
Decay 40K(β⁻) = **4.950 ± 0.043 E-10 1/a**
Atmospheric 40/36(a) = **295.50**
Atmospheric 38/36(a) = **0.1869**
Production 39/37(ca) = **0.0006425 ± 0.0000059**
Production 38/37(ca) = **0.0001800 ± 0.0000173**
Production 36/37(ca) = **0.0002703 ± 0.0000005**
Production 40/39(k) = **0.000607 ± 0.000059**
Production 38/39(k) = **0.012077 ± 0.000011**
Production 36/38(cl) = **262.80 ± 1.71**
Scaling Ratio K/Ca = **0.430**
Abundance Ratio 40K/K = **1.1700 ± 0.0100 E-04**
Atomic Weight K = **39.0983 ± 0.0001 g**

Results	40(a)/36(a) ± 2σ	40(r)/39(k) ± 2σ	Age ± 2σ (Ma)	MSWD	39Ar(k) (%,n)	K/Ca ± 2σ
Age Plateau		1.62315 ± 0.00517 ± 0.32%	**4.46 ± 0.02 ± 0.36%**	0.56 64%	29.86 4	0.116 ± 0.005
		Full External Error	± 0.10	2.63	2σ Confidence Limit	
		Analytical Error	± 0.01	1.0000	Error Magnification	
Total Fusion Age		1.64132 ± 0.00408 ± 0.25%	**4.51 ± 0.01 ± 0.31%**		32	0.122 ± 0.000
		Full External Error	± 0.10			
		Analytical Error	± 0.01			
Normal Isochron No Convergence	**532.95 ± 683.44 ########**	1.39970 ± 0.64297 ± 45.94%	**3.85 ± 1.76 ± 45.89%**	0.41 66%	29.86 4	
		Full External Error	± 1.77	3.00	2σ Confidence Limit	
		Analytical Error	± 1.76	1.0000	Error Magnification	
Inverse Isochron Clustered Points	**529.65 ± 792.46 ########**	1.40290 ± 0.56986 ± 40.62%	**3.85 ± 1.56 ± 40.58%**	0.41 66%	29.86 4	
		Full External Error	± 1.57	3.00	2σ Confidence Limit	
		Analytical Error	± 1.56	1.0000	Error Magnification	
				1%	Spreading Factor	

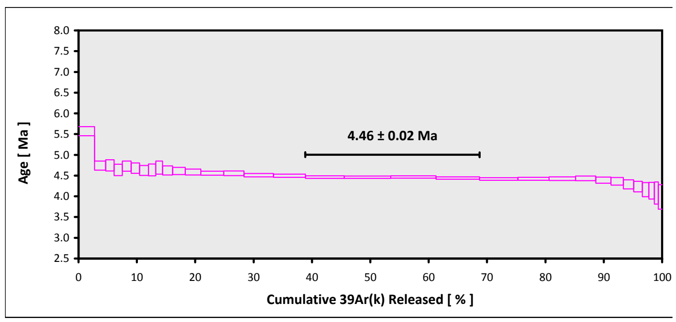

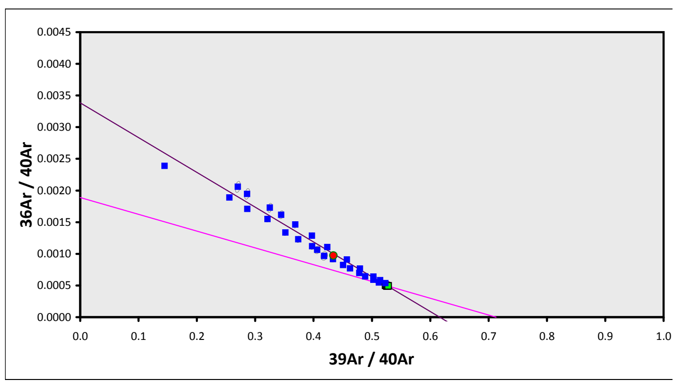

Figure E.3: Basalt $^{40}Ar/^{39}Ar$ results for sample 17OR-05 (Site V).

EXP#18E21745 > 17OR-04 > Groundmass > PESEK (18-23)
OREGON > WESTERN CASCADES
18-OSU-04 (4C5-18) > Incremental Heating > Dan Miggins

Information on Analysis and Constants Used in Calculations

Project = **PESEK (18-23)**
Sample = **17OR-04**
Material = **Groundmass**
Location = **Western Cascades**
Region = **Oregon**
Analyst = **Dan Miggins**
Irradiation = **18-OSU-04 (4C5-18)**
Position = **X: 0 | Y: 0 | Z/H: 7.63 mm**
FCT-NM Age = **28.201 ± 0.023 Ma**
FCT-NM Reference = **Kuiper et al (2008)**
FCT-NM 40Ar/39Ar Ratio = **9.87343 ± 0.00918**
FCT-NM J-value = **0.00159189 ± 0.00000148**
Air Shot 40Ar/36Ar = **307.9930 ± 0.2680**
Air Shot MDF = **0.98984624 ± 0.00060634 (LIN)**
Experiment Type = **Incremental Heating**
Extraction Method = **Bulk Laser Heating**
Heating = **55 sec**
Isolation = **6.00 min**
Instrument = **ARGUS-VI-E**
Preferred Age = **Plateau Age**
Age Classification = **Eruption Age**
IGSN = Undefined
Rock Class = Undefined
Lithology = Undefined
Lat-Lon = Undefined - Undefined
Age Equations = **Min et al. (2000)**
Negative Intensities = **Allowed**
Collector Calibrations = **36Ar**
Decay 40K = **5.530 ± 0.048 E-10 1/a**
Decay 39Ar = **2.940 ± 0.016 E-07 1/h**
Decay 37Ar = **8.230 ± 0.012 E-04 1/h**
Decay 36Cl = **2.257 ± 0.015 E-06 1/a**
Decay 40K(EC,β^+) = **0.580 ± 0.009 E-10 1/a**
Decay 40K(β^-) = **4.950 ± 0.043 E-10 1/a**
Atmospheric 40/36(a) = **295.50 ± 0.70**
Atmospheric 38/36(a) = **0.1869**
Production 39/37(ca) = **0.0006425 ± 0.0000059**
Production 38/37(ca) = **0.0001800 ± 0.0000173**
Production 36/37(ca) = **0.0002703 ± 0.0000005**
Production 40/39(k) = **0.000607 ± 0.000059**
Production 38/39(k) = **0.012077 ± 0.000011**
Production 36/38(cl) = **262.80 ± 1.71**
Scaling Ratio K/Ca = **0.430**
Abundance Ratio 40K/K = **1.1700 ± 0.0100 E-04**
Atomic Weight K = **39.0983 ± 0.0001 g**

Results	40(a)/36(a) ± 2σ	40(r)/39(k) ± 2σ	Age ± 2σ (Ma)	MSWD	39Ar(k) (%,n)	K/Ca ± 2σ
Age Plateau		3.97466 ± 0.02248	**11.41 ± 0.07**	7.07	48.96	0.57 ± 0.12
Error Mean		± 0.57%	**± 0.59%**	0%	18	
			Full External Error ± 0.27	1.69	2σ Confidence Limit	
			Analytical Error ± 0.06	2.6590	Error Magnification	
Total Fusion Age		3.99562 ± 0.00615	**11.47 ± 0.03**		32	1.24 ± 0.00
		± 0.15%	**± 0.24%**			
			Full External Error ± 0.26			
			Analytical Error ± 0.02			
Normal Isochron	**299.61 ± 2.05**	3.92708 ± 0.02718	**11.27 ± 0.08**	3.89	48.96	
Error Chron	**± 0.69%**	± 0.69%	**± 0.71%**	0%	18	
			Full External Error ± 0.27	1.71	2σ Confidence Limit	
			Analytical Error ± 0.08	1.9728	Error Magnification	
Inverse Isochron	**299.63 ± 2.06**	3.92754 ± 0.02718	**11.27 ± 0.08**	3.94	48.96	
Error Chron	**± 0.69%**	± 0.69%	**± 0.71%**	0%	18	
			Full External Error ± 0.27	1.71	2σ Confidence Limit	
			Analytical Error ± 0.08	1.9854	Error Magnification	
				53%	Spreading Factor	

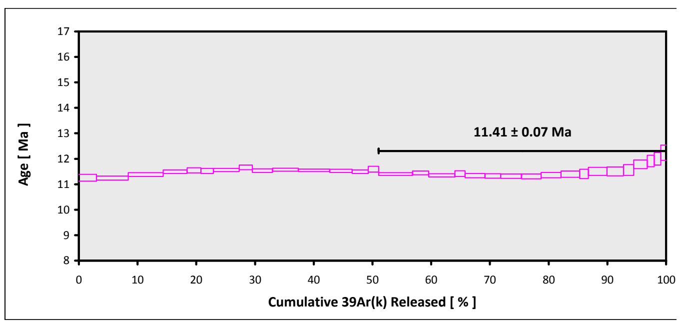

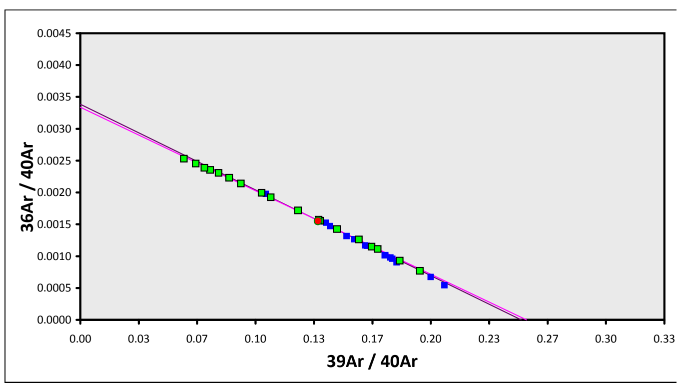

Figure E.4: Basalt ^{40}Ar/^{39}Ar results for sample 17OR-04 (Site V).

EXP#18E21977 > 17OR-20 > Groundmass > PESEK (18-23)
OREGON > WESTERN CASCADES
18-OSU-04 (4C6-18) > Incremental Heating > Dan Miggins

Information on Analysis and Constants Used in Calculations

Project = **PESEK (18-23)**
Sample = **17OR-20**
Material = **Groundmass**
Location = **Western Cascades**
Region = **Oregon**
Analyst = **Dan Miggins**
Irradiation = **18-OSU-04 (4C6-18)**
Position = **X: 0 | Y: 0 | Z/H: 9.57 mm**
FCT-NM Age = **28.201 ± 0.023 Ma**
FCT-NM Reference = **Kuiper et al (2008)**
FCT-NM 40Ar/39Ar Ratio = **9.87497 ± 0.00918**
FCT-NM J-value = **0.00159164 ± 0.00000148**
Air Shot 40Ar/36Ar = **308.0230 ± 0.2834**
Air Shot MDF = **0.98982285 ± 0.00061052 (LIN)**
Experiment Type = **Incremental Heating**
Extraction Method = **Bulk Laser Heating**
Heating = **55 sec**
Isolation = **5.10 min**
Instrument = **ARGUS-VI-E**
Preferred Age = **Total Fusion**
Age Classification = **Eruption Age**
IGSN = Undefined
Rock Class = Undefined
Lithology = Undefined
Lat-Lon = Undefined - Undefined
Age Equations = **Min et al. (2000)**
Negative Intensities = **Allowed**
Collector Calibrations = **36Ar**
Decay 40K = **5.530 ± 0.048 E-10 1/a**
Decay 39Ar = **2.940 ± 0.016 E-07 1/h**
Decay 37Ar = **8.230 ± 0.012 E-04 1/h**
Decay 36Cl = **2.257 ± 0.015 E-06 1/a**
Decay 40K(EC,β^+) = **0.580 ± 0.009 E-10 1/a**
Decay 40K(β^-) = **4.950 ± 0.043 E-10 1/a**
Atmospheric 40/36(a) = **295.50**
Atmospheric 38/36(a) = **0.1869**
Production 39/37(ca) = **0.0006425 ± 0.0000059**
Production 38/37(ca) = **0.0001800 ± 0.0000173**
Production 36/37(ca) = **0.0002703 ± 0.0000005**
Production 40/39(k) = **0.000607 ± 0.000059**
Production 38/39(k) = **0.012077 ± 0.000011**
Production 36/38(cl) = **262.80 ± 1.71**
Scaling Ratio K/Ca = **0.430**
Abundance Ratio 40K/K = **1.1700 ± 0.0100 E-04**
Atomic Weight K = **39.0983 ± 0.0001 g**

Results	40(a)/36(a) ± 2σ	40(r)/39(k) ± 2σ	Age ± 2σ (Ma)	MSWD	39Ar(k) (%,n)	K/Ca ± 2σ
Age Plateau Cannot Calculate						
Total Fusion Age		2.00801 ± 0.00100 ± 0.05%	**5.77 ± 0.01 ± 0.19%** Full External Error ± 0.13 Analytical Error ± 0.00		32	0.302 ± 0.000
Normal Isochron Cannot Calculate						
Inverse Isochron Cannot Calculate						

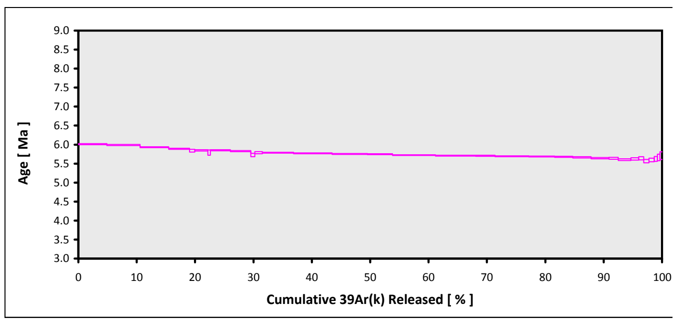

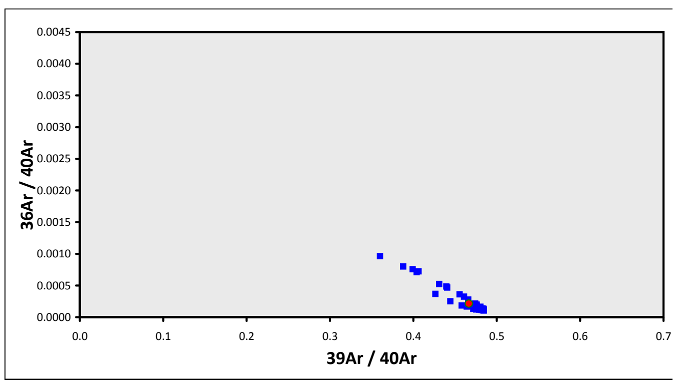

Figure E.5: Basalt ^{40}Ar/^{39}Ar results for sample 17OR-20 (Site VI).

Sample	**Latitude**	**Longitude**	**Elevation (m)**	**$^{40}Ar/^{39}Ar$ Groundmass Age**	**2σ Error (Ma)**	**Type**
17OR-19	46.97	-121.24	1122	27.68	0.05	total fusion age
17OR-12	45.26	-121.88	1490	5.15	0.01	total fusion age
17OR-07	44.13	-122.19	1154	7.7	0.02	total fusion age
17OR-04	43.64	-122.17	1004	11.41	0.07	mini-plateau age
17OR-05	43.72	-122.40	853	4.46	0.02	mini-plateau age
17OR-20	42.67	-122.64	627	5.77	0.01	total fusion age

Table E.1: Basalt sample information and $^{40}Ar/^{39}Ar$ groundmass ages.

APPENDIX F

HeFTy MODELS

Model Name	Site	Pluton Crystallization Range (°C)	Stratigraphic Range (Ma)	Zr. He Samples	Ap. He Samples	Basalt Constraint (Ma)	Number of Paths Run	Acceptable Paths Produced	Good Paths Produced
00193	I	675-950	20-24	-	00193 (Reiners et al., 2002)	2.6	10000	552	299
00193b	I	675-950	20-24	-	00193b (Reiners et al., 2002)	2.6	10000	425	240
00198	I	675-950	20-24	-	00198 (Reiners et al., 2002)	2.6	10000	412	240
97216	I	675-950	20-24	-	97216 (Reiners et al., 2002)	2.6	10000	385	203
97216b	I	675-950	20-24	-	97216b (Reiners et al., 2002)	2.6	10000	349	175
97187	I	675-950	20-24	-	97187 (Reiners et al., 2002)	2.6	10000	388	173
17OR-18a	I	675-950	23.50-24.02	17OR-18 z04	17OR-18 a3	2.6	50000	10	0
					17OR-18 a6				
17OR-18b	I	675-950	23.50-24.02	17OR-18 z03	17OR-18 a3	2.6	50000	75	9
					17OR-18 a6				
17OR-18c	I	675-950	23.50-24.02	17OR-18 z01	17OR-18 a3	2.6	50000	57	11
				17OR-18 z02	17OR-18 a6				
17OR-10a	II	675-950	9.54-9.90	17OR-10 z05	17OR-10 a2	5.15	10000	35	13
				17OR-10 z04	17OR-10 a1				
17OR-10ar	II	675-950	9.54-9.90	17OR-10 z05	17OR-10 a2	reheating at 5.1-5.2	10000	60	21
				17OR-10 z04	17OR-10 a1				
17OR-10b	II	675-950	9.54-9.90	17OR-10 z05	17OR-10 a3	5.15	10000	36	11
				17OR-10 z04	17OR-10 a5				
17OR-10br	II	675-950	9.54-9.90	17OR-10 z05	17OR-10 a3	reheating at 5.1-5.2	10000	38	15
				17OR-10 z04	17OR-10 a5				
17OR-10c	II	675-950	9.54-9.90	17OR-10 z05	17OR-10 a6	5.15	10000	38	11
				17OR-10 z04					
17OR-10cr	II	675-950	9.54-9.90	17OR-10 z05	17OR-10 a6	reheating at 5.1-5.2	10000	21	9
				17OR-10 z04					
17OR-10d	II	675-950	9.54-9.90	17OR-10 z03	17OR-10 a2	5.15	10000	62	32
				17OR-10 z02	17OR-10 a1				
17OR-10dr	II	675-950	9.54-9.90	17OR-10 z03	17OR-10 a2	reheating at 5.1-5.2	10000	104	39
				17OR-10 z02	17OR-10 a1				
17OR-10e	II	675-950	9.54-9.90	17OR-10 z03	17OR-10 a3	5.15	10000	61	17
				17OR-10 z02	17OR-10 a5				
17OR-10er	II	675-950	9.54-9.90	17OR-10 z03	17OR-10 a3	reheating at 5.1-5.2	10000	88	25
				17OR-10 z02	17OR-10 a5				
17OR-10f	II	675-950	9.54-9.90	17OR-10 z03	17OR-10 a6	5.15	10000	70	13
				17OR-10 z02					
17OR-10fr	II	675-950	9.54-9.90	17OR-10 z03	17OR-10 a6	reheating at 5.1-5.2	10000	63	19
				17OR-10 z02					
17OR-11a	II	675-950	9.48-9.64	17OR-11 z03	-	5.15	10000	93	0
				17OR-11 z06					
				17OR-11 z04					
17OR-11b	II	675-800	9.48-9.64	17OR-11 z05	-	reheating at 5.1-5.2	10000	638	314

Table F.1: HeFTy model groupings and results for Sites I-II data.

Model Name	Site	Pluton Crystallization Range (°C)	Stratigraphic Range (Ma)	Zr. He Samples	Ap. He Samples	Basalt Constraint (Ma)	Number of Paths Run	Acceptable Paths Produced	Good Paths Produced
17OR-09a	III	675-800	17.85-19.35	-	17OR-09 a001	6.3	10000	917	189
17OR-09b*	III	675-800	17.85-19.35	-	17OR-09 a004	6.3	10000	1084	562
17OR-09c*	III	675-800	17.85-19.35	-	17OR-09 a002	6.3	10000	831	563
					17OR-09 a6				
WCOS-2a	III	675-800	17.85-19.35	zWCOS-2-5	WCOS-2-4	6.3	10000	71	10
				zWCOS-2-3	WCOS-2-1				
WCOS-2b*	III	675-800	17.85-19.35	zWCOS-2-5	WCOS-2-5	6.3	10000	71	5
				zWCOS-2-3					
WCOS-2c*	III	675-800	17.85-19.35	zWCOS-2-5	WCOS-2-6	6.3	10000	51	4
				zWCOS-2-3					
WCOS-2d	III	675-800	17.85-19.35	zWCOS-2-6	WCOS-2-4	6.3	10000	112	54
				zWCOS2-4	WCOS-2-1				
WCOS-2e*	III	675-800	17.85-19.35	zWCOS-2-6	WCOS-2-5	6.3	10000	160	51
				zWCOS2-4					
WCOS-2f*	III	675-800	17.85-19.35	zWCOS-2-6	WCOS-2-6	6.3	10000	146	59
				zWCOS2-4					
WCOS-2g*	III	675-800	17.85-19.35	zWCOS-2-2	WCOS-2-6	6.3	10000	128	43
WCOS-2sa	III	675-800	16.2-16.6	zWCOS-2-6	WCOS-2-4	6.3	10000	13	0
				zWCOS-2-4	WCOS-2-1				
WCOS-2sb*	III	675-800	16.2-16.6	zWCOS-2-6	WCOS-2-5	6.3	10000	68	0
				zWCOS-2-4					
WCOS-2sc*	III	675-800	16.2-16.6	zWCOS-2-6	WCOS-2-6	6.3	10000	45	1
				zWCOS-2-4					
WCOS-2sd*	III	675-800	16.2-16.6	zWCOS-2-2	WCOS-2-5	6.3	10000	51	0
WCOS-2se*	III	675-800	16.2-16.6	zWCOS-2-2	WCOS-2-6	6.3	10000	185	57
17OR-06a	IV	675-950	19.48-19.79	17OR-06 z05	-	7.70	10000	146	53
				17OR-06 z03					
				17OR-06 z01					
17OR-06b	IV	675-950	19.48-19.79	17OR-06 z06	-	7.70	10000	317	150
WCOSNU-25	V	675-950	22.8-24.24	zWCOSNU-25-6	-	4.46	10000	0	0
				zWCOSNU-25-4					
17OR-03	V	675-950	22.8-24.24	-	17OR-03 a003	4.46	10000	0	0
17OR-02a	VI	675-950	20.62-21.55	-	17OR-02 a002	5.77	10000	37	1
					17OR-02 a005				
					17OR-02 a004				
17OR-02b*	VI	675-950	20.62-21.55	-	17OR-02 a003	5.77	10000	411	195
					17OR-02 a001				
WCOSNU-11a	VI	675-950	20.62-21.55	-	WCOSNU-11-2	5.77	10000	0	0
WCOSNU-11*	VI	675-950	20.62-21.55	-	WCOSNU-11-5	5.77	10000	25	0
					WCOSNU-11-1				
					WCOSNU-11-4				

*Preferred HeFTy model using youngest apatite (U-Th)/He ages.

Table F.2: HeFTy model groupings and results for Sites III-VI data.

APPENDIX G

EXHUMATION RATE CALCULATIONS

A

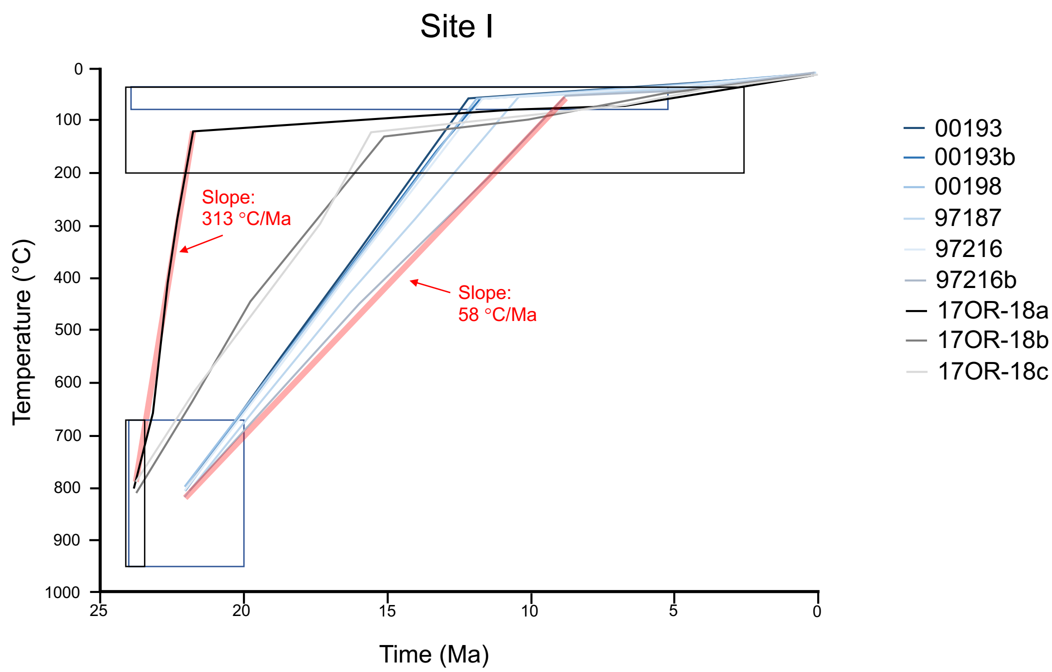

B

<u>20 °C/km Geothermal Gradient</u>

$$\frac{58\ ^{\circ}\text{C / Ma}}{20\ ^{\circ}\text{C / km}} = 3\text{ km / Ma}$$

$$\frac{313\ ^{\circ}\text{C / Ma}}{20\ ^{\circ}\text{C / km}} = 16\text{ km / Ma}$$

<u>40 °C/km Geothermal Gradient</u>

$$\frac{58\ ^{\circ}\text{C / Ma}}{40\ ^{\circ}\text{C / km}} = 2\text{ km / Ma}$$

$$\frac{313\ ^{\circ}\text{C / Ma}}{40\ ^{\circ}\text{C / km}} = 8\text{ km / Ma}$$

Figure G.1: Exhumation rate calculation for Site I. A) All HeFTy model results for Site I, where boxes indicate constraints on the thermochronometer systems. Range of slopes for period of rapid cooling indicated by light red lines and arrows. B) Calculations for exhumation rate ranges using geothermal gradients of 20 °C/km and 40 °C/km.

A

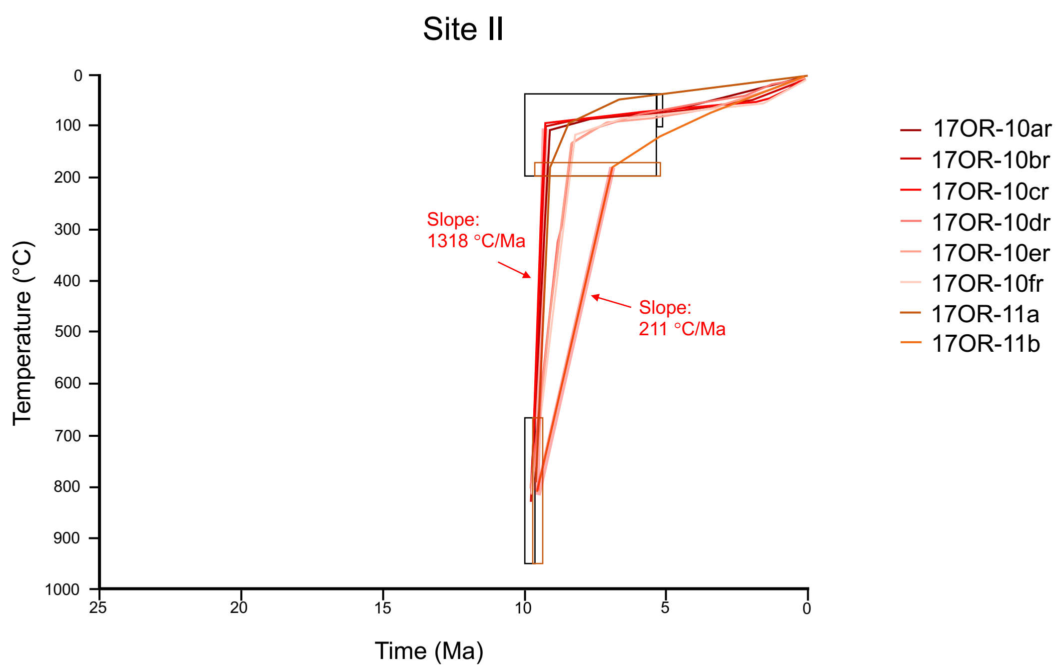

B

<u>20 °C/km Geothermal Gradient</u>

$$\frac{211\ {}^\circ C / Ma}{20\ {}^\circ C / km} = 11\ km / Ma$$

$$\frac{1318\ {}^\circ C / Ma}{20\ {}^\circ C / km} = 66\ km / Ma$$

<u>40 °C/km Geothermal Gradient</u>

$$\frac{211\ {}^\circ C / Ma}{40\ {}^\circ C / km} = 5\ km / Ma$$

$$\frac{1318\ {}^\circ C / Ma}{40\ {}^\circ C / km} = 33\ km / Ma$$

Figure G.2: Exhumation rate calculation for Site II. A) All HeFTy model results for Site II, where boxes indicate constraints on the thermochronometer systems. Range of slopes for period of rapid cooling indicated by light red lines and arrows. B) Calculations for exhumation rate ranges using geothermal gradients of 20 °C/km and 40 °C/km.

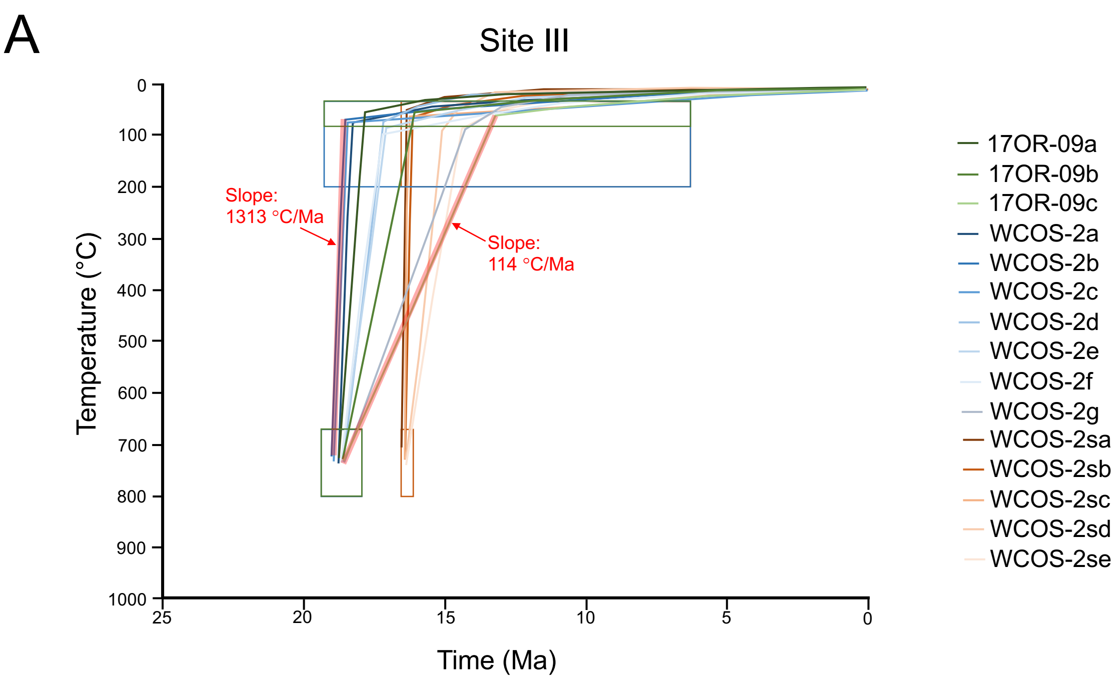

B

<u>20 °C/km Geothermal Gradient</u>

$$\frac{114\ ^\circ\text{C / Ma}}{20\ ^\circ\text{C / km}} = 6\ \text{km / Ma}$$

$$\frac{1313\ ^\circ\text{C / Ma}}{20\ ^\circ\text{C / km}} = 66\ \text{km / Ma}$$

<u>40 °C/km Geothermal Gradient</u>

$$\frac{114\ ^\circ\text{C / Ma}}{40\ ^\circ\text{C / km}} = 3\ \text{km / Ma}$$

$$\frac{1313\ ^\circ\text{C / Ma}}{40\ ^\circ\text{C / km}} = 33\ \text{km / Ma}$$

Figure G.3: Exhumation rate calculation for Site III. A) All HeFTy model results for Site III, where boxes indicate constraints on the thermochronometer systems. Range of slopes for period of rapid cooling indicated by light red lines and arrows. B) Calculations for exhumation rate ranges using geothermal gradients of 20 °C/km and 40 °C/km.

A

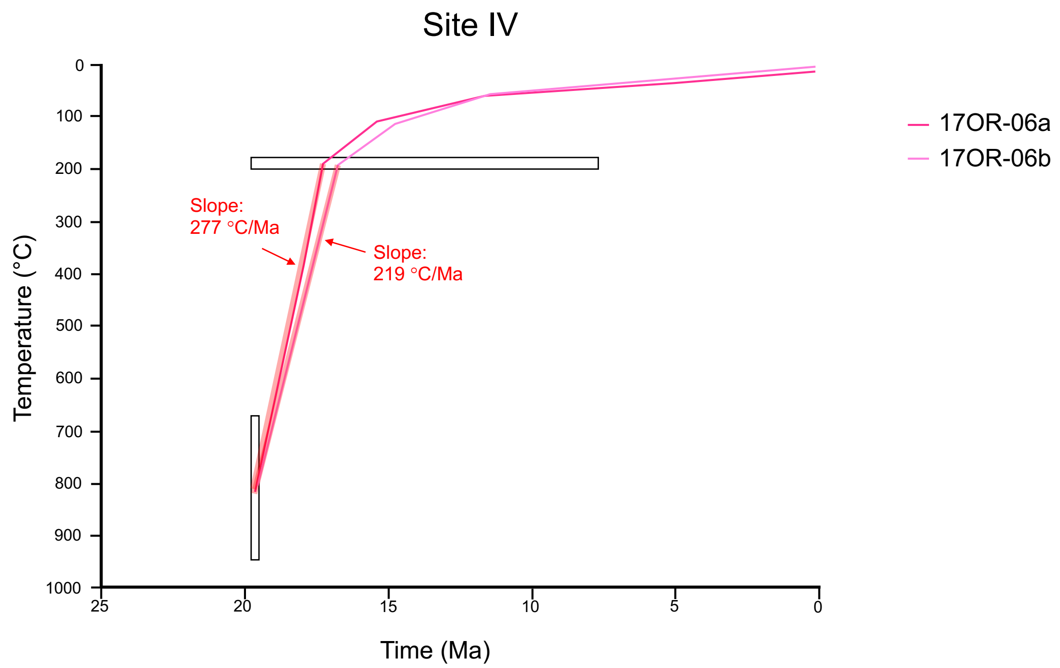

B

<u>20 °C/km Geothermal Gradient</u>

$$\frac{219\ ^\circ\text{C / Ma}}{20\ ^\circ\text{C / km}} = 11 \text{ km / Ma}$$

$$\frac{277\ ^\circ\text{C / Ma}}{20\ ^\circ\text{C / km}} = 14 \text{ km / Ma}$$

<u>40 °C/km Geothermal Gradient</u>

$$\frac{219\ ^\circ\text{C / Ma}}{40\ ^\circ\text{C / km}} = 6 \text{ km / Ma}$$

$$\frac{277\ ^\circ\text{C / Ma}}{40\ ^\circ\text{C / km}} = 7 \text{ km / Ma}$$

Figure G.4: Exhumation rate calculation for Site IV. A) All HeFTy model results for Site IV, where boxes indicate constraints on the thermochronometer systems. Range of slopes for period of rapid cooling indicated by light red lines and arrows. B) Calculations for exhumation rate ranges using geothermal gradients of 20 °C/km and 40 °C/km.

A

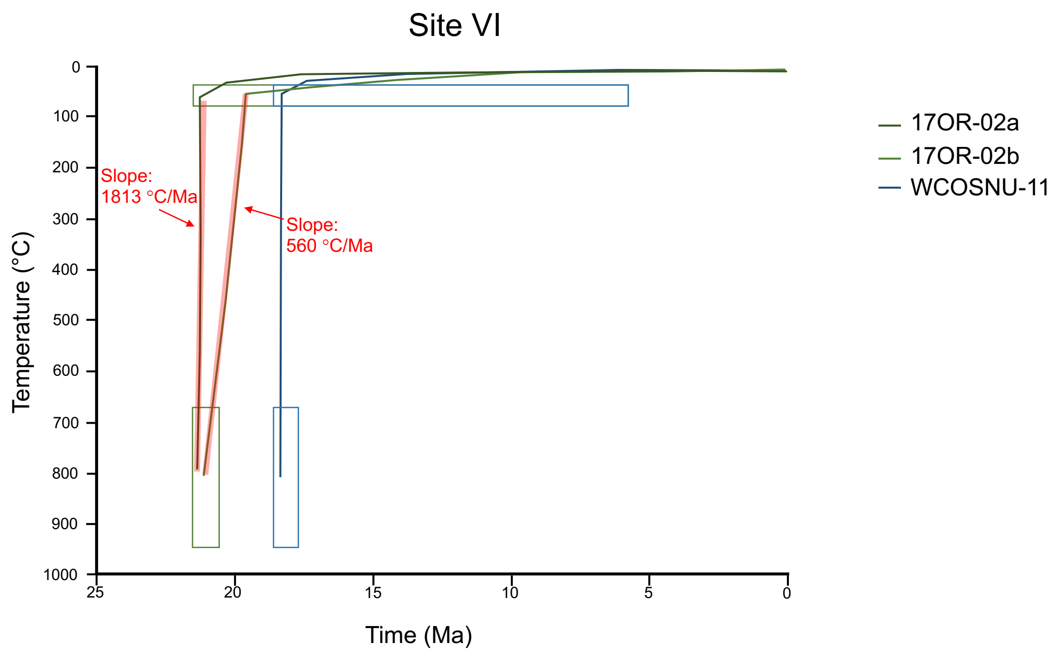

B

20 °C/km Geothermal Gradient

$$\frac{560\ {}^{\circ}\mathrm{C}\ /\ \mathrm{Ma}}{20\ {}^{\circ}\mathrm{C}\ /\ \mathrm{km}} = 28\ \mathrm{km}\ /\ \mathrm{Ma}$$

$$\frac{1813\ {}^{\circ}\mathrm{C}/\ \mathrm{Ma}}{20\ {}^{\circ}\mathrm{C}/\ \mathrm{km}} = 91\ \mathrm{km}\ /\ \mathrm{Ma}$$

40 °C/km Geothermal Gradient

$$\frac{560\ {}^{\circ}\mathrm{C}\ /\ \mathrm{Ma}}{40\ {}^{\circ}\mathrm{C}\ /\ \mathrm{km}} = 14\ \mathrm{km}\ /\ \mathrm{Ma}$$

$$\frac{1813\ {}^{\circ}\mathrm{C}\ /\ \mathrm{Ma}}{40\ {}^{\circ}\mathrm{C}\ /\ \mathrm{km}} = 45\ \mathrm{km}\ /\ \mathrm{Ma}$$

Figure G.5: Exhumation rate calculation for Site VI. A) All HeFTy model results for Site VI, where boxes indicate constraints on the thermochronometer systems. Range of slopes for period of rapid cooling indicated by light red lines and arrows. B) Calculations for exhumation rate ranges using geothermal gradients of 20 °C/km and 40 °C/km.